Czech Technical University in Prague
Faculty of Electrical Engineering
Department of Control Engineering

DOCTORAL THESIS

Distributed manipulation
by controlling force fields
through arrays of actuators

Jiří Zemánek

Prague, 2018

Ph.D. Programme:
    Electrical Engineering and Information Technology
Branch of study:
    Control Engineering and Robotics
Supervisor:
    Zdeněk Hurák

Abstract

This work focuses on the control of distributed manipulation through physical fields created by arrays of actuators. In particular, the thesis addresses manipulation of objects using non-uniform electric and magnetic fields—dielectrophoresis and magnetophoresis, respectively. In both domains, mathematical models suitable for incorporation into a feedback control loop are derived. The models in the two domains exhibit a similar structure, which encourages the development of a unified approach to control. The nonlinear model of the system dynamics is inverted by solving a numerical optimization problem in every sampling period. A powerful attribute of the proposed control strategy is that a parallel manipulation—the simultaneous and independent manipulation of several objects—can be demonstrated. Besides the theoretical concepts, the thesis also describes technical details of experimental platforms for both physical domains, together with outcomes from numerous experiments. For dielectrophoresis, a new layout of electrodes is documented that allows full planar manipulation while requiring only a one-layer fabrication technology. On the algorithmic side, work presents a novel use of phase modulation of the voltages to control dielectrophoresis. Dedicated instrumentation is also discussed in the thesis such as multichannel generators for control of dielectrophoresis through amplitude and phase modulation and optical real-time position measurements using common optics and a lensless sensor. For magnetophoresis, a modular test bed composed of a planar array of coils with iron cores is described in detail. Thanks to the modularity, the platform can be used for verification of not only the centralized but also distributed control strategies.

Keywords

Abstrakt

Tato práce se zaměřuje na řízení distribuované manipulace prostřednictvím fyzikálních polí vytvářených maticí akčních členů. Práce se zabývá především manipulací s objekty pomocí nehomogenního elektrického a magnetického pole - dielektroforézou a magnetoforézou. Pro oba principy jsou odvozeny matematické modely vhodné pro začlenění do zpětnovazební řídicí smyčky. Modely mají v obou doménách podobnou strukturu, která dovoluje vývoj jednotného řídicího systému. Nelineární model dynamiky systému je v každé vzorkovací periodě invertován pomocí numerického řešení optimalizačního problému. Výhodou navržené strategie řízení je, že dovoluje paralelní manipulaci - nezávislou manipulaci s několika objekty najednou. Práce vedle teoretických konceptů popisuje také technické detaily experimentálních platforem spolu s výsledky mnoha experimentů. Pro dielektroforézu je navrženo nové uspořádání elektrod, které umožňuje manipulaci s více objekty v rovině a zároveň vyžaduje pouze jednovrstvou výrobní technologii. Na algoritmické straně práce představuje nové použití fázové modulace napětí pro řízení dielektroforézy. Dále také popisuje součásti vyvinuté instrumentace, jako jsou vícekanálové generátory pro řízení dielektroforézy prostřednictvím amplitudové a fázové modulace a optické měření polohy v reálném čase pomocí senzoru bez objektivu. Pro magnetoforézu je detailně popsána modulární experimentální platforma sestávající se z pole cívek se železnými jádry. Díky modularitě může být platforma použita k ověření nejen centralizovaných, ale také distribuovaných řídicích systémů.

Klíčová slova

Distribuovaná manipulace, řídicí systém, zpětná vazba, dielektroforéza, magnetoforéza, mikromanipulace, elektrické pole, magnetické pole.

Preface

Motivation and contribution

In this work, we focus on control design and implementation for distributed manipulation of one or several objects. By *distributed manipulation*, we mean that the forces exerted on the individual manipulated objects are created through a (planar) *array* or actuators.

In contrast to some works i selves to the physical principles of actuation thanks to which there is no mechanical contact between the manipulated object and the actuator. We consider arrays of (micro)electrodes and coils through which we create and shape the electric and magnetic fields, respectively, from which the corresponding force fields are derived. Namely, in the electric field, we exploit the phenomenon of *dielectrophoresis* (DEP) thanks to which we can manipulate even electrically uncharged particles at micro- and meso-scales, including biological cells, droplets, and micro-LED chips. In the magnetic case, we rely on the phenomenon of *magnetophoresis* that allows us to manipulate objects made of magnetizable materials. The idea of manipulation of one or several objects by shaping the (spatially continuous) force field through a (spatially discrete) array of actuators is valid for other physical domains like acoustics or (micro)fluidics. Our restriction to electric and magnetic fields was driven by the fact that the mathematical formulations in the two physical domains exhibit nearly identical structures; the force is proportional to the gradient of the magnitude of the corresponding physical field ($\mathbf{E}$ or $\mathbf{B}$). This observation enabled us to derive a unified framework for the two actuation principles.

Even if there are several objects to be manipulated at once, our control strategy enables *simultaneous and independent* manipulation of the objects—*parallel manipulation*. We can thus bring several objects to their final destination; we can also bring two objects to a close vicinity of each other in order to analyze their interactions while keeping other objects in the field practically intact. There is a challenge linked to this scenario—if two identical objects experience the same force, the theory predicts that they would be impossible to separate. We demonstrate in our dielectrophoretic setup (using identical microbeads) that, surprisingly, this is possible while relying on the influence of intrinsic noise (hence *noise-aided* controllability).

The core functionality of the position feedback control loop is a real-time computation (in every sampling period) of the voltages to be applied to

the electrodes (or currents to flow through the coils) such that the required forces are exerted on given objects at given positions. Such task is solved as an optimization problem. As such, it naturally needs a mathematical model of the underlying physics. Although such models abound in the literature both on dielectrophoresis and magnetophoresis, they are mostly unusable for real-time computations. In this thesis, simplified models suitable for control purposes are derived and their validity demonstrated both through simulations and through experiments. The proposed modeling procedures can be used for any layout of the actuators.

A nice feature of the models for the dielectrophoresis and magnetophoresis is that they share a common structure—each component of the force is expressed as a *quadratic form* of the inputs (voltages on the electrodes and currents through the coils). The real-time numerical optimization ensuring an inversion of the model thus needs to solve a *quadratically constrained optimization* of sorts. In this thesis, we do not develop a tailored algorithm but rather provide a detailed analysis of the structure of the optimization problem that could be in the future utilized in such algorithmic development.

One of our main contributions to the control of dielectrophoresis is the use of phase modulation—an approach which has not been reported in the literature. It is mostly the amplitudes of the voltages applied to the electrodes that are modulated by the controller. The control through *shifting the phase* requires simpler hardware implementation and offers the possibility to control both the traveling wave and conventional dielectrophoresis.

We validated all concepts introduced in this thesis both using numerical simulations and in real laboratory experiments. We also document most experiments not only in this text but also in numerous illustrative publicly available videos. Some of these videos have received attention of the expert audience (IEEE Control Systems Society, IFAC, and The Mathworks).

Because of the emphasis on experimental verification, we acquired practical and unique know-how and have developed some novel instrumentation. For dielectrophoresis, we developed our own (micro)electrode layout that only requires a single-layer microfabrication technology and yet enables full planar manipulation of several object at once. Due to the combination with the control strategy, the manipulation of objects is not limited in the range and accuracy. It is not constrained by the resolution of the electrode array either. We also developed a 64-channel voltage generator for the control of dielectrophoresis through amplitude and phase modulation. Another novel contribution is the optical lensless sensor for dielectrophoresis that can measure the 3D positions of several objects in real time. The sensor advances the whole developed platform one step closer to being portable

and possibly even disposable, which could be an appreciated property if applications in bioanalytical instrumentation are found.

Similarly, for the magnetophoresis, we developed an experimental platform offering a planar array of 4×4 and, eventually, 8×8 coils. Unlike the dielectrophoretic setup, it is implemented in a *modular* format, with each intelligent module composed of 2×2 array of coils with iron cores and its own control and communication electronics. This opens the opportunity to have distributed not only the actuators but also the controller.

Personal reflections

When I started experimenting with dielectrophoresis some ten years ago— still during my master's studies, I had no idea where it would lead me. At first, I struggled to induce any visible dielectrophoretic effect at all and was far from controlling it. Over the years, including those doctoral ones for which I give an account in this thesis, I not only succeeded in making objects move but I also developed a systematic approach to controlling dielectrophoresis, which I present in this text.

Despite the very tangible achievements detailed in this thesis, I am far from thinking that we are fully in control. These past years have taught me that physics of the real world is much more complex than we would like to assume. During our experiments, we wanted to observe dielectrophoresis, but instead we occasionally got electroosmosis, thermally induced flow, electrolysis damaging our costly electrode arrays, etc. There is still quite a lot to learn and understand in this heavily multidisciplinary research area. Nevertheless, I enjoyed both the theoretical and practical aspects of my work. Experiments often bring real struggle and frustration, but when they finally work in agreement with the theoretical predictions, it is really rewarding.

When I started playing with the manipulation based on magnetic field, it was just another interesting system to control. It was related to the original assignment of dielectrophoresis-based manipulation only through the fact that in both cases the actuators come in the form of an array. It was quite fortunate that the essence of the problem would turn out to be described using the same equations as in the case of its dielectrophoretic version. I am relieved to see how nicely the pieces of the puzzle fit together in the end.

Acknowledgment

In this thesis, I present the main results of my own research in the stated areas. Even though I conceived the basic ideas, others significantly helped me to make them real. Because of that, I am using "we" instead of "I" throughout this thesis. Moreover, I am not a fan of owning ideas and attributing ideas to someone. I had the honor to work with many talented undergraduate and master students as a supervisor of their theses. Most of them were not only technically skillful but truly enthusiastic and it was pleasure and often fun to work with them. I am glad many of them are now my colleagues and friends.

Namely, I would like to thank: *Tomáš Michálek* who significantly contributed to the optimization-based control of DEP and always surprised me with some successful experiments. *Martin Gurtner* who has an exceptional combination of theoretical and practical skills. We worked together on real-time position measurement in 3D, and he came up with great ideas such as control based on numerical range, or approximate model of DEP based on Green's function. *Filip Richter*, a hardware guru who helped me a lot with the platform for magnetic manipulation. *Jakub Drs*, an extreme improviser and a hacker in the best sense of the word, who worked on control of DEP using predefined fields and instrumentation for DEP. *Jakub Tomášek*, an enthusiastic adventurer who worked on optically induced DEP and micromanipulation using the magnetic field. *Aram Simonian*, an athlete and musician who explored reinforcement learning for the magnetic platform. *Jan Filip*, a devoted student who investigated maintaining oscillation using the magnetic field. *Viktor Kajml*, *Filip Kirschner*, *Ivan Nikolaev*, *Tomáš Komárek*, *Bronislav Robenek*, and *Lukáš Zich* also worked on particular issues related to one domain or the other.

Besides, I would like to thank my colleagues. Namely, *Prof. Sergej Čelikovský* for ideas on feedback linearization and switching control. *Petr Svoboda* who made the first prototype of Magman platform. *Jaroslav Žoha* for building a generator for phase modulation.

I would like to thank my supervisor and friend *Prof. Zdeněk Hurák*. We had many interesting, inspirational discussions not only about the topic of this thesis. Thanks to his support I could also meet (and present my work to) leading researchers in the field. He allowed me to explore every idea I had, so that my mind could be creative, sometimes perhaps too creative.

Also, I would like to express gratitude to the EU for funding the international research project called *Golem* (Bio-inspired Assembly Process for Micro- and Mesoscopic Parts) lead by *Prof. Yves Bellouard*, through

Structure of the work

The first chapter provides an introduction to the topic of distributed manipulation and a general discussion of control design for such systems. The rest of the thesis is then divided into two main parts. One is devoted to manipulation by shaping of an electric field and the other to manipulation by shaping of a magnetic field; more specifically dielectrophoresis and magnetophoresis, respectively. Both parts have similar inner structures. They start with a survey of the state of the art, followed by a description of the experimental hardware and mathematical models—I have decided to introduce the hardware first because the key concepts subsequently discussed can then be visualized more clearly. The main chapter of each part tackles the design of, and experiments with, the control systems. The concluding discussion for each of the parts is consolidated in a single, final chapter that highlights the principal findings and contributions in both domains.

Contents

II. Manipulation using a magnetic field 75

1

Manipulation by shaping a physical field

1.1. Introduction

The central topic of this dissertation is *distributed manipulation*. Let us first define what this term means and why this topic is important. We will also highlight relevant keywords that appear in the literature.

In distributed manipulation, actuators are not localized on, for example, a robotic arm but are distributed in space. The effect of each actuator is localized and constitutes a discrete or continuous force field. The field exerts a force on one or several objects and the primary goal of the control system is to *shape the field* so that the objects move in the desired way.

Such systems are massively *over-actuated* because they have many more actuators than manipulated objects have *degrees of freedom*. Distributed manipulation is, therefore, robust to malfunction of actuators. Parallel manipulation is suitable for handling, for example, fragile and delicate objects like silicon wafers or sheets of glass. The principle of parallel manipulation can be visualized with the analogy of a crowd of people at a concert passing a person overhead during so-called crowd surfing.

Actuators are often arranged in the form of a regular *array*. Such an array can play the role of an *intelligent conveyor* that is versatile, reconfigurable, and can reroute macro and micro parts. Due to the excess of actuators, distributed manipulation is capable of *parallel manipulation* (or *massively parallel manipulation*), which means *simultaneous* and independent manipulation of a high number objects. Thus, distributed manipulation helps to achieve higher throughput.

Distributed manipulation is well suited for *micromanipulation* and *microrobotics* because methods and tools used for manipulation at macroscale are often not suitable for microscale. This is due to scaling laws of physical
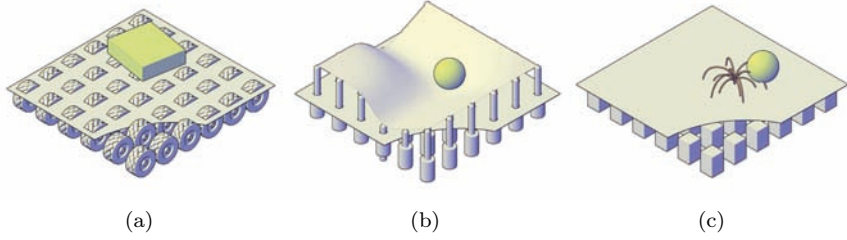
(a)   (b)   (c)

Figure 1.1.: Illustration of distributed manipulation. (a) Array of omnidirec-
tional wheels. (b) Linear actuators deforming a flexible surface.
(c) Magnetic field shaped by the array of coils.

phenomena. Distributed manipulation also allows avoidance of grasping,
which is called *non-prehensile manipulation*. As an example we can think
of vibration feeders[1]. Another possibility is to avoid contact completely, as
when we talk about *noncontact manipulation* and *untethered microrobots*.

The term distributed manipulation may evoke the idea of *distributed
control*. Although those topics are closely related—for large systems it is
reasonable to have distributed control—distributed manipulation can be,
and in fact often is, controlled in a centralized fashion.

We can distinguish between systems that create *discrete* and *continuous*
force fields. The array of wheels illustrated in Fig. 1.1a is a typical example
of a discrete force field where the influence of each actuator is limited to
a single point. On the other hand, some actuators create a continuous
field. For instance, a flexible sheet deformed by a set of linear actuators is
continuous, as depicted in Fig. 1.1b. The set of electrodes or electromagnets
sketched in Fig. 1.1c creates a continuous field as well.

1.2. State of the art

History   One of the first researchers to systematically investigate the use of arrays of
(micro)actuators was K. F. Böhringer. His seminal paper [Bohringer et al.,
1994] describes a novel MEMS (microelectromechanical system)-based array

---

[1]Papers titled Leavin on a plane jet [Reznik et al., 2001] and C'mon part do the local
motion [Reznik and Canny, 2001] show a *Universal Planar Manipulator*, which is a
vibrational plate with three degrees of freedom that can manipulate several objects at
once.

of so-called *motion pixels* and gives the first formulation of the problem of orientating an object using a *programmable force field* (PFF)—a sequence of basic *squeeze force fields* or *radial force fields* [Bohringer et al., 1997]. The inspiration comes from [Erdmann and Mason, 1988] and [Goldberg, 1993], who studied the problem of sensorless orienting of an object using a parallel jaw gripper. [Kavraki, 1997] enhance the PFF concept with some more complex shapes, using force fields derived from elliptic potential fields. [Coutinho and Will, 1998] increase the complexity of the field by segmenting it into polygonal regions and invoking some results from computational geometry. The main achievements in distributed manipulation from the 1990s are summarized in [Böhringer and Choset, 2000]

[Luntz and Moon, 2001] study issues related to the discreteness of the array. The issues become pronounced once the array of actuators is not dense enough to be modeled by a continuous model. [Varsos et al., 2006, Varsos and Luntz, 2006] study a certain class of force fields that derive from quadratic potential fields. The advantage of such force fields is that the requirements on the density of the actuator array are lower and the methodology is especially useful for naturally existing phenomena such as air flows. Discreteness issues are also studied by [Murphey and Burdick, 2004]. They show that a continuous PFF concept can lead to instabilities when translating and rotating an object to a required position and orientation without feedback. Introduction of local feedback is thus justified.

Discreteness

Some authors use the term *intelligent motion surfaces* [Liu and Will, 1995] or *smart surfaces* [Boutoustous et al., 2010] for systems with distributed actuators. [Dang et al., 2016] present a system for moving pallets in a microfactory using a smart surface. Distributed manipulation is also closely related to so-called *robotic materials*—materials that couple sensing, actuation, computation, and communication—reviewed in [McEvoy and Correll, 2015]. Such material can be used as, for example, a morphing airfoil or for active vibrational control of structures. Distributed manipulators also serve in the field of *Human Computer Interface* (HCI) to provide a tangible interface for interaction with a computer; for example, to represent internal states of the computer physically, restore arrangements of the objects from memory, move the objects remotely during a teleconference, etc. This idea is related to the concept of *Tangible Bits*, a physical representation of bits bridging the gap between the physical world and the virtual world [Ishii and Ullmer, 1997], and the concept of *Radical Atoms*, where all digital information has a physical manifestation [Ishii et al., 2012a].

Other names

The concept of distributed manipulation is tested both in the virtual and real world. For example, a virtual smart surface called SmartSurf

Simulation platforms

[Barr et al., 2013] connected with APRON software [Barr and Dudek, 2009] allows prototyping algorithms for 2D arrays. [El Baz et al., 2012] propose distributed discrete state acquisition algorithms and present a smart surface simulator for distributed algorithms. We will focus on real-world platforms.

Physical principles   As to physical principles, the literature describes a number of ways to create a distributed manipulator: for example, arrays of wheels (standard, omnidirectional, or so-called Mecano) [Luntz et al., 1997, Luntz et al., 2001] or swiveling rollers [Kruhn et al., 2013] for manipulation of parcels. Vast numbers of systems use pneumatics [Laurent and Moon, 2015]: for example, sucking and blowing tubes [Safaric et al., 2000, Safaric et al., 2002], and arrays of air nozzles [Mita et al., 1997, Ku et al., 2001, Fromherz and Jackson, 2003, Laurent et al., 2011] created successfully even in microscale [Konishi and Fujita, 1994, Fukuta et al., 2006]. Other works report systems based on arrays of cilia [Liu et al., 1995, Suh et al., 1997, Suh et al., 1999, Bourbon et al., 1999, Ataka et al., 2009], a set of solenoid plungers called a magic carpet [Oyobe et al., 2000], a combination of air jets and electrodes [Pister et al., 1990], an array of vibrational motors [Georgilas et al., 2012], an ultrasonic phased-array for acoustic levitation [Ochiai et al., 2013, Marzo et al., 2018], and motorized potentiometers actuating an array of extensible rods [Follmer et al., 2013, Leithinger et al., 2014].

     Several platforms for manipulation using an array of actuators also appeared on the Internet and there are no relevant research papers to cite. For example, the pneumatic modular conveyor belt called *Festo WaveHandling system*[2], a package handling system called *Celluveyor*[3] consisting of hexagonal modules with omnidirectional wheels, and an array of electromagnets intended for 3D printing[4].

     Also, there are many platforms using an electric or magnetic field. These are surveyed in detail at the beginning of the two main parts of this dissertation, where we address manipulation using magnetic and electric fields.

Micromanipulation and microrobotics

Micromanipulation and *microrobotics*[5] have big potential in fields such as biology, biochemistry, microfabrication, and health care. The applications cover minimally invasive medicine [Nelson et al., 2010] and the assembly of parts [Gauthier and Régnier, 2010]. [Desai et al., 2007, Castillo et al., 2009] review techniques for manipulating biological samples. A tutorial

---

[2]http://www.festo.com/cms/en_corp/13136.htm
[3]http://www.celluveyor.com/
[4]http://www.maglev3d.com/

paper on microrobotics covering applications and challenges is [Abbott et al., 2007]. [Bourgeois and Goldstein, 2015] report on progress and challenges in distributed intelligent MEMS.

Distributed manipulation is suitable for micromanipulation because tools used at macroscale do not necessarily work well at microscale. Our intuition may be misleading[6]. [Wautelet, 2001] examines scaling laws of various physical phenomena showing, for example, the dominance of surface effects such as adhesion and friction over volumetric effects such as gravity and inertia. The dominance of surface effects, for example, makes it difficult to release an object from a gripper.

[Fearing, 1995] survey adhesive forces that create limitations for handling parts smaller than 1 mm. [Menciassi et al., 2004] show models and experiments related to micromanipulation with special attention to grasping and the contact area. [Castellanos et al., 2003] discuss scaling of forces (due to electrothermal flow, DEP, electroosmosis, etc.) exerted on particles in aqueous solutions in a nonuniform electric field.

Some examples of platforms for micromanipulation were already mentioned above in the survey of physical principles used for distributed manipulation. Here, we will only briefly mention techniques for micromanipulation, such as optical tweezers [Moffitt et al., 2008], magnetic tweezers [Vlaminck and Dekker, 2012], surface acoustic waves [Wang and Zhe, 2011], digital microfluidics [Samiei et al., 2016], electrowetting on dielectric (EWOD) [Schaler et al., 2012], Marangoni's flow (or laser-induced thermocapillary convection) [Vela et al., 2009, Ishii et al., 2012b], and control of microflows [Probst et al., 2012]. [Sin et al., 2011] review and discuss several system integration approaches.

---

[5]We should note that concept of a robot is relaxed at microscale—robots do not have to necessarily be equipped with motors, sensors, computers, etc., but similar use of tools and approaches from the field of robotics justifies the term robot. A small magnet, a microsphere, and even an air bubble are called microrobots if some external system controls their position.

[6]As mentioned by [Wautelet, 2001, Abbott et al., 2007], our misconception about the microworld can be illustrated by *The Fantastic Voyage*, a movie by Richard Fleischer, in which scientists and doctors in the submarine Proteus are shrunk and injected into the body of a famous Czech scientist to perform microsurgery. A similar, more recent movie is *Innerspace*. Some of the problems with the shrinking of people are that they would be cold because heat dissipation is proportional to the surface while heat production is proportional to the volume, the adhesive force of feet would prevent walking, and they would not see any light due to the small aperture in their eyes, etc.

1.3. One-dimensional example

Consider a single object to be manipulated in a one-dimensional spatial domain. The response of a single object constrained to a horizontal motion in one dimension is described by Newton's second law

$$m\ddot{x}(t) = \sum_{n=0}^{N-1} F_n\left(x(t)\right) - b\dot{x}(t), \tag{1.1}$$

where F_n is a force contributed by the individual actuator indexed by n, m is the mass of the object, b is the coefficient of viscous friction, and N is the number of actuators. Clearly, F_n is a function of the position $x(t)$ of the object. Assuming that each actuator exhibits identical force, a *unit influence function* $f(x)$ (spatial equivalent to impulse response) can be introduced. For the equidistant spatial sampling h, we can write the motion equation as

$$m\ddot{x}(t) = \sum_{n=0}^{N-1} u_n(t) \cdot f(x(t) - nh) - b\dot{x}(t), \tag{1.2}$$

where u_n are inputs to the system and they represent the scaling the individual local contributions to the global force field. The unit influence function can be for conservative fields derived from a scalar potential (*unit potential function* $\phi(x)$) as negative gradient. In one dimensional case

$$f(x) = -\frac{\partial}{\partial x}\phi(x). \tag{1.3}$$

The example is visualized in Fig. 1.2. The state-space model characterizing dynamics of a single object is

$$\begin{bmatrix} \dot{x}(t) \\ \dot{v}(t) \end{bmatrix} = \underbrace{\begin{bmatrix} 0 & 1 \\ 0 & -\frac{b}{m} \end{bmatrix}}_{\mathbf{A}} \underbrace{\begin{bmatrix} x(t) \\ v(t) \end{bmatrix}}_{\mathbf{x}(t)}$$

$$+ \underbrace{\frac{1}{m}\begin{bmatrix} 0 & 0 & \cdots & 0 \\ f(x) & f(x-h) & \cdots & f(x-(N-1)h) \end{bmatrix}}_{\mathbf{B}(x)} \underbrace{\begin{bmatrix} u_0(t) \\ u_1(t) \\ \vdots \\ u_{N-1}(t) \end{bmatrix}}_{\mathbf{u}(t)}. \tag{1.4}$$
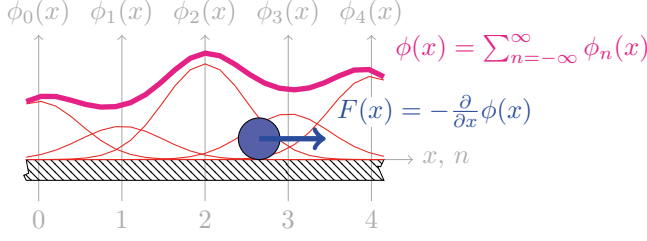
Figure 1.2.: One-dimensional restriction of planar manipulation by shaping a potential field. Actuators are placed in integer positions n and each of them is a source of potential $\phi_n(x)$. The force is derived as a gradient of the sum of the potentials.

The state-space model which is so-called *state-dependent model* characterized by two matrices $\mathbf{A}(\mathbf{x})$ and $\mathbf{B}(\mathbf{x})$

$$\dot{\mathbf{x}}(t) = \mathbf{A}\mathbf{x}(t) + \mathbf{B}(x)\mathbf{u}(t), \tag{1.5}$$

where $\mathbf{x}$ is the full state vector (comprising both the position and the velocity). In our case only the matrix $\mathbf{B}(x)$ depends on the state, namely the position. Of course, this is a nonlinear model.

1.4. Feedback linearization

It is easier to control a linear system. To make our system linear, we can use feedback linearization. That means the control $\mathbf{u}(t)$ in (1.5) is chosen in such a way that the product $\mathbf{B}(x)\mathbf{u}(t)$ is linear. We will introduce a new scalar input $\bar{u}$ and a vector of weights $\mathbf{w}$

$$\mathbf{u}(t, x) = \underbrace{\begin{bmatrix} w_0(x) \\ w_1(x) \\ \vdots \\ w_{N-1}(x) \end{bmatrix}}_{\mathbf{w}(x)} \bar{u}(t). \tag{1.6}$$

This vector of weights "allocate" the scalar input to the individual inputs u_i of the system. To make equations easier to read, we will introduce a new symbol $\mathbf{g}(x)$ for the row of the influence functions from the matrix $\mathbf{B}(x)$

$$\mathbf{g}(x) = \begin{bmatrix} f(x) & f(x-h) & \cdots & f(x-(N-1)h) \end{bmatrix}. \tag{1.7}$$

The linearizing input can be written as

$$\mathbf{u}(t,x) = \mathbf{w}(x)\left(\mathbf{g}(x)\mathbf{w}(x)\right)^{-1}\bar{u}(t) \tag{1.8}$$

and then for an arbitrary vector of weights $\mathbf{w}(x)$ we will have a linear system with respect to the new input $\bar{u}(t)$. Of course, the question arises how to pick suitable weights. A natural option is to scale individual actuators according to their influence. This leads to an effective strategy—the bigger influence the actuator has, the more it is activated.

For N objects, we would like to have an individual new input $\bar{u}_i$ for each object. We can now declare a matrix of weights that allocates individual new inputs to the inputs of the system

$$\mathbf{u}(t,x) = \underbrace{\begin{bmatrix} w_{0,1}(x) & w_{0,2}(x) & \cdots & w_{0,M}(x) \\ w_{1,1}(x) & w_{1,2}(x) & \cdots & w_{1,M}(x) \\ \vdots & \vdots & & \vdots \\ w_{N-1,1}(x) & w_{N-1,2}(x) & \cdots & w_{N-1,M}(x) \end{bmatrix}}_{\mathbf{W}(x)} \underbrace{\begin{bmatrix} \bar{u}_1(t) \\ \bar{u}_2(t) \\ \vdots \\ \bar{u}_M(t) \end{bmatrix}}_{\bar{\mathbf{u}}(t)} \tag{1.9}$$

To make the notation simpler, we will collect non-zero rows from the matrix $\mathbf{B}(x)$ describing the effect of individual actuators on individual objects

$$\mathbf{G}(x) = \begin{bmatrix} f(x_1) & f(x_1-h) & \cdots & f(x_1-(N-1)h) \\ f(x_2) & f(x_2-h) & \cdots & f(x_2-(N-1)h) \\ \vdots & \vdots & & \vdots \\ f(x_M) & f(x_M-h) & \cdots & f(x_M-(N-1)h) \end{bmatrix}. \tag{1.10}$$

Similarly to the case of one object, to make system linear with respect to the new inputs, we will express the input to the system as

$$\mathbf{u}(t,x) = \mathbf{W}(x)\left(\mathbf{G}(x)\mathbf{W}(x)\right)^{-1}\bar{\mathbf{u}}(t). \tag{1.11}$$

Now, if we allocate the new inputs to actuator according to influence of the individual actuators on the objects (it implies $\mathbf{W} = \mathbf{G}^{\mathrm{T}}$), we will get

$$\mathbf{u}(t,x) = \mathbf{G}(x)^{\mathrm{T}}\left(\mathbf{G}(x)\mathbf{G}(x)^{\mathrm{T}}\right)^{-1}\bar{\mathbf{u}}(t). \tag{1.12}$$

In this expression, we immediately recognize the pseudoinverse of the matrix $\mathbf{G}(\text{x})$. It means that $\mathbf{u}(t, x)$ is a least-norm solution for an underdetermined system $\mathbf{Gu} = \mathbf{F}_{\text{des}}$, where $\mathbf{F}_{\text{des}}$ is the vector of desired forces acting on the objects. We can formulate this as an optimization problem

$$
\begin{aligned}
\text{minimize} \quad & \|\mathbf{u}\|, \\
\text{subject to} \quad & \mathbf{Gu} = \mathbf{F}_{\text{des}}.
\end{aligned}
\tag{1.13}
$$

The problem is that real systems have saturated inputs. Therefore we can not use pseudoinverse for feedback linearization but we have to solve this optimization problem

$$
\begin{aligned}
\text{minimize} \quad & \|\mathbf{u}\|, \\
\text{subject to} \quad & \mathbf{Gu} = \mathbf{F}_{\text{des}}, \\
& u_{\min} < u_i < u_{\max}.
\end{aligned}
\tag{1.14}
$$

As we will show in the following parts dedicated to manipulation using a nonuniform magnetic and electric field, the force acting on the object is expressed by a matrix form $\mathbf{u}^{\mathrm{T}}\mathbf{Gu}$. Thus, we have to solve this optimization problem

$$
\begin{aligned}
\text{minimize} \quad & \|\mathbf{u}\|, \\
\text{subject to} \quad & \mathbf{u}^{\mathrm{T}}\mathbf{G}_j\mathbf{u} = F_{\text{des,j}}, \\
& u_{\min} < u_i < u_{\max}.
\end{aligned}
\tag{1.15}
$$

We will show that the matrix $\mathbf{G}_j$ has a special structure for the electric and magnetic field. It is singular with maximal rank six or three.

1.4.1. Numerical simulations

The proposed control scheme is demonstrated using numerical simulations. An array of 11 actuators is considered. Each actuator generates a local Gaussian potential field. The suggested scheme was tested on a feedback system consisting of the state-space model describing two objects in a potential field, feedback linearization and two SISO controllers. An example of manipulation is shown in Fig. 1.3.

The total potential created by the set of actuators is visualized in Fig. 1.4. We can notice how the controller sets the blue object in motion and also how it decelerates it and holds the red object "locked" in a given position at the same time.
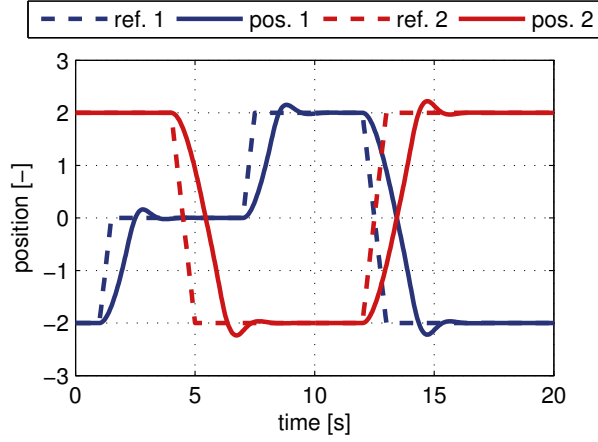
Figure 1.3.: Simulation of parallel manipulation with two objects in the potential field created using 11 actuators. Each actuator acts as a source of local a Gaussian potential.

(a)   (b)
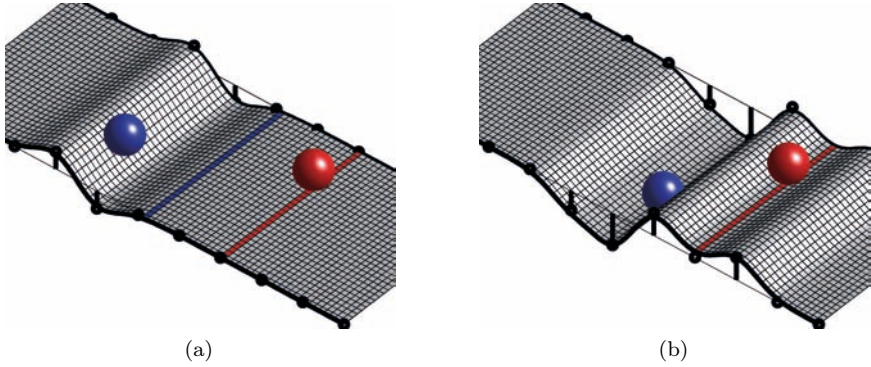
Figure 1.4.: Visualization of the total potential field created using 11 actuators (depicted as black dots along the edges of the stripe). Two objects are represented by spheres and their target positions as correspondingly colored lines. (a) Blue object is approaching its final position, t=1.7 s. (b) Blue object is in the final position. The red object is held still thanks to the decoupling of inputs, t=2.7 s.

Part I.

Manipulation using an electric field

2
Introduction

This part is devoted to distributed micromanipulation using an electric field. We focus mainly on dielectrophoresis (DEP)—the phenomenon that sets even uncharged but polarizable particles in motion within a non-uniform electric field. We will concentrate on control systems for DEP but also address related topics such as layouts of microelectrode arrays, mathematical modeling, and position measurement.

2.1. Dielectrophoresis

The fundamental principle of *dielectrophoresis* (DEP) is that a dielectric particle when placed into an electric field becomes polarized. The resulting *induced dipole*, which approximately describes the effect of the polarization, then interacts with the external electric field. When the electric field is spatially non-uniform, the dipole feels a net force and the particle moves. This is called dielectrophoresis (phoresis comes from the Greek word for migration). The DEP force then attracts or repels the particle to or away from the points of local electric field maximum. These maxima are usually found at the edges of the electrodes. The sign and the magnitude of the DEP force depend on the material properties of the particles and of the media (typically liquid), represented by the so-called *Clausius-Mossotti* (CM) factor. This selectivity makes DEP an attractive tool for various separation tasks, especially in biology.

Moreover, the CM factor depends on the frequency of the driving AC voltage. It is common that for a given material of the particles and the liquid, the particles are attracted toward the electrode edges for some driving frequencies while being repelled at some other frequencies. The former is called *positive DEP* (pDEP), whereas the latter is called *negative DEP* (nDEP). We will use the collective term *conventional DEP* (cDEP) for both pDEP and nDEP. On a planar electrode array, the negative dielectrophoresis

leads to levitation of particles above the electrodes. When at least three phase-delayed AC voltage channels are used, another phenomenon called *traveling wave dielectrophoresis* (twDEP or TWD) can be observed. A gradient of the phase induces a force that can translate the particles along the direction of the gradient, even across the electrode edges.

The external electric field and its inhomogeneities are usually generated and controlled by a set of microscopic electrodes located in the vicinity of the manipulation area. The electrodes can be of various shapes and arrangements, depending on the purpose of the device (separation/fractionation, pumping, focusing, manipulation/positioning, trapping, etc.).

History   Herbert Pohl gave a formal description of DEP in 1951 while he was working at the Naval Research Laboratory [Pohl, 1951], but the phenomenon itself was probably observed earlier[12]. [Pohl, 1958] describes applications of DEP for separation and sketches visually appealing experiments such as hanging drops of liquid in midair, creating fountains, etc. The description of experiments together with photographs appears in [Pohl, 1960] together with a description of a so-called isomotive cell that can separate two powders: for example, industrial diamonds from ceramic dust. Pohl studied polymer particles [Pohl and Schwar, 1959] and living and dead yeast cells [Pohl and Hawk, 1966, Pohl and Crane, 1971], and summarized the theory and experimental setups in [Pohl, 1978]. [Jones and Bliss, 1977] describe DEP of bubbles that can, for example, affect heat transfer during boiling. [Jones and Kallio, 1979] focus on levitation of both solid and hollow spheres and of gas bubbles in a liquid medium. [Jones, 1979] shows various ways of deriving a DEP force. [Batchelder, 1983] uses a traveling electric field to manipulate a water droplet and a small steel ball. Traveling wave DEP was described and exploited in [Masuda et al., 1987, Masuda et al., 1988] and then studied systematically in [Hagedorn et al., 1992]. A case study with yeast cells was presented in [Huang et al., 1993]. Some other relevant works on twDEP are [Morgan et al., 1997, Huang et al., 1997, Hughes et al., 1996].

Reviews and applications   A comprehensive description of DEP can be found in several monographs covering dielectrophoresis such as [Jones, 1995, Morgan and Green, 2002,

---

[2]In [Pohl, 1960], Pohl mentions that their success was due to a fortunate accident. Germans performed similar experiments but with poor results. They used an extremely thin wire, as the theory indicated. The superior results at the Naval Research Laboratory were due to using an ordinary wire; they could not get the thin wire because of wartime shortages.

[2]In [Pethig, 2010], Pethig mentions that the effect was in fact known to the ancient Greeks and Romans. According to Mottelay, Thales of Miletus described it in approximately 600 B.C. in his observation that vigorously rubbed pieces of amber can attract straws, dried leaves, and other light bodies in the same way that a magnet attracts iron.

Hughes, 2003, Ramos, 2011, Pethig, 2017b]. A basic tutorial paper on dielectrophoresis is [Jones, 2003]. DEP has numerous applications, especially in biology and medicine. Because the DEP force depends on the electrical properties, it can be used for separation and characterization of cells. It can transport, focus, trap, and mix particles in microfluidics. The literature on DEP is vast, so we will mention mainly reviews and surveys. Advances in and applications of DEP are reviewed in a series of papers [Pethig, 2010, Pethig, 2013, Pethig, 2017a]. [Hughes, 2016] summarizes 50 years of DEP with a focus on cell separation. [Kua et al., 2005] provides a review of applications of DEP to manipulation of bioparticles. [Zhang et al., 2009, Çetin and Li, 2011, Khoshmanesh et al., 2011] review the applications of DEP forces in microfluidic systems. [Lapizco-Encinas and Rito-Palomares, 2007] survey works using DEP for the separation of nanobioparticles. Applications of DEP to characterization, manipulation, separation, and patterning of cells are reviewed in [Gagnon, 2011]. [Jesús-Pérez and Lapizco-Encinas, 2011] focus on systems for water- and air-monitoring assessment. [Adekanmbi and Srivastava, 2016] survey DEP applications for disease diagnostics. [Lewis et al., 2015] shows the potential of DEP for detection of cancer biomarkers in blood. Small colloidal microbeads actuated by DEP can serve diverse purposes in microfluidic devices like pumps or valves [Terray et al., 2002].

A few companies commercialized DEP systems. For example, the Silicon Biosystems *DEParray* uses DEP field cages to move and recover rare cells[3] and the *ApoStream* platform from ApoCell uses a combination of DEP and field-flow fractionation to separate circulating tumor cells[4].

2.2. State of the art

2.2.1. Micromanipulation using DEP

We can classify systems for manipulation into two groups according to their manipulation area. By manipulation we mean here the steering of particles to desired positions. The first group contains systems that have the *manipulation area limited* to the space between electrodes. Those systems are useful for high-accuracy manipulation within a short range. The second group, on the other hand, covers systems capable of motion across electrodes. Such systems have *virtually unlimited manipulation area* and can serve for long-range transportation.

---

[3]http://www.siliconbiosystems.com/deparray-system
[4]http://www.apocell.com/ctc-technology-2/apostreamtm-technology/

Let us start with the first group. [Edwards and Engheta, 2012] developed so-called *electric tweezers*, which consist of circular electrodes arranged in a circle around the manipulation area. Numerical optimization is then used to find a vector of electrode voltages that leads to the desired DEP force. [Kharboutly et al., 2012a, Kharboutly and Gauthier, 2013] use four triangular electrodes pointing toward the center of the manipulation area. In order to create the required forces on a particle, a simple 2D model is inverted using a Newton-Raphson method for finding the proper voltages. The same group has applied a *model predictive controller* (MPC) together with some transformation of variables that handles even nonlinear dynamics [Kharboutly et al., 2010].

The following systems belong to the second group. [Suehiro and Pethig, 1998] use two glass plates with parallel electrodes arranged in such a way that the electrodes on one plate are perpendicular to the electrodes on the other. It is possible to manipulate a particle by trapping and releasing it at intersections of the electrodes. [Manaresi et al., 2003, Medoro et al., 2007] designed an array of 320×320 microsites, each having dimensions of $20\,\mu m \times 20\,\mu m$ and consisting of an electrode, embedded sensors, and logic. Utilizing the nDEP, they are capable of creating so-called *DEP cages* (stable local equilibria of the force field) between individual electrodes and the conductive coverslip that can be used to trap the particles [Medoro et al., 2003]. If the DEP cage shifts to the neighboring electrode, the trapped particle follows it as well. In addition, every microsite can sense the presence of the particle above itself using an integrated image sensor. [Hunt et al., 2007] followed a similar approach (relying on DEP cages) to construct a 128×256 array of $11\,\mu m \times 11\,\mu m$ pixels that can trap and move cells or liquid droplets in a microfluidic chamber. They also demonstrated splitting of one droplet into two and merging two droplets into one. Both pDEP (without the need of the conductive coverslip) and nDEP can be utilized. [Gascoyne et al., 2004, Current et al., 2007] demonstrated a fluidic processor with 32×32 square electrodes with a side of $100\,\mu m$. [Issadore et al., 2009] even combine the electric field created by an array of 60×61 DEP pixels with the magnetic field created by parallel wires arranged in a grid.

Amplitude modulation is often used to control DEP and has been reported in the literature a number of times [Kharboutly et al., 2012b, Edwards and Engheta, 2012, Zemánek et al., 2015]. To the best of our knowledge, the *modulation of phase*, that is, controlling the phase shifts, was not used for feedback control. Only basic control strategies utilizing predefined force fields are used for twDEP and electrorotation [Cen et al., 2004, Miled and Sawan, 2010, Cen et al., 2003]. Typically a pattern of phases 0, $\pi/2$, π, and

$3\pi/2$ rad is repeatedly applied to subsequent parallel electrodes causing all the particles to move in one direction. Reversing the phase pattern changes the direction of motion. Another use of phase modulation reported in the literature is to create and move DEP cages [Bocchi et al., 2009, Wang et al., 2013, Guo and Zhu, 2015, Manaresi et al., 2003]. [Keilman et al., 2004] show a DEP system consisting of 741 circular electrodes (dubbed lexels) arranged in a checkerboard pattern. The array uses a sample-and-hold circuit and time multiplexing to impose arbitrary voltages on each electrode, although only basic settings and no particle positioning were demonstrated. Our own previous work [Zemanek et al., 2014] demonstrates a strategy for DEP manipulation along nontrivial planar trajectories based on commanding the phase shift of the applied voltages.

2.2.2. Control theory

Early considerations of feedback control in DEP can be found in a series of papers [Kaler and Jones, 1990, Jones and Kraybill, 1986, Jones and Kraybill, 1987]. In these papers, DEP-induced levitation of small particles is used to characterize them; that is, to identify their electric properties. [Chang and Loire, 2003] formulate the dynamics of DEP in the control-oriented framework and use it to find a suitable signal to separate particles hardly separable by a sinusoidal signal. This idea is formalized in [Chang and Petit, 2005]. Another application of classical feedback control is in [Wang et al., 2007] where the authors generate droplets using a feedback control scheme. Similar work is reported in [Hosseini et al., 2008]. Rigorous analysis of a time-optimal control problem for dielectrophoresis is in [Chang et al., 2006]. [Simha et al., 2011a] treat reachability, controllability, and [Simha et al., 2011b] optimal control, but only for a purely theoretical case of control of the levitation height of a particle. [Luo et al., 2018] present a simulation study of dynamic sliding mode control for quadrupole polynomial electrodes. Successful demonstration of feedback manipulation using DEP is still somewhat rare. [Kharboutly et al., 2010, Kharboutly et al., 2012b, Kharboutly and Gauthier, 2013] present open-loop control, model predictive control, and high-speed control for DEP. [Edwards and Engheta, 2012] show electric tweezers that use feedback for micromanipulation.

[Chang and Petit, 2005] enumerate a list of opportunities for control engineers and researchers within the area of DEP. These topics are: control of systems that are quadratic in control, control of systems with bounded control, boundary value control (in the sense of PDEs), system identification, control of interaction among the particles (chaining), and treating multipoles.

2.3. Contribution

Real-time optimization-based controller

Most of the DEP systems documented in published papers work in open-loop mode. That is, no signals are measured and used in real-time to modify the control voltage applied to the electrodes. Although systems for planar DEP manipulation of several particles were described in the literature, they were either limited in the *range of motion* or in *spatial resolution of positioning*. Reported systems that use feedback have limited range of motion because the manipulation area is enclosed by the electrodes. Systems for long-range manipulation, on the other hand, use DEP cages created only at discrete positions above the electrodes. The resolution distance between centers of the electrodes (the resolution of the electrode array) therefore limits the position resolution. We introduce a feedback control approach with an essentially unlimited spatial range and a resolution that is not defined by the electrode geometry. It can work with both amplitude and phase modulation and can control both cDEP and twDEP. Moreover, it allows for parallel manipulation; that is, simultaneous and independent manipulation of several particles at once.

Phase modulation to control DEP

To steer particles along a desired trajectory, systems reported in the literature used amplitude modulation or DEP cages. The only use of phase modulation reported in the literature so far is for creating and moving DEP cages (which means open-loop control). Some systems use predefined phase patterns to change the mode of operation of the electrode array, i.e., a global motion of particles. Our contribution is therefore in utilizing phase modulation for setting the desired force on the particle. Advantages of phase modulation compared to amplitude modulation are that it simplifies hardware implementation and offers a broader set of feasible forces.

Noise aided manipulation

We show how to control multiple particles independently on the parallel electrode array even if they are exposed to the same forces, which happens when they are on the same line parallel to the electrodes. This is an interesting achievement from the control engineering viewpoint because of an expected loss of *controllability* in this situation. Provided that two

identical particles are exposed to same force fields and provided that the inertia effects are negligible (which is the case for small particles), it should be impossible to control them independently. Hence, swapping two particles seems impossible. However, we present a probabilistic control scheme, based on exploiting the intrinsic noise in the system, which recovers controllability.

New layouts of electrodes

We designed innovative layouts of microelectrode arrays as extensions of a standard parallel electrode array. We call these arrays a *corner array*, which consists of two segments of parallel electrodes arranged perpendicular to each other, and a *four-sector array*, which consists of four segments of parallel electrodes. Microelectrode layouts reported in the literature are either limited in their manipulation area because the electrodes are arranged around the area, or are demanding for manufacture because of the need for multilayer fabrication technology or even integration with driving electronics. Matrix electrode arrays are not only demanding for manufacture, but also usually need a conductive coverslip that in turn prevents access. The main advantages of our design are the following. It does not need an upper conductive lid; therefore the manipulation area is still accessible, for example, by a pipette. The layout requires only single-layer fabrication technology; thus it does not need advanced microfabrication facilities. With a simple control, the array can work as a reconfigurable multi-way switch for microfluidics. With precalculated electric fields it can manipulate particles to desired locations, and with optimization-based control, it can steer several particles simultaneously and independently along arbitrary trajectories. The manipulation area is not constrained to a space between electrodes, and manipulation accuracy is not limited by the resolution of the array, as in the case of DEP cages on a matrix array.

Instrumentation

The distinctive character of our work also resides in the experiments because feedback control systems for DEP manipulation are still somewhat rare in the literature. This is one of a few systems that successfully demonstrates feedback DEP manipulation in experiments. To build an experimental setup and conduct experiments requires a lot of time and effort that hardly can be presented as new science. On the other hand, it gave us a lot of experience that may be useful to other teams, such as ways of connecting a microelectrode array, designs of multi-channel generators, and an effective

way of measuring the position of the particles in three dimensions using a simple camera chip.

2.4. Related work

During my dissertation research, I was a supervisor or advisor of many talented students whose work assisted my research. In particular, their bachelor's and master's theses are relevant to manipulation using an electric field. [Drs, 2012] deals with instrumentation for a four-sector array, open-loop phase control, and the NIST Mobile Microbotics Challenge. [Drs, 2015] focuses on trajectory planning for a four-sector array, a platform for manipulation of droplets, and useful fabrication tips. [Tomášek, 2013] investigates optically controlled DEP. [Michálek, 2013] explores phase-based control for a small matrix electrode array. [Michálek, 2015] analyzes optimization-based control for parallel and four-sector arrays, and integration of particle interaction and position uncertainty into the controller. [Gurtner, 2016] proposes a twin-beam method for measuring position, an approximative model of DEP based on Green's function, and application of numerical range for control of DEP. [Machek, 2017] investigates control of electroosmosis.

I also authored or co-authored several research papers that provide a foundation for the text of this part of the thesis. [Zemanek et al., 2014] show the open-loop manipulation strategy on a four-sector array used in the Mobile Microbotics Challenge. [Zemánek et al., 2015] present optimization-based control for DEP on the parallel electrode array. [Gurtner and Zemánek, 2016] propose a cost-effective method for real-time position measurement in 3D using a standard camera chip. [Michálek and Zemánek, 2017] compare dipole and multipole models of DEP to experiments and to the Maxwell stress tensor.

2.5. Organization of the part

The remaining sections of this part are organized as follows. In the next chapter, we will discuss hardware aspects of manipulation using DEP and present our new designs. We will then sum up available mathematical models for DEP and derive a model suitable for feedback control. The penultimate chapter in this part is devoted to our proposed ways to control DEP and our experimental results; namely, we will show how to use predefined fields both in open-loop and in feedback. Then optimization-based control will

be described, together with a discussion of parallel manipulation of several particles. We will present an unusual way to control several particles even though it seems theoretically impossible. Finally, we will show planar manipulation using phase modulation and the four-sector array. We will conclude this part with a chapter summarizing our findings and future research plans.

3

Hardware description

This chapter is devoted to hardware aspects of manipulation using DEP. Namely, we will describe our designs of microelectrode arrays, voltage generators for amplitude and phase modulation, ways of measuring position, and the complete laboratory setup.

3.1. Microelectrode arrays

DEP takes place in a non-uniform electric field that is created by suitably shaped and placed electrodes[1]. The shape and arrangement of the electrodes are essential because they set limitations on the induced motion. Electrode layouts are either planar—this means that the thickness of the electrodes is negligible—or three-dimensional. In addition, layouts are either designed so that the electrodes enclose the working area, or so that particles can pass across electrodes.

Many layouts are described in the literature but we will restrict our attention to those that are suitable for distributed manipulation. A primary example is a *parallel electrode array* that contains parallel bar electrodes, as can be seen in Fig. 3.1. Such a configuration can induce motion of the particles in only one direction — perpendicular to the electrodes[2]. To achieve this motion, it is possible to employ either twDEP or cDEP. Traveling wave DEP requires the presence of a spatial gradient of phase, which can be created applying several voltage signals shifted in phase. To use cDEP for motion across the electrode array, electrodes can be successively activated and either repel or attract the particles through nDEP or cDEP.

---

[1]To be more precise, the non-uniform field can also be generated by a non-uniform environment—for example, by placing pillars between plate electrodes.

[2][Lin and Yeow, 2007] suggest a minor modification of a linear array by letting the width of the electrodes vary continuously (with the length of the electrode). Thus by changing frequency, it is possible to move particles globally in the other direction.
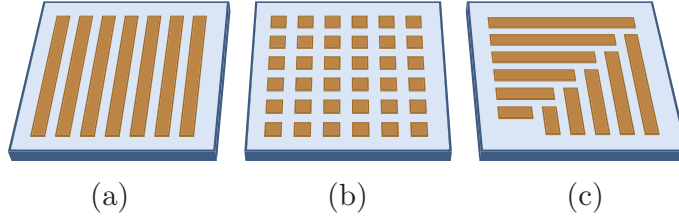
Figure 3.1.: Examples of electrode layouts: (a) parallel electrode array, (b) matrix array, and (c) our design of a corner array.

Systems that can control two-dimensional motion use electrodes arranged to form a *rectangular matrix* (chessboard) as depicted in Fig. 3.1. The drawback of this design lies in its need for advanced fabrication technology. Because of a high number of electrodes, it is difficult to interface them to the external driving circuitry[3]. Matrix electrode arrays, as was mentioned in the literature survey, are realized as integrated circuits that bring electrodes and the driving circuitry together.

3.1.1. Corner array

Our motivation is to achieve planar manipulation even with one layer technology that is more accessible. We come up with an innovative arrangement of the electrodes and call this new design a *corner array*. It consists of two sets of parallel electrodes arranged perpendicular to one another to form a corner, as illustrated in Fig. 3.1.

The original idea was to use this array to move the particles "around the corner," that is, to change the direction of motion for twDEP[4], but it turned out the layout can be used for traveling wave electroosmosis as well. Moreover, it can serve as a basic building block for more complex structures, as we will show later.

The corner electrode array is divided into three zones of interest: two triangular *sectors* containing parallel electrodes arranged perpendicular to

---

[3]Electrode arrays of modest sizes (for instance, 5×5) can be fabricated in such a way that the interconnecting paths lead between electrodes to the edges and are insulated on the top, as shown, for example, in [O'Riordan et al., 2004]. Such arrays are even available as commercial products (originally for electrophysiology). https://www.multichannelsystems.com/
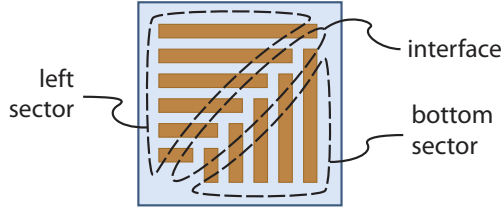
[4][Pethig et al., 1998] show another form of a junction for twDEP.

Figure 3.2.: Main sections of the corner array. The connectors can be attached to the left and bottom sides of the substrate.

(a) clockwise   (b) anticlockwise   (c) up-concentration   (d) down-concentration
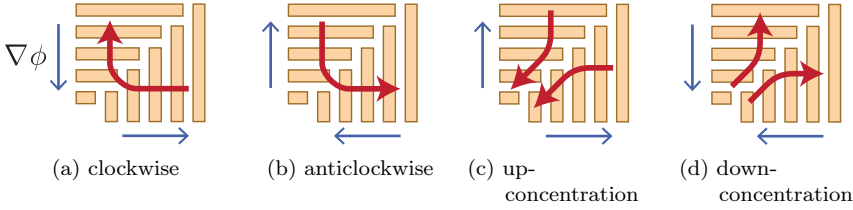
Figure 3.3.: Primary operating modes of the corner array. Arrows along the edges show the direction of the phase gradient. The arrows above the electrodes show the trajectories of induced motion.

one another, and a diagonal *interface* between them. The zones are depicted in Fig. 3.2. Each triangular sector can be used to induce both cDEP and twDEP. As will be demonstrated later, the interesting zone is the diagonal interface between the two sectors.

We will consider twDEP to explain the operation of the corner array. It requires at least three periodic voltages with a mutual phase shift. These voltages are applied to the electrodes to create a traveling wave electric field above the electrodes. The sequence of the phase shifts on the electrodes determines the direction of the traveling wave, and consequently the direction of the induced motion. Four primary operating modes of the corner array are possible: motion around the corner clockwise or anticlockwise, and up-concentration or down-concentration, as depicted in Fig. 3.3.

If the electrode sectors are used in the conventional twDEP regime, the sequence of phase shifts on the electrodes is given and cannot be set arbitrarily. Let us consider four harmonic signals with phases ($0°$, $90°$, $180°$,

and 270°). This quadruple of signals is repeated across the given sector, which induces a standard twDEP, hence a linear translation of particles above the sector, perpendicularly to the electrodes. When the trajectories of the particles reach the diagonal interface, their further motion is influenced by the boundary conditions (voltages) on the neighboring electrodes from the two opposing sectors.

To summarize, in the primary modes, the new corner array allows setting directions of particles above both of the triangular sectors independently, either to steer particles around the corner in both directions or to up-concentrate or down-concentrate particles.

Experiments with the corner array

All the experiments were conducted with 5-µm polystyrene microbeads (Corpuscular Inc.) in deionized water. A harmonic voltage with frequency 200 kHz and amplitude 7 V was applied to the electrodes. We tested the corner array in the four primary operation modes: motion around the corner in both directions, up-concentration, and down-concentration. The results are presented in Fig. 3.4. The shape of observed trajectories of the microbeads is in agreement with the expectations. However, the motion is in the direction of the phase gradient even though, according to the CM factor, it should be in the opposite direction. This discrepancy led us to hypothesize that it may be traveling wave electroosmosis that set the particles in motion.

It is quite difficult to distinguish whether the electric field actuates the medium, which in turn carries the particles, or actuates the particles directly, which in turn sets the medium in motion. Moreover, it can be problematic to figure out the direction of motion. The field moves against the gradient of the phase. From the expression for twDEP, we can deduce that if the Clausius-Mossotti factor is negative ($\mathrm{Im}\,[f_{\mathrm{CM}}(\omega)] < 0$), particles move against the gradient of phase, which means with the field (i.e., co-field motion). But, for example, the review article [Khoshmanesh et al., 2011] erroneously states that "If $\mathrm{Im}\,[f_{\mathrm{CM}}] > 0$ the particle is pushed towards the smaller phase regions and such a motion is termed a co-field TW response." Another problem is that the conductivity of the particle and the medium are essential for twDEP. The conductivity of polystyrene is, according to Wikipedia and MatWeb, approximately $1 \cdot 10^{-16}\,\mathrm{S\,m^{-1}}$, but some articles specify values different by several orders; for example, $2 \cdot 10^{-4}\,\mathrm{S\,m^{-1}}$ in [Rosenthal and Voldman, 2005] or $9 \cdot 10^{-3}\,\mathrm{S\,m^{-1}}$ in [Chang and Loire, 2003].
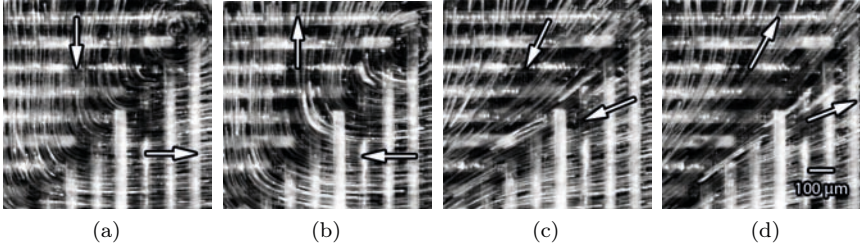
Figure 3.4.: Experimental demonstration of the four primary operation modes. Software-made long exposure of motion of $5\,\mu\mathrm{m}$ polystyrene microbeads in deionized water. (a) Motion around the corner anticlockwise, (b) clockwise, (c) up-concentration, and (d) down-concentration.

3.1.2. Four-sector array

The proposed corner array can be viewed as a basic building block for more complex configurations. For instance, it can serve as a controllable T-junction for microfluidics. An even more powerful layout is a proposed four-sector microelectrode array. It consists of four identical *sectors* (quadrants), each containing parallel electrodes. These sectors are mutually orthogonal and they are arranged as shown in Fig. 3.5a. It provides a cheap and flexible planar manipulation platform. Such a platform could be used, for example, as a four-way mixing valve with a many possible flow paths between inlets and outlets located as in Fig. 3.5b. The array can serve for both DEP and traveling wave electroosmosis.

So far we have considered only a traveling wave above the sectors because it was our first inspiration for this array, but the capabilities of the array are much wider. Using arbitrary voltage on the electrodes, which means various amplitudes or phases, it is possible to generate and move DEP cages along the diagonal interface between sectors and even generate almost arbitrary force above the array, as will be presented in Sections 5.1 and 5.5.

3.1.3. Fabrication

Fabrication of an electrode array starts with the substrate on which it will be created. We used mainly glass and plastic foil. A layer of conductive material is then deposited on top of the substrate by, for example, sputter
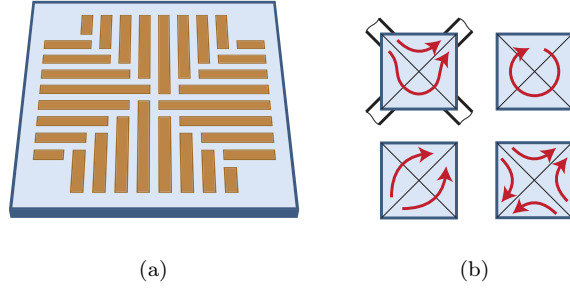
(a)   (b)

Figure 3.5.: (a) Extension of the corner array to a four-sector microelectrode
array. (b) Possible use of the four-sector array as a four-way mix-
ing valve. Depicted interconnection can be rotated or reflected.

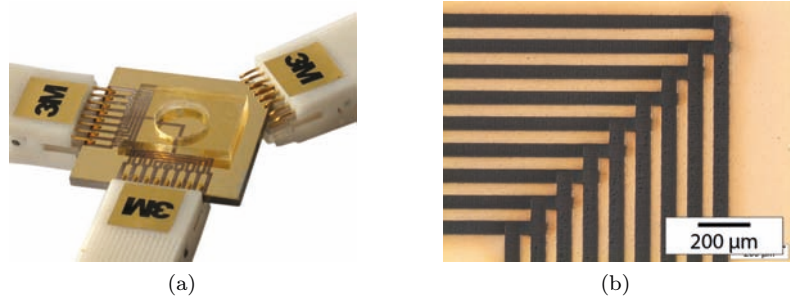(a)   (b)

Figure 3.6.: Detailed view of (a) the corner array with interconnections to
the external circuitry and (b) the fabricated electrodes.

coating. This layer is typically around one hundred nanometers. As the
conductive layer, we used gold with an additional layer for good adhesion,
or ITO (indium tin oxide). Alternatively, it is possible to buy a substrate,
such as a glass slide or a plastic sheet, with an already deposited layer of
some material like, for example, ITO.

The pattern of the electrodes is usually created through some method
for selective removal of the material. We use *laser ablation* or *lithography*.
During laser ablation, a device called an excimer laser progressively removes
unwanted parts of the material using a laser beam. An example showing
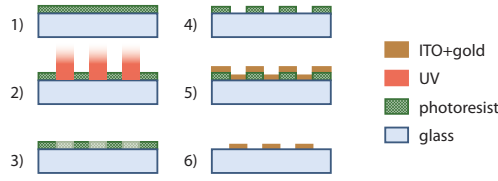the corner array fabricated by the excimer laser is in Fig. 3.6.

Figure 3.7.: Individual steps of lift-off lithography: 1) photoresist spincoat-
ing, 2–3) UV exposure, 4) photoresist development, 5) ITO and
gold sputtering and 6) photoresist removal.[5]

   During lithography, a designed pattern is first projected into a layer
of *photoresist*, which locally changes its properties. Then the photoresist
is developed leaving unwanted parts accessible for *etching*. Alternatively,
the photoresist can be exposed and developed first and material deposited
afterward. This way, the conductive material sticks to the substrate at
places where there is no photoresist, and material that is deposited on the
photoresist is later washed away. This process is called *lift-off lithography*.
The procedure is shown in Fig. 3.7. An alternative way to produce a
microelectrode array is to order it from a company manufacturing PCBs
(printed circuit board). We have found that with PCB technology it is
possible to fabricate electrodes 100 μm wide. An example of such array
is in Fig. 3.8. To beam the desired pattern into the photoresist, we use
either a mask with the required shape or a tabletop laser pattern generator
(Heidelberg μPG 101).
   Once we have manufactured the electrode array, it is necessary to connect
it to external circuitry. We have tried various ways and found that the best
are spring contacts and zero-insert force connectors. Other methods involve
adjusted test clips for integrated circuits (shown in Fig. 3.6) or a flexible
PCB bonded to the array with a special z-axis, electrically conductive,
double-sided tape.

3.2. Experimental setups

The following section describes the two main experimental setups used for
validation of proposed control systems. The first one is set up with a parallel

---

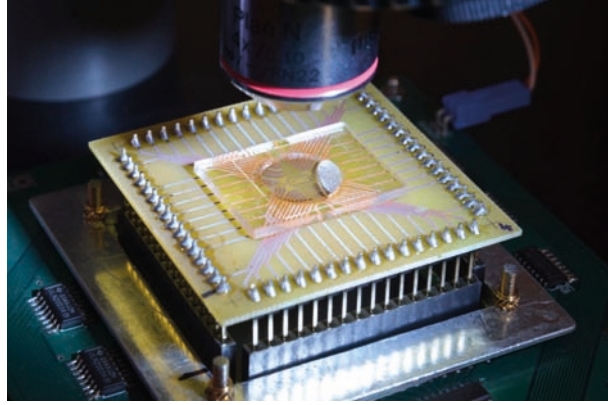[5]Reprinted from [Zemanek et al., 2014].

Figure 3.8.: Electrode array fabricated as a PCB.

electrode array for testing of amplitude modulation, and the second is set up for the four-sector array and phase modulation.

3.2.1. Parallel electrode array and amplitude modulation

This experimental setup contains a parallel electrode array controlled by amplitude modulation. The array consists of an array of eight parallel indium tin oxide (ITO) electrodes, 400 nm in thickness, patterned on a glass substrate. All of them have equal width of 100 µm and are separated by gaps of the same size. There is no insulating layer on the electrodes. A shallow pool is made by cutting a hole with a diameter of 13 mm into a 2 mm thick sheet of *polydimethylsiloxane* (PDMS) and attaching it to the top of the array. Commercially available polystyrene micro-spheres with a diameter of 50 µm (Corpuscular Inc.) are used as the particles to be manipulated. They are immersed in *deionized water* with a conductivity of $50 \, \mu\text{S m}^{-1}$ (as measured using a conductometer, Jenway 4510). See Fig. 3.9a for the manipulator illustration.

By applying sinusoidal voltages of different amplitudes to individual electrodes, a non-uniform electric field is generated above them and a dielectrophoretic force is exerted on the micro-spheres in the pool. We use a standard function generator (Agilent 33220A) to generate a simple

---
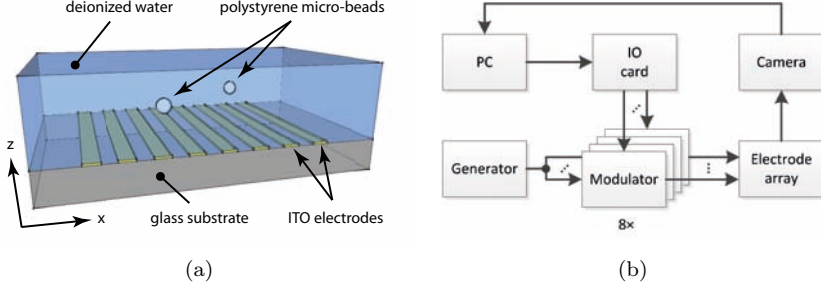[6]Reprinted from [Zemánek et al., 2015].

Figure 3.9.: (a) Main part of the manipulator: parallel electrodes, liquid medium and the manipulated particles. (b) Block diagram of the experimental setup.[6]

sinusoidal voltage. This signal is then brought to eight four-quadrant analog multipliers (AD633) and multiplied by eight voltages set by a PC through an input/output card (MF624, Humusoft). This way we can control the amplitudes of voltages on all eight electrodes in the range of $0\,\mathrm{V}$ to $10\,\mathrm{V}$, and the phase shift can be set to either $0°$ or $180°$. The reason for using the analog multipliers is that it would be challenging to generate sinusoidal signals with frequencies on the order of $100\,\mathrm{kHz}$ with only a computer. As a position measurement for feedback, we use the images acquired through a camera (Pike F-032B, Allied) on a microscope (Olympus BX-FM, $5\times$ magnification lens) providing the top view of the manipulation area. The block diagram of the experimental setup is in Fig. 3.9b.

The real-time control algorithm runs in a Matlab and Simulink environment on a conventional personal computer (Intel i5, $3.30\,\mathrm{GHz}$, $8\,\mathrm{GB}$ RAM, 64-bit, Win 7). The computer is only equipped with a rather standard input/output PCI card (MF624, Humusoft). Through this interface, the voltages for the analog multipliers are set, which then produce voltages applied to the electrodes. The control loop runs with a frequency of $10\,\mathrm{Hz}$; this is determined mainly by the time needed to complete the control algorithm.

3.2.2. Four-sector array and phase modulation

This experimental platform uses the four-sector array controlled by phase modulation. The parameters of a particular realization of the array's design are the following: the widths of the electrodes, as well as the widths of the
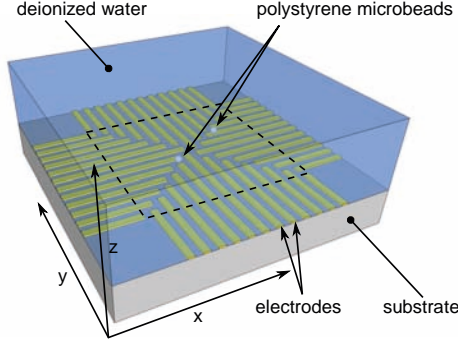
Figure 3.10.: Illustration of the four-sector electrode array manipulator. The dashed lines show the boundary of the manipulation area (1.55 mm × 1.55 mm).

interelectrode gaps, are 50 µm; the electrodes are made of gold on a glass substrate; there is no insulation layer deposited on top of the electrodes.

A circular basin of 13 mm in diameter cut out from a 2.4 mm thick poly-dimethylsiloxane (PDMS) sheet is attached to the surface of the electrode array by pure adhesion. During experiments, the basin is filled with deionized water having a conductivity of $50\,\mu\mathrm{S\,m}^{-1}$ (measured by a conductometer Jenway 4510). Polystyrene microspheres (Corpuscular Inc.) having a diameter of 50 µm are immersed in the water to play the role of test particles. No upper lid covering the experimental area is necessary, but it can be used if, for example, the user wants to reduce the contamination of the water by air pollutants. An illustration of the array is in Fig. 3.10.

The electrode array is placed under a microscope (Olympus BX-FM, 5× magnification lens) that has a digital camera (Pike F-032B, Allied) attached to one of its optical outputs. The camera captures a top view of the electrode array with the microspheres visible as dark circular spots.

A standard PC (Intel i5, 3.30 GHz, 8 GB RAM, 64-bit, Win 7) processes the camera images and runs the control algorithm in real time. The computational demands of those control tasks set the upper bound on the sampling frequency of the feedback controller to 10 Hz. A schematic of the experimental feedback control setup is in Fig. 3.11.
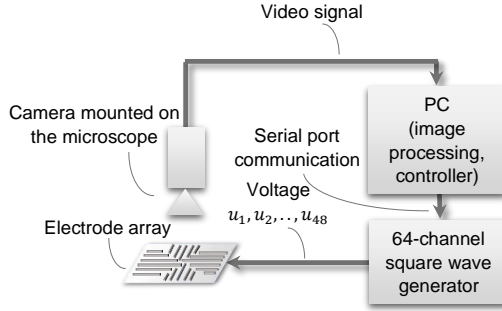
Figure 3.11.: Diagram of the laboratory setup showing the feedback loop.

64-channel generator

The electrodes are connected to the driving circuitry. We designed a programmable voltage generator that can deliver 64 square wave signals with mutual phase shifts because generating voltages of the frequency of a few hundred kilohertz directly from a personal computer (PC) would be very challenging. The phase shift of each channel can be set independently in the 0°–360° range in 16 steps—this gives a step of $\pi/8$ rad. The frequency is derived from the basic frequency 3.125 MHz divided by a value from 1 to 65536, which corresponds to the frequency 47.7 Hz–3.125 MHz. An output stage of each channel is realized using a Darlington transistor and a pull-up resistor designed to switch up to 25 V. In the future, it would be better to use a pair of transistors as a push-pull driver to reduce losses. The amplitudes and the frequencies of the waveforms are the same for all the 64 channels.

A field-programmable gate array (FPGA Xilinx, Spartan-3, XC3S200) serves as the computational heart of the generator. An FPGA chip is suitable for this purpose thanks to the fact that it, unlike a microcontroller, can refresh all its output pins at the same time. Moreover, it is faster. The logic of the generator contains the following function blocks: variable divider of the clock signal, phase shifter, and multiplexers. The signal from the divider is delayed by the phase shifter in such a way that 16 signals ($\varphi_0...\varphi_{15}$) with different phase shift are generated, and each output has its own multiplexer (MUX0...MUX64) passing one of these signals. The FPGA can communicate with an operator PC via RS-232. The block diagram of the generator core is depicted in Fig. 3.12. The generator together with the microelectrode array connected to it can be seen in Fig. 3.13.
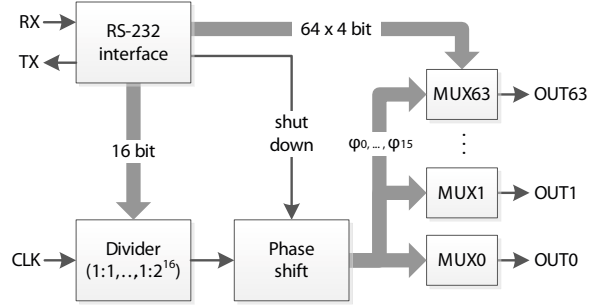
Figure 3.12.: Block diagram of an internal structure of the multichannel generator implemented in FPGA.[7]
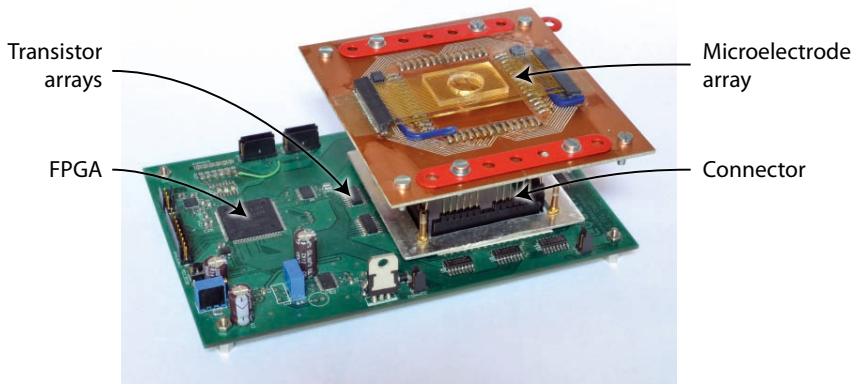
Figure 3.13.: Microelectrode array connected to the generator. Camera with microscope lens is used for visual feedback.[8]

3.3. Position measurement

Information about the current positions of the manipulated particles is essential for feedback control. The position of a particle can be measured using several techniques. A typical way is to use a *camera* on a microscope.

---

[7]Reprinted from [Zemanek et al., 2014].
[8]Reprinted from [Zemanek et al., 2014].

Some electrode arrays reported in the literature integrate *photodetectors* with electrodes. Another reported technique is impedance analysis relying on the change that is caused by the presence of the particle [Brazey et al., 2018]. To eliminate a bulky microscope, it is possible to use so-called *digital microscopy*. This method can reconstruct a 3D image of the scene, but the reconstruction is usually done in post-processing. We present a cost-effective and fast method for measuring the positions of the particles in 3D using a plain camera chip.

3.3.1. Computer vision algorithm

A computer vision algorithm requires the particle to be visually distinguishable from the background. It means that *light* plays an essential role because it changes the visual appearance of the particle. Especially translucent particles might be hard for detection. We achieved the best results with a circular light and a coaxial light going through a lens of the microscope. The former causes a bright spot that appears under the particle (a sphere, in our case). This works best if the background is reflective; otherwise the bright spot is not visible. The latter light makes particles visible as dark spots. Again, the reflective background created better contrast. In practice, if the array is transparent, we can put a piece of aluminum foil under it.

Simple *intensity thresholding* can detect the particles; this means setting a suitable threshold and marking all pixels with intensity above or under it as belonging to the particle. The position of the particle is then calculated as the center of mass of the particle's pixels. To speed up the detection, the thresholding can be done only within the so-called *region of the interest* (ROI). The ROI is a rectangular area capturing only a small part of the whole image. This lowers the number of pixels that need to be processed, but it requires changing the position of the ROI along with the particle.

The position of the ROI needs to be initialized either manually or by having the system process the whole image and find all particles. In every frame, the particle has to be inside the ROI. Here we can suppose that the particle is near the last detected position. Therefore we set the center of the ROI to this position. It requires having the ROI big enough so that the particle cannot escape it between two consecutive frames.

If the particle is partially out of the ROI, the calculated center of mass will not correspond to the center of the particle. We can overcome this by iterative calculation of the center of mass—the center of the ROI is shifted to the center of mass, and the center of mass is calculated again on the same image frame.

The detected position of the particle is determined with respect to the image coordinate frame, but usually we are interested in the position with respect to the global coordinate frame, which calls for a transformation of coordinates. In general, using a single camera we can only determine a ray on which the point lays. In our case, manipulation is done mainly in the plane—levitation height is small in comparison to the manipulation area. The transformation of the coordinates is then described by a *homography*.

The parameters of the transformations have to be found for the particular arrangement of the camera and the microelectrode array. To do this, a user clicks in the image on defined points for which coordinates with respect to the world coordinate frame are known. From the corresponding points, the parameters of the transformation are calculated. For a general transformation, at least four corresponding points are needed.

The image acquisition and processing introduce a delay in the feedback loop (in our case approximately 25 ms). A simple predictor is used to compensate for this delay—it estimates the current position of the particle by adding the last measured velocity multiplied by the time delay to the previously measured position.

3.3.2. Digital microscopy

Digital microscopy (digital holographic microscopy, lensless microscopy) allows computationally reconstructing the image of the scene from the hologram captured by a camera chip. Because no lens is needed, the device can be much smaller and cheaper. Some methods based on digital microscopy can estimate the positions of the particles computationally(for a review see [Yu et al., 2014, Wu and Ozcan, 2018]). The processing is usually done off-line because it is computationally demanding.

In [Gurtner and Zemánek, 2016], we propose a method based on twin-beam illumination to measure the positions of the particles. It uses two light sources as depicted in Fig. 3.14. The red LED illuminates the array from directly above and the green from an angle under 45° from vertical. In the red channel we can measure the horizontal position of the particle and from the mutual distance of particle's shadows in the red and the green channels we can measure the levitation height, as is sketched in Fig. 3.15.

If we illuminate the scene by partially coherent light, the particles create interference patterns on the chip. An example of such an image is in

---

[9]Reprinted from [Gurtner and Zemánek, 2016].
[10]Reprinted from [Gurtner and Zemánek, 2016].
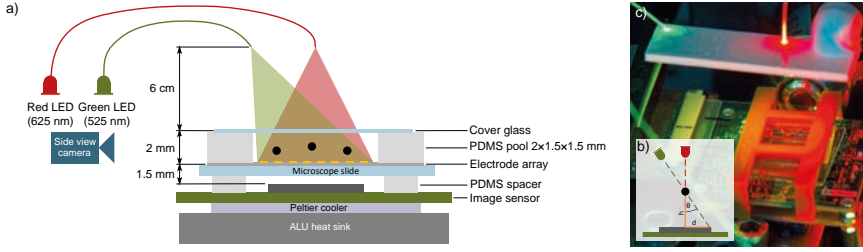
Figure 3.14.: Setup for twin-beam position estimation.[9]
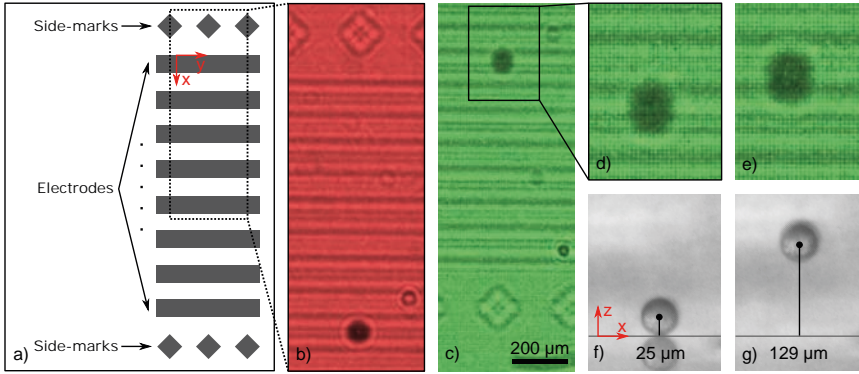
Figure 3.15.: The principle of twin-beam position estimation. a) The electrode array. b) The red channel gives information about the horizontal position. The change in the position of the shadow in the c) green channel from d) to e) corresponds to the difference in the height between f) and g).[10]

Fig. 3.16a. This image can be backpropagated to the height of the electrode array by the Rayleigh-Sommerfeld method to reconstruct the original image. We use this method not only to improve the image but also to focus particles to points which are better for detection, as it can be seen in Fig. 3.16b.

(a)

(b)

Figure 3.16.: Back propagation. (a) Image captured by the camera. (b) Image reconstructed by back propagation.

4

Mathematical modeling

The mathematical model of DEP is crucial not only because it is needed for analysis of the behavior of the control system, but also because it is a part of the feedback control loop. The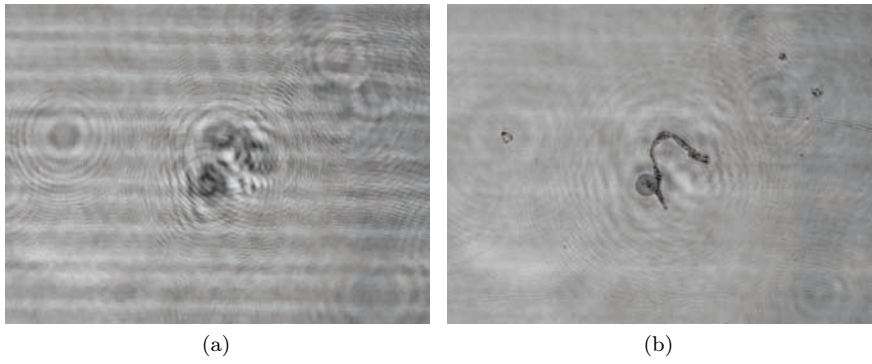 controller uses the model to find suitable voltages for the electrodes to exert a desired force on the particle in real time. Therefore, the model has to have a structure suitable for this task and it has to be computationally tractable. To simulate the motion of particles, we model the electric field $\mathbf{E}$, out of which we estimate the average DEP force that we finally incorporate into the equation of motion.

4.1. Dielectrophoresis

The dielectrophoretic force can be calculated as an interaction between the external field and the field induced by the particle. The induced field can be approximated as a field generated by a dipole and then the first-order approximation of DEP force is

$$\mathbf{F} = (\mathbf{p} \cdot \nabla) \, \mathbf{E}, \tag{4.1}$$

where $\mathbf{E}$ is the electric field and $\mathbf{p}$ defines the dipole moment. Basic assumptions for this equation are that the dipole must be small compared to the scale of non-uniformities of the electric field, and higher-order moments must be negligible. For a detailed derivation and discussion of assumptions, see, for example, [Jones, 1995]. We will consider a harmonic (i.e., sinusoidal) electric field and use a phasor notation

$$\mathbf{E} \, (\mathbf{r}, t) = \mathrm{Re} \left[\tilde{\mathbf{E}} \, (\mathbf{r}) \, e^{j\omega t} \right], \quad \tilde{\mathbf{E}} = \left[\begin{array}{c} E_{x0} \, (\mathbf{r}) \, e^{j\phi_x (\mathbf{r})} \\ E_{y0} \, (\mathbf{r}) \, e^{j\phi_y (\mathbf{r})} \\ E_{z0} \, (\mathbf{r}) \, e^{j\phi_z (\mathbf{r})} \end{array} \right], \tag{4.2}$$

where E_{x0}, E_{y0}, and E_{z0} are the amplitudes of the electric field in a Cartesian coordinate frame, ϕ_x, ϕ_y and ϕ_z are the corresponding phases, ω is the

<div style="margin-left: auto; text-align: right;">Time-average force</div>

angular frequency of the electric field, $\mathbf{r} = (x, y, z)$ is the position vector, and j denotes the imaginary unit (that is, $j = \sqrt{-1}$). An operator $\text{Re}\,[\cdot]$ returns the real part of its argument and $\tilde{\ }$ denotes a phasor.

For a homogeneous spherical particle inside this field it is possible to derive time-averaged DEP forces and then to extract the two components of this force as $\langle \mathbf{F} \rangle = \langle \mathbf{F}_{\text{cDEP}} \rangle + \langle \mathbf{F}_{\text{twDEP}} \rangle$. The operator $\langle \cdot \rangle$ denotes time average in one period. The first component

$$\langle \mathbf{F}_{\text{cDEP}} \rangle = \pi \varepsilon_m r^3 \, \text{Re}\,[K(\omega)] \, \nabla \left(E_{x0}^2 + E_{y0}^2 + E_{z0}^2 \right), \qquad (4.3)$$

is related to the gradient of the field intensity squared and the second component is induced by the gradient of the phase

$$\langle \mathbf{F}_{\text{twDEP}} \rangle = 2\pi \varepsilon_m r^3 \, \text{Im}\,[K(\omega)] \left(E_{x0}^2 \nabla \phi_x + E_{y0}^2 \nabla \phi_y + E_{z0}^2 \nabla \phi_z \right), \qquad (4.4)$$

where r is the radius of the particle and ε_m the permittivity of the medium. The frequency-dependent behavior of DEP is described by a *Clausius-Mossotti* (CM) factor[1]. For a homogeneous spherical particle, it is

$$K(\omega) = \frac{\varepsilon_p^* - \varepsilon_m^*}{\varepsilon_p^* + 2\varepsilon_m^*}, \quad \varepsilon^* = \varepsilon_0 \varepsilon_r + j \frac{\sigma}{\omega}, \qquad (4.5)$$

where ε_p^* is the complex permittivity of the particle, ε_m^* is the complex permittivity of the medium, ε_0 is the permittivity of vacuum, ε_r is the relative permittivity of the material, σ is its conductivity, and ω is the angular frequency of the applied sinusoidal voltage. Note that the CM factor is a complex number and its real part influences cDEP, while its imaginary part affects the twDEP. To make expressions compact we will collect all the parameters and the CM factor into two, frequency-dependent parameters

$$k_{\text{R}}(\omega) = \pi \varepsilon_m r^3 \, \text{Re}\,[K(\omega)], \quad k_{\text{I}}(\omega) = \pi \varepsilon_m r^3 \, \text{Im}\,[K(\omega)] \qquad (4.6)$$

When working with the phasor of the electric field, it is possible to express[2] the force as [Morgan and Green, 2002]

---

[1] Clausius-Mossotti factors capture the dynamic behavior of the polarization. The lag of the induced dipole behind the external field gives rise to twDEP. This is not the only reason for using the AC electric field in DEP; avoiding DC effects is another.

[2] To obtain and further manipulate these expressions, it is helpful to recall $\nabla \times \mathbf{E} = 0$ (because the electric field is curl-free) and $\nabla \cdot \mathbf{E} = 0$ (because of absence of the charge). Moreover, vector calculus identities are necessary, namely:
$\nabla(\mathbf{A} \cdot \mathbf{B}) = (\mathbf{A} \cdot \nabla)\mathbf{B} + (\mathbf{B} \cdot \nabla)\mathbf{A} + \mathbf{A} \times (\nabla \times \mathbf{A}) + \mathbf{B} \times (\nabla \times \mathbf{A}) = \mathbf{J}_{\mathbf{A}}^{\text{T}}\mathbf{B} + \mathbf{J}_{\mathbf{B}}^{\text{T}}\mathbf{A} = \mathbf{B} \cdot (\nabla \mathbf{A}) + \mathbf{A} \cdot (\nabla \mathbf{B})$ and $\nabla \times (\mathbf{A} \times \mathbf{B}) = \mathbf{A}(\nabla \cdot \mathbf{B}) - \mathbf{B}(\nabla \cdot \mathbf{A}) + (\mathbf{B} \cdot \nabla)\mathbf{A} - (\mathbf{A} \cdot \nabla)\mathbf{B}$.

$$\langle \mathbf{F}_{\text{cDEP}} \rangle = k_{\text{R}}(\omega) \underbrace{\nabla \left(\tilde{\mathbf{E}} \cdot \tilde{\mathbf{E}}^* \right)}_{\mathbf{a}}, \tag{4.7}$$

$$\langle \mathbf{F}_{\text{twDEP}} \rangle = -2k_{\text{I}}(\omega) \underbrace{\left(\nabla \times \left(\tilde{\mathbf{E}} \times \tilde{\mathbf{E}}^* \right) \right)}_{\mathbf{b}}, \tag{4.8}$$

where the operator $(\cdot)^*$ denotes the complex conjugate. The expression can be re-written using the following identities

$$\begin{aligned}
\mathbf{a} &= \nabla \left| \tilde{\mathbf{E}} \right|^2 = \nabla \left(\text{Re} \left[\tilde{\mathbf{E}} \right]^2 + \text{Im} \left[\tilde{\mathbf{E}} \right]^2 \right), \\
\mathbf{b} &= \left(\nabla \times \left(\text{Re} \left[\tilde{\mathbf{E}} \right] \times \text{Im} \left[\tilde{\mathbf{E}} \right] \right) \right).
\end{aligned} \tag{4.9}$$

We found it useful for simulations to have those expressions in the form with partial derivatives of the electric field. Moreover, they reveal the similarity between cDEP and twDEP. Single x-components of $\mathbf{a}$ and $\mathbf{b}$ are

$$\begin{aligned}
a_x &= 2 \sum_{a=x,y,z} \left(\text{Re} \left[E_a \right] \text{Re} \left[\frac{\partial E_a}{\partial x} \right] + \text{Im} \left[E_a \right] \text{Im} \left[\frac{\partial E_a}{\partial x} \right] \right), \\
b_x &= \sum_{a=x,y,z} \left(\text{Im} \left[E_a \right] \text{Re} \left[\frac{\partial E_a}{\partial x} \right] - \text{Re} \left[E_a \right] \text{Im} \left[\frac{\partial E_a}{\partial x} \right] \right),
\end{aligned} \tag{4.10}$$

and expressions for y- and z-components can be obtained by an appropriate change of the index. Let us note that it is not a good idea to use (4.4) for simulations because it contains the gradient of phase, but the phase is periodical and thus discontinuous.

4.2. Electric field

We started our discussion by introducing the approximative model of DEP, but to get the average DEP force, we first need the electric field. Simulation of the electric field for a homogeneous, isotropic, nondispersive, linear material, for which we can assert $\mathbf{D} = \varepsilon \mathbf{E}$, and in the absence of a free charge, can be accomplished by solving Laplace's equation for electric potential Φ ($\mathbf{E} = -\nabla \Phi$)

$$\nabla^2 \Phi = 0. \tag{4.11}$$

Since we are considering a harmonic single-frequency voltage, a phasor can be used for describing the potential at a given position $\mathbf{r} = (x, y, z)$ and time t

$$\Phi(\mathbf{r}, t) = \mathrm{Re}\left[\tilde{\Phi}(\mathbf{r})\, e^{j\omega t}\right], \quad \tilde{\Phi} = \Phi_{\mathrm{R}} + j\Phi_{\mathrm{I}}. \tag{4.12}$$

The real and imaginary parts Φ_{R} and Φ_{I} give information about the magnitude and the phase of the potential. Laplace's equation holds for both the real and the imaginary parts of the potential

$$\nabla^2 \Phi_{\mathrm{R}} = 0, \quad \nabla^2 \Phi_{\mathrm{I}} = 0. \tag{4.13}$$

Boundary conditions   To complete our problem definition, we consider the following boundary conditions. If the upper boundary (surface) of the simulated area is sufficiently high, both the electric potential and the electric field go to zero, fulfilling the Dirichlet ($\Phi = 0$) or Neumann ($\partial\Phi/\partial\mathbf{n} = 0$) boundary condition. The vector $\mathbf{n}$ stands for the normal vector of the boundary. The same holds for the boundary conditions on the sides.

Since the thickness of the electrodes is more than about one hundred times smaller than the the dimension of electrodes and gaps, we consider the electrodes to be infinitely thin. The voltages applied to the electrodes define the boundary conditions at the bottom surface of the simulation domain.

Finally, it is necessary to find the boundary conditions for the space between the electrodes. The general condition is that the potential and the normal component of the total current have to be continuous at the interface between the substrate and the medium. For water and glass, this can be simplified by setting a Neumann boundary condition for the potential ($\partial\Phi/\partial\mathbf{n} = 0$), and the solution space can be reduced to just the medium without the substrate. See [Green et al., 2002].

Numerical solution   A numerical solution for Laplace's equation is found with a commercial finite-element-method (FEM) solver (COMSOL Multiphysics®). Averaged cDEP and twDEP forces are computed from the field variable (electric potential) and the derived field variable (electric field $\mathbf{E}$) in the postprocessing.

Nonetheless, there has been a systematic effort to develop some analytical models which at least roughly approximate the dynamics of the problem; that is, the DEP/twDEP force field induced by the electric field. The inspiration comes from [Masuda and Kamimura, 1975], but the first investigation that takes into consideration the geometry of the electrodes (at least partially)

can be found in a few papers such as [Wang et al., 1996], where Green's theorem is invoked, [Morgan et al., 2001], where truncated Fourier series are used, [Green et al., 2002], where finite element method modeling is analyzed thoroughly, and finally [Chang et al., 2003] where a closed form approximation to the DEP/twDEP is given.

4.3. Model for control system

Now, we will rearrange the mathematical model to a form suitable for the control system, which means we want to separate how the force evolves with the input voltages and with the position. If we apply the gradient operator in (4.7), we get the $x-$, $y-$, and $z-$components of the force as

$$F_{\text{cDEP},a} = k_{\text{R}}\left(\omega\right)\left(\frac{\partial \tilde{\mathbf{E}}^{\text{T}}}{\partial a}\tilde{\mathbf{E}}^{*} + \tilde{\mathbf{E}}^{\text{T}}\frac{\partial \tilde{\mathbf{E}}^{*}}{\partial a}\right), \, a \in \{x, y, z\}. \tag{4.14}$$

From now on, we will use only time-average DEP force so we dropped the operator $\langle\cdot\rangle$. To evaluate this expression, we need to know the electric intensity at a given location and also its spatial derivatives. As was mentioned, we can calculate the field using a FEM solver. Nevertheless, the FEM model requires a new simulation for every new potential. To reduce the FEM-related computational load, we exploit the principle of *superposition* for the electric potential. In our case, the boundary conditions can be expressed as a linear combination of a small number of basic boundary conditions (forming a basis). Accordingly, the electric potential can be composed as a linear combination of potentials related to those basic boundary conditions. There is then no need to repeat the FEM simulations. This approach was inspired by a *hybrid model* described in [Kharboutly et al., 2009]. The only disadvantage is that we have to store the basis in memory. To relieve these storage requirements, [Gurtner et al., 2017] propose an approximation of the boundary conditions allowing the use of a Green's function to find the solution.

To get the basis of solutions, we apply a unit potential consecutively to each of the n electrodes while keeping the remaining electrodes at a zero potential. The resulting set of solutions Φ_{i} $(i = 1, 2, \cdots, n)$ is then used to compose the solution for an arbitrary boundary condition through a linear combination

$$\tilde{\Phi}(\mathbf{r}) = \sum_{i=1}^{n} \tilde{\Phi}_i(\mathbf{r}) = \sum_{i=1}^{n} \Phi_{\mathrm{i}}(\mathbf{r})\tilde{u}_i, \tag{4.15}$$

where $\tilde{\Phi}_i(\mathbf{r})$ is a potential contribution of the i-th electrode and $\tilde{u}_i$ is a voltage phasor representing the signal applied to the ith electrode. The resulting electric potential $\tilde{\Phi}(\mathbf{r})$ is a complex number and thus also marked with $\tilde{\ }$ as a phasor. The summation above can be more compactly written as $\tilde{\Phi} = \mathbf{\Phi}^{\mathrm{T}}\tilde{\mathbf{u}}$, where $\tilde{\mathbf{u}}$ is a column vector composed of individual $\tilde{u}_i$'s stacked one on the top of another and $\mathbf{\Phi}$ is in the same way composed of Φ_{i}'s (please note that we drop the function arguments in some expressions to make them clearer). Similarly, we can also express the electric field as

$$\tilde{\mathbf{E}} = - \begin{bmatrix} \frac{\partial \tilde{\Phi}}{\partial x} \\ \frac{\partial \tilde{\Phi}}{\partial y} \\ \frac{\partial \tilde{\Phi}}{\partial z} \end{bmatrix} = - \begin{bmatrix} \sum_{i=1}^{n} \frac{\partial \Phi_{\mathrm{i}}}{\partial x}\tilde{u}_i \\ \sum_{i=1}^{n} \frac{\partial \Phi_{\mathrm{i}}}{\partial y}\tilde{u}_i \\ \sum_{i=1}^{n} \frac{\partial \Phi_{\mathrm{i}}}{\partial z}\tilde{u}_i \end{bmatrix} = - \underbrace{\begin{bmatrix} \frac{\partial \Phi_1}{\partial x} & \frac{\partial \Phi_2}{\partial x} & \cdots & \frac{\partial \Phi_n}{\partial x} \\ \frac{\partial \Phi_1}{\partial y} & \frac{\partial \Phi_2}{\partial y} & \cdots & \frac{\partial \Phi_n}{\partial y} \\ \frac{\partial \Phi_1}{\partial z} & \frac{\partial \Phi_2}{\partial z} & \cdots & \frac{\partial \Phi_n}{\partial z} \end{bmatrix}}_{\mathbf{\Gamma}^{\mathrm{T}}} \tilde{\mathbf{u}}, \tag{4.16}$$

The matrix $\mathbf{\Gamma}$ is composed of spatial derivatives of basis elements. In other words, the matrix $\mathbf{\Gamma}$ is the *Jacobian* of the vector $\mathbf{\Phi}$. Differentiation is performed numerically in advance during preprocessing and the results are stored to be readily available during online model evaluation. Along the same lines, we express the spatial derivatives of the electric potential

$$\frac{\partial \tilde{\mathbf{E}}}{\partial a} = - \underbrace{\begin{bmatrix} \frac{\partial^2 \Phi_1}{\partial x \partial a} & \frac{\partial^2 \Phi_2}{\partial x \partial a} & \cdots & \frac{\partial^2 \Phi_n}{\partial x \partial a} \\ \frac{\partial^2 \Phi_1}{\partial y \partial a} & \frac{\partial^2 \Phi_2}{\partial y \partial a} & \cdots & \frac{\partial^2 \Phi_n}{\partial y \partial a} \\ \frac{\partial^2 \Phi_1}{\partial z \partial a} & \frac{\partial^2 \Phi_2}{\partial z \partial a} & \cdots & \frac{\partial^2 \Phi_n}{\partial z \partial a} \end{bmatrix}}_{\mathbf{\Lambda}_a^{\mathrm{T}}} \tilde{\mathbf{u}}, \ a \in \{x, y, z\}, \tag{4.17}$$

and this means that the matrix $\mathbf{\Lambda}_a$ is the Jacobian of the vector of electric fields along the a-axis. Now we can substitute (4.16) and (4.17) into (4.14) to get

$$\boxed{F_{\mathrm{cDEP},a} = \tilde{\mathbf{u}}^{\mathrm{T}} \underbrace{k_{\mathrm{R}}\left(\omega\right)\left(\mathbf{\Lambda}_a\mathbf{\Gamma}^{\mathrm{T}} + \mathbf{\Gamma}\mathbf{\Lambda}_a^{\mathrm{T}}\right)}_{\mathbf{P}_a(\omega,\mathbf{r})} \tilde{\mathbf{u}}^{*}, \ a \in \{x, y, z\},} \tag{4.18}$$

where the inputs stacked into $\tilde{\mathbf{u}}$ are expressed explicitly. The matrix $\mathbf{P}_a$ depends on the position of the particle (through the electric intensity and its

spatial derivatives), the frequency of the applied voltage, and the material properties (through the k_R term). The rank of the matrix is at maximum 6 because each summand has the rank at maximum 3.

Using the vector calculus identity

$$
\nabla \times \left(\tilde{\mathbf{E}} \times \tilde{\mathbf{E}}^* \right) = \tilde{\mathbf{E}} \underbrace{\left(\nabla \cdot \tilde{\mathbf{E}}^* \right)}_{=0} - \tilde{\mathbf{E}}^* \underbrace{\left(\nabla \cdot \tilde{\mathbf{E}} \right)}_{=0} +
$$
$$
+ \left(\tilde{\mathbf{E}}^* \cdot \nabla \right) \tilde{\mathbf{E}} - \left(\tilde{\mathbf{E}} \cdot \nabla \right) \tilde{\mathbf{E}}^*, \tag{4.19}
$$

we can express the twDEP force from (4.8) in a form suitable for the control system.

$$
F_{\text{twDEP},a} = \tilde{\mathbf{u}}^T \underbrace{2 k_I \left(\omega \right) \left(-\mathbf{\Lambda}_a \mathbf{\Gamma}^T + \mathbf{\Gamma} \mathbf{\Lambda}_a^T \right)}_{\mathbf{Q}_a(\omega, \mathbf{r})} \tilde{\mathbf{u}}^*, \ a \in \{x, y, z\}. \tag{4.20}
$$

Through the precomputed electric potentials and their spatial derivatives, the DEP force can be evaluated in real time even for electrode arrays for which an analytical solution is unavailable. However, the more electrodes the array has and the larger it is, the bigger the precomputed dataset will be. Geometric symmetry of the array could be exploited, if possible, but in any event it was not necessary in our case.

4.4. Limitations of the model

4.4.1. Other effects

The presented mathematical model describes DEP, but in reality other phenomena can effect the motion of the particles in the electric field. For example, electrophoresis, electroosmosis, the thermal gradient-induced fluid flow, the mutual electrokinetic and hydrodynamic interactions, etc. Thus, during experiments we have to find suitable conditions to avoid unmodelled effects. If another effect, like mutual interaction of particles, starts to be pronounced, it is necessary to incorporate it into the mathematical model. [Lin et al., 2006] show a DEP simulation that incorporates particle-particle interactions. Nevertheless, the feedback itself introduces some degree of insensitivity to the discrepancy between the model and the reality (also called robustness).

4.4.2. Dipole approximation

The mathematical model (4.1) assumes that the induced dipole is small compared to the scale of non-uniformities of the electric field and that higher-order moments are negligible. Therefore, it is only an approximation in our case when the size of the particle and electrodes are comparable. The only way to obtain an accurate force is a calculation based on the *Maxwell stress tensor* (MST). The force acting on a particle in an electromagnetic field is

$$\mathbf{F} = \oint_A (\mathbf{T} \cdot \mathbf{n}) \, \mathrm{d}A \tag{4.21}$$

where A is the surface enclosing the volume V. $\mathbf{T}$ is the Maxwell stress tensor given by

$$\mathbf{T} = \epsilon(\mathbf{E} \otimes \mathbf{E} - \frac{1}{2}\mathbf{E}^2\mathbf{U}) + \mu(\mathbf{H} \otimes \mathbf{H} - \frac{1}{2}\mathbf{E}^2\mathbf{U}), \tag{4.22}$$

where $\mathbf{U}$ is the unit tensor. In our case, we do not have to consider the magnetic field $\mathbf{H}$. Evaluation of the force using MST is computationally demanding and therefore it is infeasible for real-time control. However, MST provides a good reference value.

[Rosales and Lim, 2005] performed a comparison of different levels of DEP approximation with the accurate solution resulting from MST. Based on the stated guidelines, the point-dipole approximation could have a non-negligible error in our case, because the manipulated particles are comparable in size to the electrodes. However, in [Michálek and Zemánek, 2017] we performed a detailed verification of the model by comparing the point-dipole and higher-order approximations to both the MST and the experimental results, and concluded that the dipole model is sufficiently accurate for control purposes. The discrepancy in the conclusions deserves further attention.

Table 4.1 shows memory and time requirements for the different orders of approximation compared to the Maxwell stress tensor. The values were measured for the 3D model of a planar electrode array with eight electrodes. We see that one order increases time and memory requirements approximately two times. To relieve the memory requirement, [Gurtner et al., 2017] suggest a model based on a Green's function.

---

[3]Reprinted from [Michálek and Zemánek, 2017].

Table 4.1.: Time and memory requirements for evaluation of different models.[3]

Method	MST	Dipole	Quadrupole	Octupole
Evaluation	20 min	0.42 ms	0.88 ms	1.8 ms
Preparation		5.9 h	11 h	16.7 h
Memory	5 GB	130 MB	240 MB	370 MB

4.5. Dynamic model

To simulate the motion of the particles we need a dynamic model. We will examine the main forces that influence the motion of the particle in a liquid medium. The first is the DEP force, for which we already have the mathematical model. Then gravity and buoyancy act together as a sedimentation force

$$F_{\text{sed}} = \frac{4}{3}\pi r^3 \left(\rho_{\text{p}} - \rho_{\text{m}}\right) g, \tag{4.23}$$

where r is the radius of the particle, ρ_{p} and ρ_{m} are the densities of the particle and the medium, respectively, and g is the acceleration due to gravity. A homogeneous spherical particle moving though a viscous liquid experiences the frictional force known as Stoke's drag

$$F_{\text{d}} = 6\pi\mu r v \tag{4.24}$$

where μ is the dynamic viscosity of the medium and v is the velocity of the particle. This law assumes that the particle moves in free space. In the vicinity of walls, it is possible to use a correction factor as shown, for example, in [Happel and Brenner, 1983]. For a low Reynolds number, the shape becomes less important and Stoke's law gives a good prediction of the force. In small scale, we can neglect inertia of the particle [Kharboutly et al., 2009]. This means that the particle reaches its terminal velocity almost instantaneously and the velocity is determined by Stoke's law. Thus the equation of motion is

$$\dot{\mathbf{x}} = \frac{\mathbf{F}_{\text{sum}}}{k_\mu}, \quad \mathbf{F}_{\text{sum}} = \mathbf{F}_{\text{DEP}} + \mathbf{F}_{\text{sed}}. \tag{4.25}$$

5

Control

The ultimate goal of the control algorithm is to steer one or several particles (simultaneously and independently) along arbitrary trajectories. Since for practical purposes these trajectories can be reasonably well approximated by polygonal chains, the task can be reduced to steering the particles through all the vertices of the polygonal chain in a given order, thus following the approximated trajectory. So the main goal is to get particles into the desired locations using DEP force.

From the mathematical model, (4.7) and (4.8), we know that for fixed material properties (the permittivity and the conductivity of the particle and the medium), the only way to control the DEP force is through a change of the external electric field. This calls for a variation in the frequency, amplitudes, or mutual phase shifts of the voltages on the electrodes. The frequency affects the induced dipole. Thus it can scale the DEP force and change its sign, though this is not guaranteed because it depends on the electrical properties of the material.

The direction of the force can be controlled through a variation of the amplitude and/or the phase shift. A common description of cDEP is such that it depends on the gradient of the electric field squared, and twDEP depends on the gradient of the phase. It is then natural to conclude that a modulation of the amplitude controls cDEP whereas a phase modulation controls twDEP, but this reasoning is misleading. Indeed, the amplitude modulation of a single-phase signal can change only the real part of the electric field while leaving the imaginary part zero. Thus it is possible to induce and control only cDEP. However, modulation of the phase changes both the real and imaginary part. As a result, we can control both cDEP and twDEP, and phase modulation extends the set of achievable forces.

While the use of amplitude modulation for controlling cDEP is well documented in the literature, using a variable phase shift for controlling cDEP is rarely reported. We have not found a paper reporting phase

modulation for feedback control of cDEP. This is somewhat striking since generating a periodic voltage with a determined phase shift—in particular, a square wave—is much easier than generating a periodic signal with variable amplitude.

In this chapter, we will discuss several control systems that we have developed. The first uses a predefined alphabet of fields. Next, we will show optimization-based feedback control using amplitude modulation and a basic parallel electrodes array. This array allows presenting a new concept of noise-aided manipulation that enables parallel manipulation even in the case when it should not be theoretically possible. The last controller uses phase modulation and the four-sector microelectrode array for parallel manipulation of several particles.

5.1. Predefined fields

To manipulate particles, it is possible to use an alphabet of predefined settings of voltages. These settings constitute a set of elemental moves from which the desired trajectory is composed. We will show both open-loop and feedback strategies, based on predefined fields.

5.1.1. Basic moves

We demonstrate the predefined fields on the four-sector array. This electrode array is capable of inducing a translation motion across the electrodes and also along the *diagonal interface* between the triangular *electrode sectors*, as shown in Fig. 5.1a. The path of the particle must be composed from these two basic movements[1]. As a result, the particle can reach an arbitrary final position starting at any initial position, but it cannot travel along an arbitrary path. An example of a realizable path is in Fig. 5.1b.

With the presented control strategy, we participated in the "Mobile Microrobotics Challenge"[2]. The layout of the four-sector microelectrode array was adjusted to meet the requirements of the contest, but the control strategy works with the original layout as well.

---

[1]This holds only for predefined fields, but the optimization-based control presented later can steer a particle along an arbitrary path.

[2]Mobile Microrobotics Challenge (MMC) is organized to bring together research teams in microrobotics. The task we had to solve was to steer a microrobot along a figure-eight path in a $2.5 \times 3.5\,\text{mm}$ arena as fast as possible. MMC was originally proposed and organized by the National Institute of Standards and Technology (NIST) and in 2013 it was delegated to the IEEE Robotics and Automation Society (RAS). MMC has
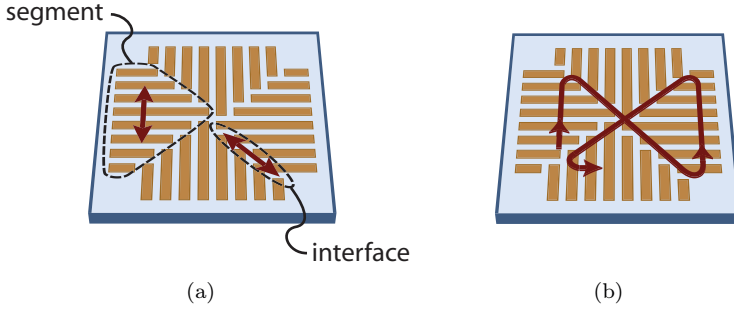
Figure 5.1.: (a) Elemental motions on the four-sector array perpendicular to
the electrodes and also the diagonal interfaces. (b) An example
of a realizable path.

.

The basic fact upon which the control strategy is based is that using
negative cDEP it is possible to push the particle away from edges of a
specific electrode when the electrode is *activated*. Activation means that the
electrode has a potential different from the one on the neighboring electrodes.
In particular, the potential differs just in the phase shift (amplitude and
frequency are always kept identical in the presented control strategy). Note
that this can be implemented by the generator described in Section 3.2.2.

By sequentially activating individual electrodes of one *sector*, the particle
can be moved perpendicularly to the electrodes as shown in Fig. 5.2, where
the velocity vector field at the height of 125 µm above the electrodes, together
with the phases on the electrodes, is shown. This specific height was selected
because it approximately agrees to the levitation height of the (center of
gravity of the) particle.

If the particle is situated in a gap between several electrodes with potentials
of different phase, it is steered to the spot with zero gradient of the electric
field (if there is one). This way the particle can be steered *along the diagonal
interface*. Phase shift settings in two consecutive steps are shown in Fig. 5.3.
Full motion along the diagonal can be established by moving these nDEP
potential cages.

---

been held during the IEEE International Conference on Robotics and Automation
(ICRA) every year since 2010 [Popa, 2014]

[3]Reprinted from [Zemanek et al., 2014].

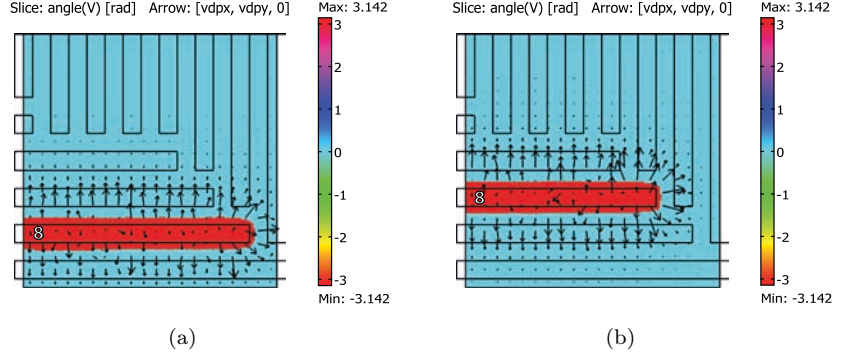[4]Reprinted from [Zemanek et al., 2014].

Figure 5.2.: Motion above the sector. (a) The particle is repelled from the edge of the electrode upwards and (b) the neighboring electrode is activated to push the particle further. Arrows show direction and magnitude of the velocity vector at a height of 125 µm above the electrodes; color stands for the phase on the electrodes. The number above the electrode near the border stands for the phase shift, so that value n corresponds to phase $n\pi/8$. If the number is not stated then $n = 0$.[3]
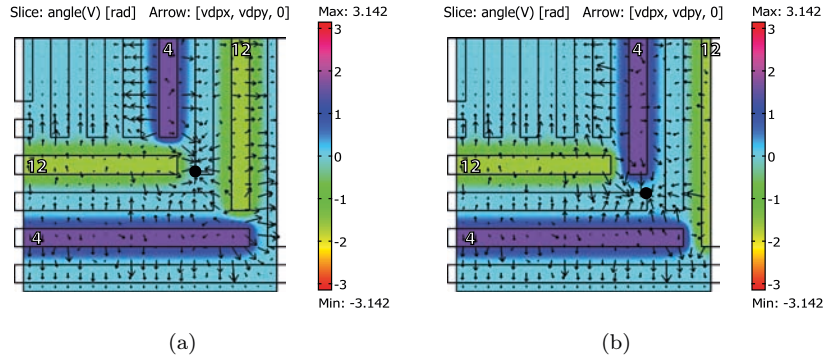

Figure 5.3.: Motion along the diagonal interface. (a) The particle establishes its position at the tip of one electrode. (b) Afterwards, the particle is attracted toward the tip of the neighboring electrode.[4]

The presented steps are organized in a sequence to achieve the desired path. A significant advantage of such an approach is that it does not necessarily need feedback from the position of the particle because the final, stable position of the particle is known for each step. Therefore, it suffices to find a suitable sequence of settings of potentials and then go through this sequence slowly enough to give the particle enough time to reach the final position. This open-loop control may, of course, turn out very conservative (slower then it is necessary) and then feedback control is required.

5.1.2. Experimental results

Both the platform and the control strategy were tested experimentally. The widths of the electrodes and the interelectrode gaps is $100\,\mu\text{m}$. The experiments were conducted with a $250\,\mu\text{m}$ polystyrene bead immersed in deionized water. The bead was placed near to the starting position using a pipette and fine positioning was done using cDEP. Then the preprogrammed sequence of phase shift settings was replayed in such a way that transitions between steps were manually triggered by the human operator, who observed the scene. The generator was set to provide square wave voltages with an amplitude of $7.5\,\text{V}$ (off state $0\,\text{V}$, on state $15\,\text{V}$), a frequency of $300\,\text{kHz}$, and a $50\,\%$ duty cycle.

The particle represented by the polystyrene bead followed the figure-eight path as shown in Fig. 5.4. The total length of the path is $9.2\,\text{mm}$ and the particle was able to finish it in approximately $30\,\text{s}$ which gives an average speed of $0.3\,\text{mm}\,\text{s}^{-1}$. The velocity computed by numerical simulations was approximately $0.15\,\text{mm}\,\text{s}^{-1}$. The instantaneous speed of the particle fluctuates according to its position. This observation corresponds to the simulations as the generated force is not uniform.

5.1.3. Trajectory planning

The sequence of the steps in the previous section was programmed manually. Here we will describe a systematic approach for planning of the phase sequence. For this purpose, the position is discretized to a grid given by the electrodes; each electrode and each gap constitute one column or row. We use basic phase configurations presented in the previous section to move the particle between these discrete positions. For motion above the sectors, one activated electrode pushes the particle as shown in Fig. 5.5a. Four electrodes

---

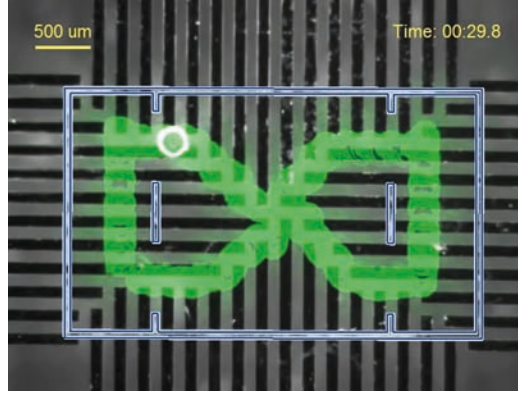[5]Reprinted from [Zemanek et al., 2014].   Video available at http://youtu.be/Dq-1apN3sBI.

Figure 5.4.: The path of the particle (250-micron polystyrene bead). The entire figure-eight is finished in 30 s, which gives an average speed of $0.3\,\mathrm{mm\,s^{-1}}$.[5]

with suitable phase shifts create a potential cage that can be shifted along the interface as shown in Fig. 5.5b. Small red arrows in the pictures denote transitions between positions that the particular setting causes.

From those basic steps, we can construct a directed graph where vertices represent positions and edges represent transitions induced by the particular setting of phases. A part of such a graph is in Fig. 5.6. This graph can be used for planning an optimal trajectory to the desired position. We precalculated an optimal next step for each pair of the current position and the desired position. We also integrated this planning with feedback from the camera. Thus, at every moment, the controller picks an optimal setting of phases according to the desired location.

5.2. Amplitude modulation

For feedback control of the position of the particles, it is convenient to set directly the forces acting upon them. These are, however, nonlinearly dependent on the voltages applied to the electrodes, and on the position of the particles. The model (4.18) calculates the DEP force for a given position $\mathbf{r}$ and voltages $\tilde{\mathbf{u}}$, but we need to invert it.

---

[6]Reprinted from [Drs, 2015].
[7]Reprinted from [Drs, 2015].

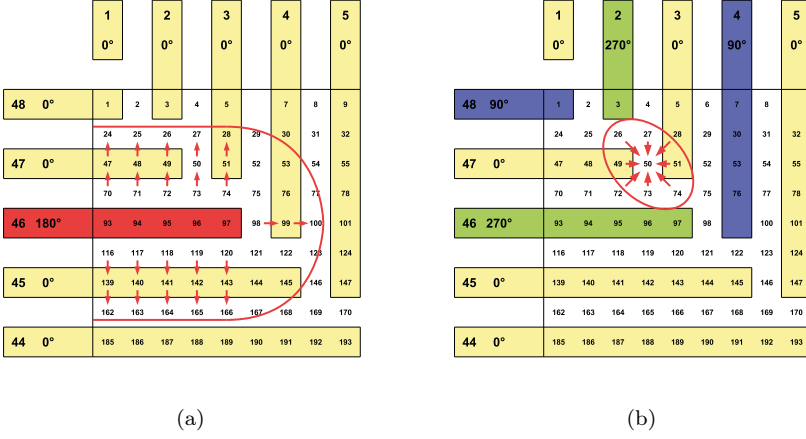(a)   (b)

Figure 5.5.: Basic phase settings for a four-sector array for motion a) above the sector and b) along the interface. Small red arrows represent induced transition between positions.[6]
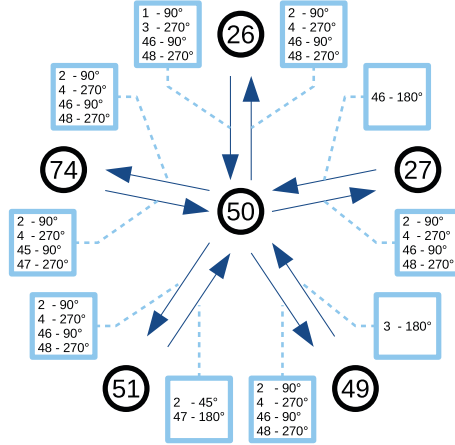

Figure 5.6.: Part of the oriented graph for trajectory planning on the four-sector array.[7]

5. Control

To demonstrate control of DEP using amplitude modulation, we will use a basic parallel electrode array. It allows us to demonstrate parallel manipulation even in a constrained field. Since in this case the electric field is constant along the electrodes, we only consider a planar cross-section. Then x represents the coordinate along the horizontal direction orthogonal to the electrodes and z stands for the levitation height. Nevertheless, the presented algorithm works in three dimensions as well.

If only amplitude modulation is used, a vector of the voltages $\mathbf{u}$ is real and the model for cDEP is in a simpler form

$$F_{\text{cDEP},a} = \mathbf{u}^{\text{T}} \underbrace{2k\left(\omega\right)\left(\mathbf{\Lambda}_a \mathbf{\Gamma}^{\text{T}}\right)}_{\mathbf{P}_a} \mathbf{u},\ a \in \{x, y, z\}, \tag{5.1}$$

and the total force acting on the particle also has to include the sedimentation force

$$\mathbf{F}_{\text{sum}}(\mathbf{r}, \tilde{\mathbf{u}}) = \mathbf{F}_{\text{cDEP}}(\mathbf{r}, \tilde{\mathbf{u}}) + \mathbf{F}_{\text{sed}}. \tag{5.2}$$

Now the task is to find the potentials $\mathbf{u}$ on the electrodes that will yield the desired DEP force $\mathbf{F}_{\text{des}}$ at a given position $\mathbf{r}$. This can be formulated as an optimization task that is solved numerically during every *sampling period* of the controller (every fraction of a second, $100\,\text{ms}$ in our case)

$$\begin{aligned} \underset{\mathbf{u}}{\text{minimize}} \quad & \|\mathbf{F}_{\text{sum}}(\mathbf{r}, \tilde{\mathbf{u}}) - \mathbf{F}_{\text{des}}\|, \\ \text{subject to} \quad & |u_i| < U_{\text{max}}. \end{aligned} \tag{5.3}$$

This way it is possible to obtain voltages $\mathbf{u}$ necessary to induce the desired force. The matrix $\mathbf{\Lambda}$ is composed of contributions of individual electrodes to the electric field as expressed in (4.16), and the matrix $\mathbf{\Gamma}$ is composed of the partial derivatives of those individual contributions, as shown in (4.17). The advantage of this formulation is that the field of individual electrodes and its partial derivatives are calculated for the given electrode array only once.

The optimization problem is nonconvex, which makes the problem computationally challenging. For solving it, we currently apply a *simulated annealing* algorithm[8]. This solution is satisfactory concerning the computational speed, but the solver provides no guarantee of reaching the global optimum—there is a possibility of becoming stuck at a local minimum. Hence, further investigation on the algorithmic side can improve the overall performance.

---

[8]The code written by J. Vandekerckhove is freely available at *MATLAB central*.
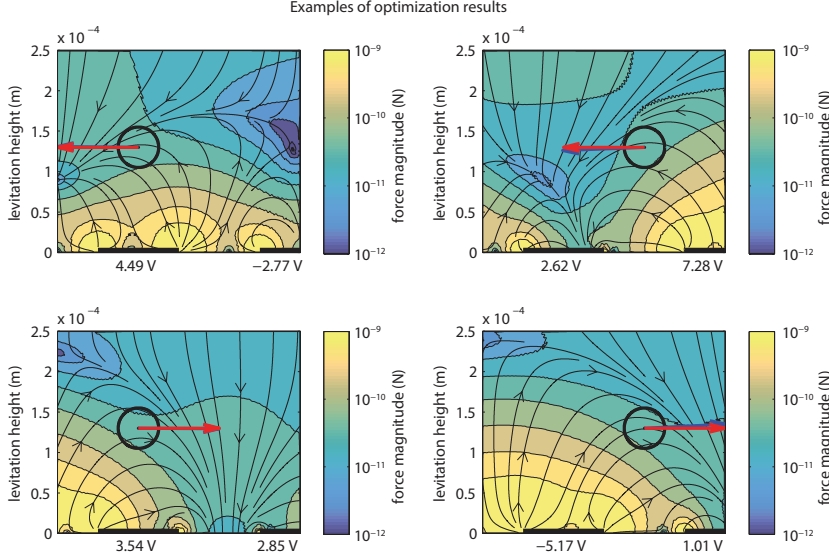
Figure 5.7.: Four examples of the optimization results: the plots show a side view of a section of the manipulation area containing the particle. The red arrow stands for the requested force, and the blue one shows the force resulting from the voltages applied to the electrodes and found by numerical optimization. The background color plot represents a magnitude of the force.[9]

Results of the optimization in various situations are shown in Fig. 5.7 as side views of a sector of the manipulation area containing the particle at two different positions and with two different desired forces (red arrows). Blue arrows then represent the force achieved by the optimization over the voltages. Although the two arrows do not overlap perfectly, this performance is sufficient to be used with the real system in a feedback manner.

It is possible to add other physical effects to the control scheme in the future. For example, hydrodynamic forces resulting from the interaction of the particles or the presence of the walls can be added as external forces similar to $\mathbf{F}_{\mathrm{sed}}$. However, it must be possible to calculate these forces within every sampling period. Incorporating the mutual interaction of the particles

---

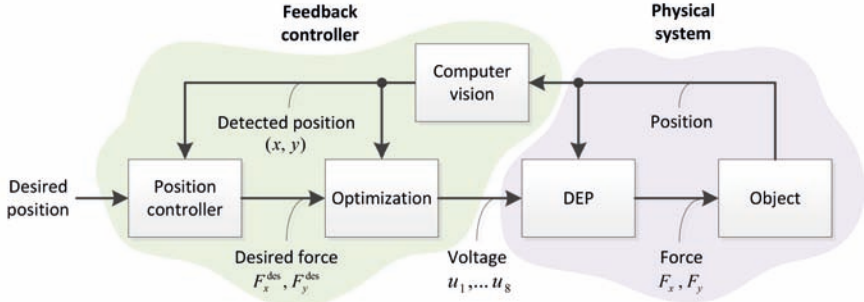[9]Reprinted from [Zemánek et al., 2015].

Figure 5.8.: Block diagram of the feedback controller.[10]

through the electric field would be possible through a model of dipole-dipole interaction. That would lead to a change in the computation of the $\mathbf{P}_a$ matrix. The model could be further improved by extending the dipole approximation to the more accurate multipole one, which would change the calculation of matrix $\mathbf{P}_a$ by requiring higher-order derivatives.

5.3. Position control

A position controller acquires a measurement of the position of the particle, compares it with the desired (reference) position, and computes the desired force, which is then forwarded to the optimization block. This is done every sampling period. In our case we only use a proportional part of a general PID controller; this means that the force is proportional to the position error. The output of the controller (the desired force) is limited to 100 pN because of constraints on the achievable amplitude of voltage.

The position coordinates and the components of the desired force vector are then used as the input parameters to the optimization task. The voltages are the outputs of the optimization and are applied to the electrodes. A block diagram of the feedback controller is in Fig. 5.8.

This system successfully controls the x-position even without measurement of the levitation height. We fixed the F_z^{des} component to zero and the position z to the desired levitation height. This means that the controller attempts to maintain the desired levitation height by creating an equilibrium of vertical forces at the given height z. But if the particle does not reach the required

---

[10]Reprinted from [Zemánek et al., 2015].

height, the controller has no information about it. This could only be resolved by measuring the levitation height.

The computer vision algorithm feeds the horizontal position into the feedback controller. However, this information is delayed. It takes a finite time to acquire the image and then process it and execute the control algorithm. This delay has to be compensated, otherwise, it can cause undesired behavior, such as oscillations in our case. We tackle this problem using a simple position estimator mentioned in Section 3.3.1.

5.3.1. Experiments

The experiments were conducted with 50-micron polystyrene micro-beads in deionized water. The applied sinusoidal voltage had a maximum amplitude of 10 V and a frequency of 300 kHz, which induced a negative DEP. This frequency was selected to avoid low-frequency electrokinetic effects and to remain within the bandwidth of the voltage multipliers (1 MHz).

Experiments started with sinusoidal voltages with amplitudes of 10 V and phases of 0° and 180° applied alternately to the electrodes. This set all the particles to levitation at the known height (130 μm).

A selected particle was then steered along a user-defined trajectory (orthogonal to the electrodes). Although the controller does not have the measurements of the levitation height, and the FEM model used to construct the matrices $\mathbf{P}_x(\mathbf{r})$ and $\mathbf{P}_z(\mathbf{r})$ in the optimization (5.3) is not perfectly accurate, the particle followed the reference position fairly well. The worst-case steady-state errors are up to 20 μm at some locations (see Fig. 5.9A).

The error in positioning, that is, the difference between the desired and true position, was also evaluated statistically. Various desired positions were set and the mean value and the standard deviation of the absolute value of the errors were calculated. These values for different positions above the electrode array are shown in Fig. 5.9B. The error is greater above the edges of electrodes and towards the end of the manipulation area, but is around 20 μm within the range of manipulation. This value can also be expressed in the number of pixels (5 px), or related to the size of the micro-sphere (40 %), or to the manipulation range of 1.2 mm (1.8 %).
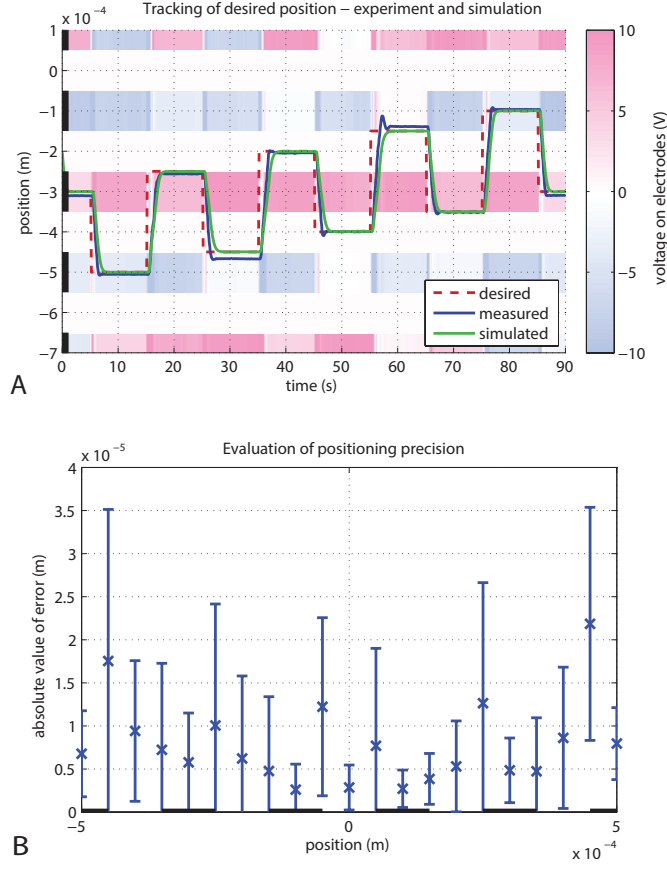
---

[11]Reprinted from [Zemánek et al., 2015].

Figure 5.9.: A) Feedback control of the position of a single particle using numerical optimization and a PID regulator. Black line segments on the vertical axis show the positions of the electrodes, and the horizontal color strips to the right of them represent the voltage amplitudes set on them at given times (negative values mean counter-phase). B) Evaluation of the error of the position. The desired position was set to various places above the electrode array, and the errors of the real position were then processed statistically.[11]

5.4. Noise-aided manipulation

The presented optimization-based approach can be extended to independent manipulation of several particles at the same time. Computationally this extension is straightforward—new terms for the desired forces appear in the criterion in the numerical optimization (5.3). However, unless the electrodes form a dense, matrix-like array, with each electrode addressable independently, it may happen that the force developed at one place restricts the freedom of setting an arbitrary force at another place over the electrode array. This may then pose a problem from a *controllability* viewpoint. Two identical particles located at these positions cannot be manipulated independently since they are exposed to forces of an identical magnitude and direction. This illustrates the loss of the controllability property of the system, which is a major problem that no deterministic control algorithm can overcome. We can visualize this problem on the array of parallel microelectrodes. Two (or more particles) distributed along a given electrode will feel the same force, regardless of voltages on the electrodes. Hence it appears they cannot be manipulated independently.

Although we have stated that control theory currently gives a negative answer to the quest for control under the above-stated conditions, we are still able to offer a solution, albeit a probabilistic one. The two particles start at the same position (in a stable force equilibrium), which can be viewed as if they were placed at the bottom of a potential well (see Fig. 5.10A). Then we switch the potential landscape (by changing the voltages on the electrodes) so that the two particles find themselves in an unstable equilibrium (on top of a potential hill). Now, with the random noise intrinsic in the system there is a chance that the particles will start moving in different directions and we achieve the needed separation. We can then start controlling the two particles independently (see Fig. 5.10B).

If this separation is not achieved on the first attempt and the particles move in undesirable directions, the original force field is switched on and the particles are brought back to the stable equilibrium of Fig. 5.10A. A new iteration can start and the process is repeated until the particles are successfully separated. Numerical simulation for this procedure is shown in Fig. 5.10C. The two particles are commanded to swap their positions. Note that we cannot rely on inertia effects since the particles are too small.

The number of particles that can be controlled simultaneously and independently is bounded by the number of electrodes. Relaxing the constraints

---

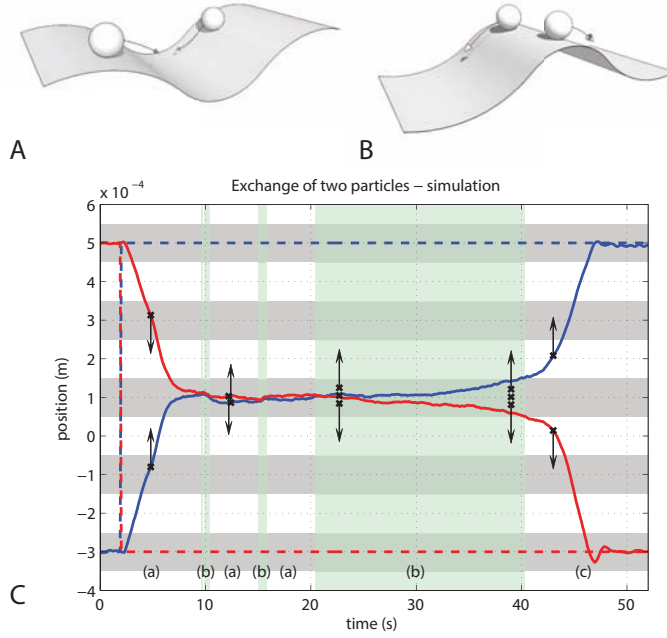[12]Reprinted from [Zemánek et al., 2015].

Figure 5.10.: Principle of noise-aided manipulation. (A) Stable equilibrium attracting particles to the same location. (B) Unstable equilibrium repulsing particles on its two sides. (C) Simulation of the procedure of separation. Particles are commanded to swap their positions. (a) First, they are brought together, (b) and then the procedure of separation begins (indicated by the green color). If separation is not successful, it stops and particles are brought together again. (c) Manipulation finishes when the particles are separated by the predefined distance $(100\,\mu\mathrm{m})$. Arrows represent the desired forces at the locations of the black crosses.[12]

on the amplitudes of the voltages temporarily, the optimization task (5.3) can be reduced to solving a set of equations. Each particle adds two equations (x and z-components of the new demanded force) and each electrode adds one free variable. Therefore, to independently control N particles we need at least $2N$ electrodes. Nevertheless, even if the number of electrodes is

sufficiently high for the given number of particles, it may not be possible to set the forces independently due to bounds on the amplitude of the voltages. Furthermore, as increasing the number of particles increases the size of the corresponding optimization, the computational burden rises as well.

5.4.1. Experiments

Parallel manipulation of three particles, including the position interchange maneuver (swapping), was also successfully demonstrated. From the results presented in Fig. 5.11, it is obvious that the particles oscillated around their final positions with deviations up to 70 μm, much more than in the case of single-particle control. This is because the nonlinear, constrained optimization task is more complex, and the time restrictions allow running only a limited number of iterations. However, based on the experiments we can conclude that independent control of more particles is possible.

This functionality could be used, for example, for noise-based filtering of particles of two different kinds that otherwise experience the same DEP force. Even using a basic parallel electrode array, we could filter particles that behave in the same way. Through controlled introduction of stable and unstable equilibria, we could reach a net velocity of particles of one kind and an opposite net velocity of particles of the other kind.

5.5. Phase modulation

In this final case, we use the four-sector array to demonstrate control of DEP using phase modulation. Amplitude modulation is not used and, for implementation reasons, the phase shifts are chosen merely from a discrete set of 16 fixed values. It is worth emphasizing that the sets of achievable electric fields differ between the cases of amplitude and phase shift control because of the different sets of possible boundary conditions of the electric field. The only fields that can be generated by both approaches (for an array of more than two electrodes) are the trivial cases when all the generating phasors lie in a single line and their magnitudes are equal. Different electric fields also lead to different achievable forces. A comparison is shown in Fig. 5.12, which is a histogram of the achievable forces at the center of the array (at a levitation height of 130 μm) generated by randomly chosen

---

[13]Reprinted from [Zemánek et al., 2015]. Video clip is available at http://youtu.be/nHZIGG4KL-8
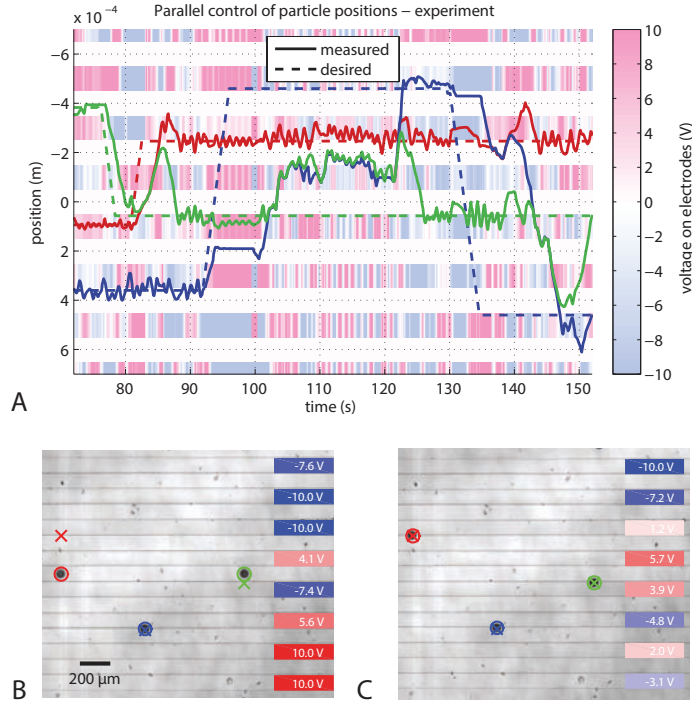
Figure 5.11.: (A) Parallel positioning of three particles using numerical optimization and three independent PID regulators, one for each. (B) Snapshot from the experiment – red has to pass the green particle ($t = 83\,$s). (C) All particles reached the desired positions ($t = 89\,$s).[13]

inputs (with uniform distribution). Phase modulation gives a larger and more uniformly distributed set of achievable forces.

The four-sector array allows several modes of operation, as shown in Section 5.1; using the repulsive effect of the electrodes and the DEP cages, which can be created along the boundaries of adjacent sectors, it is possible to move a particle to an arbitrary position. The feasible trajectories are, limited, however, as sketched in Fig. 5.13. In contrast, the feedback control scheme based on real-time numerical optimization offers a more systematic approach to the positioning task—no explicit selection and parameterization of the "modes" is needed. Furthermore, controlled movement along an arbitrary
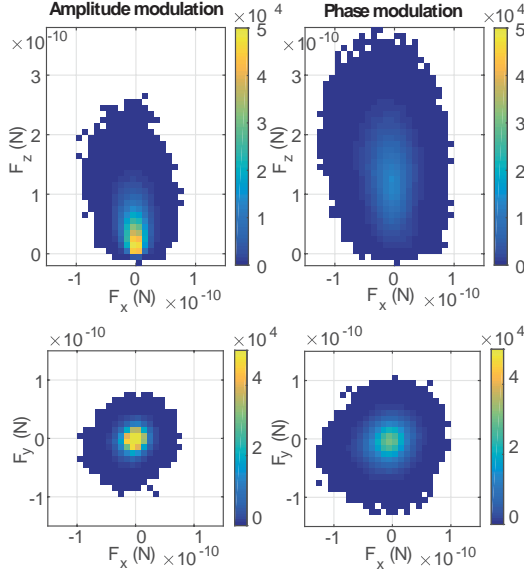
Figure 5.12.: Histograms comparing the forces achievable by amplitude and phase modulation at the center of the four-sector electrode array and a height of $130\,\mu\text{m}$. Constructed from 10^6 samples.

trajectory becomes achievable and the achievable positioning accuracy can be increased significantly, i.e., it is not limited by the dimensions of the electrodes.

5.5.1. Real-time optimization for finding the phase shifts

The mathematical model (4.18) and (4.20) offers a means of determining what forces, $\mathbf{F}_{\text{cDEP}}(\mathbf{r}, \tilde{\mathbf{u}})$ and $\mathbf{F}_{\text{twDEP}}(\mathbf{r}, \tilde{\mathbf{u}})$, are acting on a particle in a given position $\mathbf{r}$ for given input voltages $\tilde{\mathbf{u}} = \begin{bmatrix} \tilde{u}_1 & \tilde{u}_2 & \dots & \tilde{u}_n \end{bmatrix}^{\text{T}}$. The lower layer of the control algorithm should, however, solve the opposite problem; thus, the model has to be inverted, similar to the case of amplitude modulation. This inversion can be accomplished by solving the following optimization problem in every control period
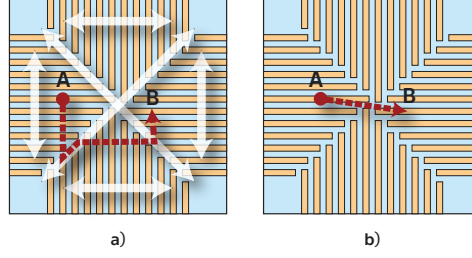
Figure 5.13.: a) Limitations imposed on the achievable motion of the particle when using the simple control strategy based on repulsion and DEP cages. The white arrows indicate the possible basic movements. The red path shows an achievable trajectory for motion from A to B. b) The real-time optimization-based control scheme proposed in the thesis can follow a direct (and even arbitrary) trajectory.

$$\begin{aligned} \underset{\tilde{\mathbf{u}}}{\text{minimize}} \quad & \|\mathbf{F}_{\text{sum}}(\mathbf{r}, \tilde{\mathbf{u}}) - \mathbf{F}_{\text{des}}\|, \\ \text{subject to} \quad & |\tilde{u}_i| = U, \ i = 1, \ldots, n, \\ & \angle \tilde{u}_i \in \left\{0, \frac{\pi}{8}, \ldots, \frac{15}{8}\pi\right\}, \ i = 1, \ldots, n, \end{aligned} \tag{5.4}$$

where $\mathbf{F}_{\text{des}}$ is a vector of the desired force, U is the amplitude of the voltage signals, $|\cdot|$ denotes the phasor magnitude, and $\angle\cdot$ its angle. Some other criteria can be used in the optimization task. For example, one could wish to penalize the error in the direction of the force rather than the error in its magnitude. Or one may even want to maximize the force in a given direction, which translates into the criterion

$$\theta + c\frac{1}{\|\mathbf{F}_{\text{sum}}(\mathbf{r}, \tilde{\mathbf{u}})\|} \tag{5.5}$$

in the otherwise identical optimization problem. Here θ is the angle between the actual force $\mathbf{F}_{\text{sum}}$ and a force vector pointing in the desired direction, and c is a weighting factor enabling setting a trade-off between the two summands in the criterion. The criterion in (5.5) will be used in the following section for an analysis of the movement limitations. However, the position

control algorithm uses the definition in (5.4), which, in contrast, allows generating a zero force.

The optimization task is *non-convex* since the values of phases are discrete. Even if the phase were continuous, the equality constraints would define a non-convex set. The non-convex task prevents us from utilizing any of the well established convex optimization methods. We resorted to heuristic methods and picked a *Simulated annealing algorithm* (SA)[14], which can handle non-convex optimization problems and is suitable for discrete values. Every run of the SA is initialized by the result obtained in the previous control period, which is likely to be near the optimum (unless, for example, an abrupt change in the required force happens).

When dealing with simultaneous independent control of N particles, the task can be extended so that the objective function includes the errors related to all the desired forces: $\sum_{i=1}^{N} \|\mathbf{F}_i - \mathbf{F}_{\text{des},i}\|$. Of course, more complex objective functions demand higher computational time. One possible approach to dealing with a growing number of particles is to decompose the optimization problem into several smaller (hence computationally easier) ones by exploiting the distributed nature of the actuators.

Parallel manipulation

There is another challenge that needs to be faced immediately. The controller needs to know the full (x, y, z) position of the particle in space, but our experimental setup based on a camera overseeing the planar scene through a microscope lens (see Section 3.2.2) can only measure the (x, y) coordinates—the levitation height is left unmeasured. A simple solution is to assume that the initial levitation height is known reasonably accurately and that the controller keeps it constant. If the vertical component of the force vector is set to zero, an equilibrium is created in the particle's position. The initial levitation height can be estimated based on the simulations or roughly measured using a focusing micrometer screw on a microscope. Another solution is to measure all three coordinates (x, y, z) using the twin-beam position estimation method sketched in Section 3.3.2.

5.5.2. Simulations

We can expect that the places where more electrodes meet offer a wider range of possibilities for manipulation. Such places are at the (diagonal) interface between the individual sectors and, unsurprisingly, the very center

---

[14]https://www.mathworks.com/matlabcentral/fileexchange/10548-general-simulated-annealing-algorithm
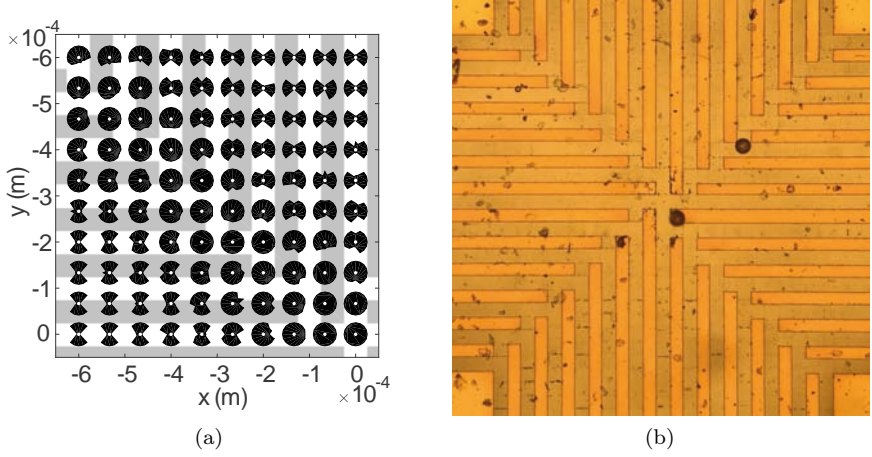
(a)   (b)

Figure 5.14.: (a) Possible directions of motion in a grid of points (white dots) above a quarter of the electrode array. The longer the distance of the black polygon vertices from these grid points, the easier the motion in this direction. (b) The four-sector array viewed by a camera through a microscope.

of the array. The manipulation capabilities of the four-sector array were investigated at first using numerical simulations. The greatest possible force at a given position and for a given direction can be found by solving the optimization problem (5.5). This calculation was done for a grid of points in the manipulation area (covering just one-quarter of the array thanks to the symmetry) and for several directions equally distributed around the 360° range.

The resulting values of the forces define, after suitable uniform scaling, vertices of the polygons in Fig. 5.14. If the polygon resembles a circle, the particle in such a position can move freely in all directions. On the other hand, a bow-tie-shaped polygon indicates that motion in the direction perpendicular to the long axis of the bow tie is hardly achievable. It may be surprising to note that even above the parallel electrodes far from the sector boundaries, movement in the direction along the electrodes is feasible. The influence of the electrodes farther away is non-negligible.

In fact, it is possible to generate motion that corresponds to a force that lies in a convex hull of the polygon. This means it is possible to sum forces

even though the final sum cannot be generated by the optimization task. The trick here is to sum forces through rapid switching between them. This can be viewed as *chattering control*.

5.5.3. Experiments

We verified the manipulation capabilities of our system in a series of experiments. The controller produced square wave signals with an amplitude of 5 V and frequency of 300 kHz. The frequency was in the region of nDEP for a polystyrene microsphere and deionized water. The activation of the control algorithm was always preceded by applying phase shifts of 0 and π alternately to all the electrodes. This pattern causes repulsion of the particles to the known initial levitation height of 140 µm.

First, we demonstrated the capability of tracking a circular reference trajectory. Figure 5.15 shows the measured position of the particle during the experiment together with the data acquired from the numerical simulation of the same situation. The worst-case steady-state error in the reference position tracking is around 20 µm. A visualization of a "virtual potential" related to the same experiment is shown in Fig. 5.16 as a cross-hatched surface. The virtual potential was computed by numerical integration of the force field obtained in the simulation.

Second, manipulation accuracy and precision were evaluated experimentally. A test algorithm repeatedly steered a particle to a grid of points above one quadrant of the manipulation area and recorded the steady-state position error e. Figure 5.17 shows for each position the mean of absolute values of the errors $\mu_{|e|}$ and the standard deviation $\sigma_{|e|}$ of absolute values of the errors. The black lines mark positions of the electrodes. The errors are roughly the same above the whole manipulation area, with the value of 8 µm being the maximum, which is 16 % of the particle's size or 0.7 % of the manipulation range in one direction.

Third, we also tested parallel (simultaneous) manipulation with up to three particles. Figure 5.18 shows an experiment when two microspheres were repeatedly brought together and then separated again. With more particles to manipulate, their movement becomes more oscillatory. The reason for this behavior is probably the increased size of the problem for the real-time optimizer combined with the reduced freedom of shaping the electric field.

---

[15]Video clip available at https://youtu.be/ht6gy5cBGp8

(a)

(b)
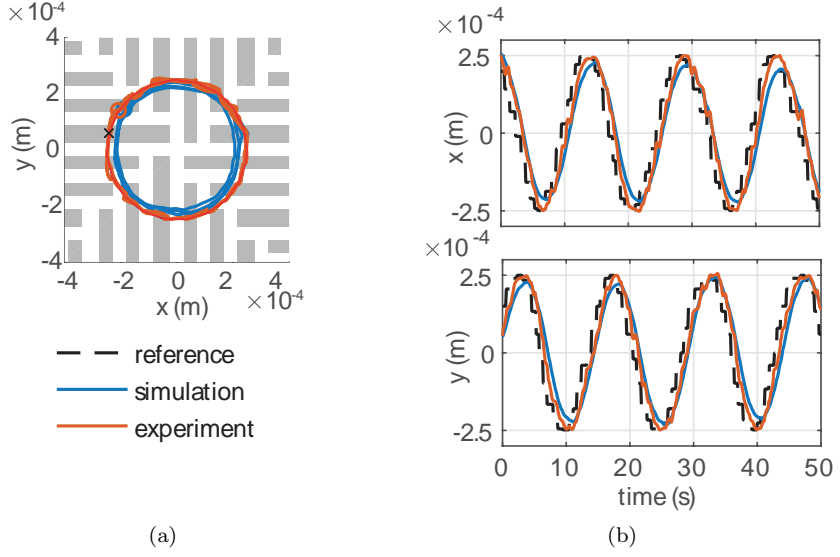
Figure 5.15.: Comparison of the experiment and simulation on the task of circular trajectory tracking. The circle has the diameter 500 μm. (a) The path and (b) the trajectory.
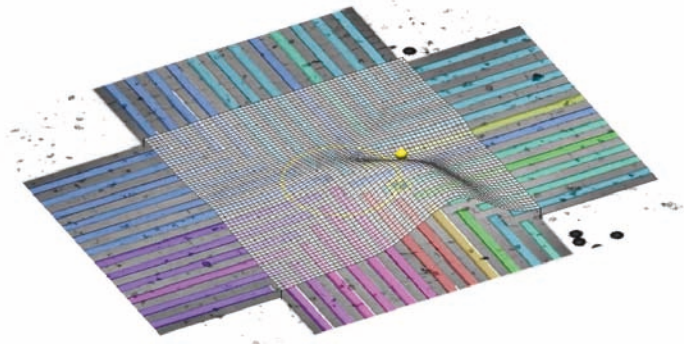

Figure 5.16.: Visualization of a "virtual potential". The image comes from the camera on the microscope. The electrode color represents the phase shift. The circle in the middle of the array shows the reference trajectory.[15]
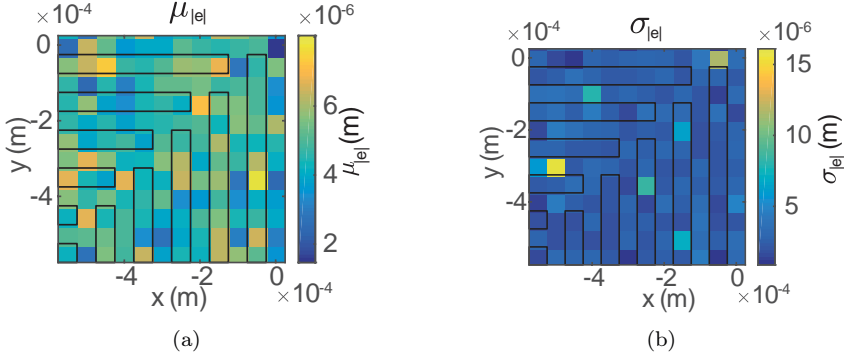
(a)

(b)

Figure 5.17.: Statistical analysis of manipulation accuracy and precision over one quarter of the electrode array based on experimental data. (a) The mean of absolute values of the errors. (b) The standard deviation of absolute values of the errors
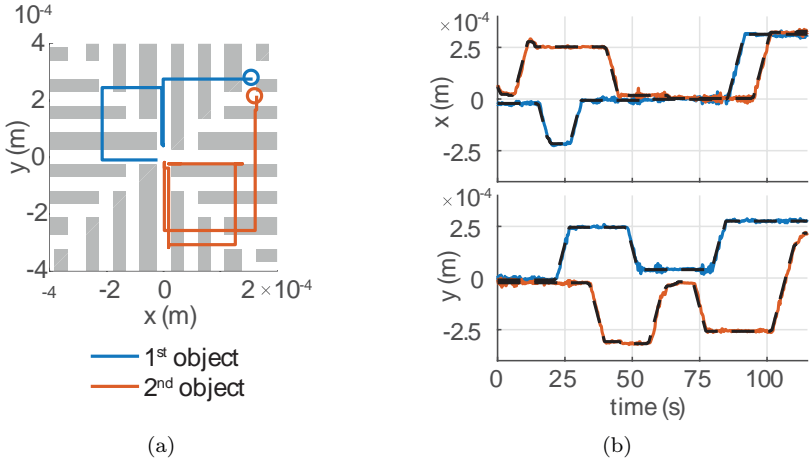

(a)

(b)

Figure 5.18.: Bringing together and subsequently separating two particles. (a) The path and (b) the trajectory.

71

6

Discussion and concluding remarks

In the preceding discussion dedicated to manipulation using an electric field, we first addressed practical aspects of the development of systems for DEP. We designed original layouts of electrode arrays that can serve both for electroosmosis and DEP. The layouts can be easily fabricated and can be used to induce controlled motion in a plane. We also described experimental setups that focused on multi-channel amplitude and phase modulation, and on real-time measurement of the position even in 3D. Mathematical modeling of DEP was presented in order to derive a model suitable for use in a feedback loop. The resulting models relating voltages on electrodes to the force exerted on a particle have a quadratic form. We presented models for both cDEP and twDEP and for variable amplitudes and phases of the applied voltages. Even though the modeling is based on dipole approximation, it proved to be sufficient for feedback control that can handle some level of discrepancy.

We designed several means of manipulation using DEP. One method is based on predefined settings of voltages serving as basic steps from which the desired trajectory is composed. We showed how to plan the trajectory from such basic steps and use them in open-loop and feedback control. We demonstrated a systematic approach that for a given position and a requested force finds voltages for the electrodes that exert this force on the particle. This approach is based on numerical optimization that inverts the mathematical model of DEP. We exploited both amplitude and phase modulation and verified all control systems in experiments. The phase modulation proved as a powerful approach to control DEP. Experiments included parallel manipulation of several particles and even the swapping of particles on the parallel electrode array where it should not be possible. Such swapping allows, for example, filtering of particles with identical properties.

6. Discussion and concluding remarks

We conducted all experiments with polystyrene beads because our main purpose was to present general engineering tools, not the final application. The presented system is not limited to polystyrene beads; it only requires an approximative model of DEP for the particular particle of interest. It also can be scaled up and down. In the future, we would like to perform experiments with particles like cells or droplets of liquid. In addition, we would like to integrate the four-sector array with a twin-beam sensor to have a system capable of controlled 3D manipulation. Our next research also includes experiments with twDEP and a combination of amplitude and phase modulation.

Part II.

Manipulation using a magnetic field

7

Introduction

In this part, we will focus on distributed manipulation using a magnetic field. The main contribution of my work is the design of a laboratory platform serving for development, verification, and demonstration of control systems for distributed magnetic manipulation. Magnetic manipulation is used in many fields from fabrication to biology to medicine. Thus, the first motivation to build our platform was to have a challenging and interesting test bed for such control systems.

7.1. State of the art

Similar to the case of systems for manipulation using an electric field, we classify platforms for magnetic manipulation into two groups according to the arrangement of the coils. The first kind has the manipulation area enclosed by the coils; therefore the motion is constrained to the space between coils. The second kind allows motion of the object across several coils. Such an arrangement of the coils can have the form of a planar array. It means that the manipulation area is virtually unlimited (in two dimensions) because the array can be extended to a larger area by adding more coils.

Several platforms described in the literature use a magnetic field for manipulation or micromanipulation. For example, [Pelrine, 1989] introduces a concept of manipulation using magnetically levitated magnets that evolved over time to controlled diamagnetic levitation [Hsu et al., 2016]. [Khamesee et al., 2002] use eight coils for controlled magnetic levitation. A magnetically levitated robot for 3D manipulation is also shown in [Elbuken et al., 2009]. Often Helmholtz and/or Maxwell coils are used. For example, [Floyd et al., 2009, Pawashe et al., 2012] describe *Mag-μBot*—a permanent magnet actuated by six air coils placed on the faces of a cube. [Probst et al., 2011] demonstrate steering of a ferrofluid drop by control of four electromagnets. [Kummer et al., 2010] describe a system called *OctoMag* allowing 5-DOF

Microrobotics

control of an untethered microrobot designed for delicate retinal procedures. This system has a smaller version called *MiniMag* [Kratochvil et al., 2014]. [Dkhil et al., 2014, Dkhil et al., 2017] present control of a magnetic particle at the air-liquid interface using four coils. [Pieters et al., 2016] use eight coils and model predictive control to guide a rolling microrobot. Magnetic manipulation can be used for actuation of medical robots by clinical MRI scanners [Martel, 2017]. Even though it is possible to control multiple objects in a global magnetic field to some extent[Diller et al., 2012, Diller et al., 2013, Rahmer et al., 2017], we concentrate on platforms that use local magnetic fields—that is, systems with an array of coils.

Human-machine interface

In the HMI (*Human-machine interface*) field, we find a few platforms utilizing an array of coils. The system called *Actuated Workbench* uses a grid of electromagnets to move a magnetic puck [Pangaro et al., 2002] for tangible interfaces. A system nicknamed *Madgets* (magnetic widgets) contains miscellaneous components (knobs, buttons, etc.) for control panels [Weiss et al., 2010] that can be rearranged by a computer, and individual components can provide various haptic feedback [Weiss et al., 2011a]. This system can also be used to generate near-surface haptic feedback on interactive tabletops [Weiss et al., 2011b]. A system with an array of 10×10 electromagnets can animate strings of magnets [Kono and Kakehi, 2012].

Microsystems

In microsystems, coils are usually planar and have either a meander or a spiral shape, which is either circular (a so-called pancake coil) or rectangular. An array of planar coils moves a permanent magnet or an array of magnets [Nakazawa et al., 1997, Komori and Hirakawa, 2005, Cappelleri et al., 2014, Chowdhury et al., 2015]. Even coils in the simplest form, i.e. single loops, can form a distributed manipulator [Chowdhury et al., 2017]. [Lee et al., 2004] present a microelectromagnet matrix formed by parallel wires in two layers perpendicular to each other. [Lee et al., 2006] show an integrated circuit for magnetic manipulation of cells. The array has 8×8 microcoils and the cells have to be attached to magnetic beads. [Issadore et al., 2009] combine an electric field created by an array of 60×61 DEP pixels with a magnetic field created by parallel wires arranged in a grid.

Meander-shaped coils work similarly to a linear motor. Two planar, meander-shaped coils shifted in respect to each other to move an array of permanent magnets [Khan et al., 2012]. [Dang et al., 2016] extend this concept to a matrix of such linear motors allowing parallel manipulation. Besides permanent magnets, the meander-shaped coils can manipulate microrobots through diamagnetic levitation [Pelrine et al., 2012].

7.2. Contribution

The main contribution of this work is the design of a platform that can be used as a test bed for control systems for distributed magnetic manipulation. The investigated control system could be either centralized or distributed because the platform is modular and each module has its own processor. Thanks to the modularity, the platform can be easily reconfigured to another shape or made bigger.

Even though platforms with a similar arrangement of coils exist, our system is distinguishable because the manipulated objects are not permanent magnets. This changes the structure of the problem because the magnetization of the object is not a constant but depends on the magnetic field—the control problem is not linear but quadratic.

The platform described in this thesis was awarded "first place" in the 2013 MATLAB and Simulink Student Design Challenge[1]. It was shortlisted in the top seven video clips in the IEEE CSS Video Clip Contest 2014[2], and received the EEA Demonstrator Paper Prize on IFAC World Congress 2017[3]. Another team has already used a one-dimensional version of our platform to benchmark nonlinear controllers [Damsteeg et al., 2017].

7.3. Related work

During my dissertation research, I supervised several students who greatly helped me with my work. The relevant work is captured in their bachelor's and master's theses. [Richter, 2014, Richter, 2017] solved mainly hardware and firmware issues of the platform, made an upgrade of the electronics, and extended the platform. [Simonian, 2014] tried several controllers based on reinforcement learning. Section 10.5 about switching control comes from our paper [Zemánek et al., 2017].

7.4. Organization of the part

The remaining chapters of this part are organized as follows. In the next chapter, we will describe hardware of the platform and available methods for measuring the position of the manipulated object. We will then build

---

[1] http://www.mathworks.com/academia/student-challenge/spring-2013.html
[2] http://www.ieeecss.org/video-contest/2014/winners
[3] https://www.ifac2017.org/prizes#DPP

a mathematical model suitable for feedback control. The derivation of the model starts with a magnetic field of a single coil, then examines a force exerted by several coils, and ends with dynamics of the ball. The penultimate chapter in this part is devoted to our proposed ways to control magnetic manipulation. We will show optimization-based feedback linearization and then use it for position control of one and several objects. Besides, we will demonstrate examples of control systems for maintaining oscillations and switching time-optimal control. We will conclude this part with a chapter summarizing our findings and future research plans.

8

Hardware description

The platform contains a set of electromagnetic coils arranged in a rectangular array, above which a flat surface is placed, as seen in Figs. 8.2 and 8.3. Coils actuate one or several steel balls rolling on the surface. We nicknamed the platform Magman (magnetic manipulation).

8.1. Module

The basic building block of the Magman platform is a rectangular, solid-shaped module. The module's base is a square with dimensions of 50×50 mm. Its height is 75 mm. The module consists of three main parts—four coils, an iron base from which four cores are erected, and driving electronic circuitry—as shown in Fig. 8.1. An electric current flowing through a coil creates a magnetic field, and the magnetic field intensity is increased by the presence of the iron core and the base. The iron base also reduces magnetic flux passing through the electronics and thus suppresses possible interference. To be able to modulate the magnetic field's intensity, the electronics control the direction and value of the current. The module is designed in a truly modular way; that is, it is prepared both mechanically and electrically to be used as a building block to create larger arrays of modules. Therefore, the board has identical electrical connectors (power and communication lines) on each of its four sides.

Relevant parameters of the coil are specified in Table 8.1. The inductance of the coil is not stated there because it is difficult to measure it correctly due to losses in the core. Relative permittivity will be discussed later in the section on mathematical modeling.

The computational heart of the control board is the 32-bit microcontroller Electronics
ARM Cortex-M3 (LPC1311) running at 72 MHz. The microcontroller is interfaced to four full H-bridges (DRV8800) for switching the currents through individual coils and changing their directions. Moreover, each coil
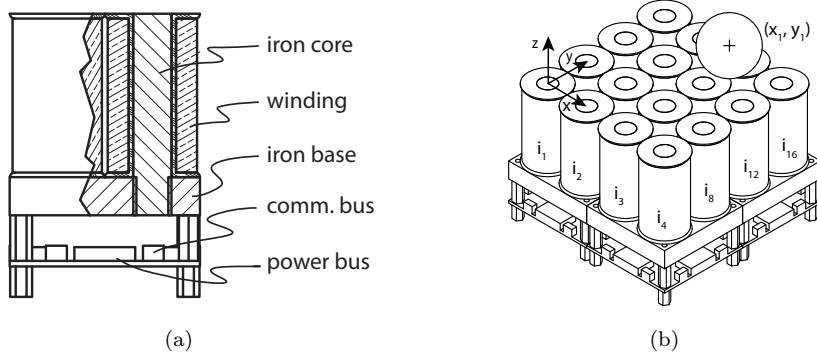
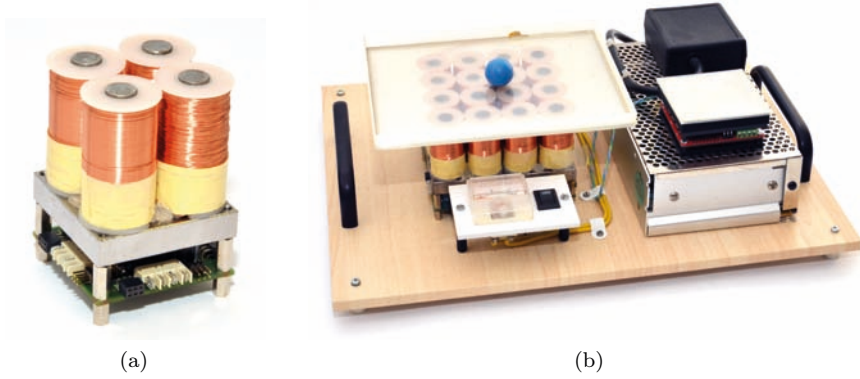Figure 8.1.: (a) The module of the platform. (b) Platform with key symbols.

Figure 8.2.: (a) The module that is used as a basic building block of a larger, reconfigurable (electro)magnetic array. (b) The experimental platform consisting of a 4×4 array of coils created by stacking together 2×2 basic modules, a power supply, a glass equipped with a transparent resistive foil for position measurement, and a border.

has a shunt resistor $(0.02\,\Omega)$ and a current-shunt monitor (INA210, gain 200) that enables measurement of the current as needed for implementation

Figure 8.3.: Extended platform for magnetic manipulation consisting of an
8×8 array of coils.

Table 8.1.: Parameters of the coil

Voltage	24 V
Max. current	420 mA
Resistance	58 Ω
Time constant	9.6 ms
Inductance (without core)	50 mH
Rel. permittivity	30-300
No. of turns	3000

of a current feedback loop. Control of the current is important because the
coil can get hot, which changes the resistivity. The board can communicate
with its environment via an RS-485 bus running at speed 230400 Bd. The
platform can be controlled from a PC over a USB to RS-485 adapter. For
that case, the refresh rates are given in Table 8.2. The firmware includes a

Table 8.2.: Parameters of communication

Speed	230400 Bd
Refresh rate 1 coil	2.3 kHz
Refresh rate 1 module	1.3 kHz
Refresh rate whole platform	320 Hz

bootloader that enables loading of new firmware through the communication bus. Finally, the board is prepared for further expansion by other boards stacked on the bottom of it and interconnected via an I2C bus. This way, the functionality of the module can be enhanced by, for instance, processing the measurements from a temperature sensor, magnetometer, optical sensor, etc.

8.2. Position measurement

8.2.1. Overview of suitable sensors

Sufficiently fast and accurate measurement of the position of the ball is required for feedback control. Because the manipulation takes place in a plane, several technological inspirations can be taken from the field of touchscreens. A concise review of methods used in touch screens is found in [Walker, 2012]. However, there are a couple of significant constraints in our proposed platform compared to touchscreens. First, it may be desirable to measure the positions of several objects at once. Second, the object to be manipulated will be an iron ball.

Touch screens on hand-held devices are often either resistive (especially cheaper and older devices) or capacitive. The *resistive touch sensor* is, in its basic form, two resistive foils separated by microdots capable of measuring the position of a single touch. Nevertheless, it is possible to find multi-touch sensors that are made through arranging perpendicular stripes of foils into the form of a matrix.

Capacitive touchscreens contain parallel electrodes in two layers (perpendicular to each other) intersecting in a matrix where capacitance can be analyzed. The presence of an object in proximity to the sensor's surface results in a change of capacity that can be detected to determine the object's position. Multi-touch sensing by such a sensor is, in principle, possible.

A disadvantage of the capacitive sensor for our purpose, however, is that commercially available devices are ready to detect human fingertips, not steel balls. Furthermore, detection of the steel ball would not be easy because of the presence of the iron cores in the vicinity of the sensor.

Another class of sensors utilizable for position measurement is *tactile sensors* (matrix pressure sensors) capable of measuring pressure (compression) at several points in a matrix. Measurement is usually done through analyzing the change in resistance or capacity of a deformable surface (for example, a conductive foam).

It is also possible to exploit light or IR to sense the ball's position. An *IR- based sensor* consists of a line of IR emitters and detectors, arranged along the frame, that can detect one or several objects blocking IR emission. The photodetectors can also be arranged to form a matrix.

A classical approach in the robotics community is the use of a *fast camera* and a computer that processes the digital image to find the position of the ball. A camera (or a *linear camera*) could be mounted on the side of the array. A significant disadvantage is a non-negligible latency. Moreover, this sensing method leads, in principle, only to centralized manipulation schemes. A single camera is monitoring the whole array. The above-mentioned techniques could be used to make each module completely self-contained, detecting the presence and sensing the position of the ball on the "roof" of each module.

An interesting alternative to a standard (intensity) camera is a *depth camera* giving information about the depth of individual pixels. The depth is calculated from time-of-flight (ToF) or using structured light. Processing of such an image can be in some sense easier because objects can be well distinguished by their depth. Furthermore, the depth camera is insensitive to changes in lighting. On the other hand, depth cameras have lower resolution and work well for higher working distance. These are drawbacks in our application where both the scene and the object are small.

The last method that can be exploited is an *analysis of impedance*, i.e. measuring mutual inductance and self-inductance of the coils. The presence of the ball influences both mutual and self-inductance, but it has to be considered whether this change is big enough to be detected. Similarly, the presence of the ball reshapes the magnetic field. Thus the position can be theoretically estimated using an *analysis of the magnetic field*.

8.2.2. Resistive touch sensor

Resistive touch sensors are widely used in some handheld devices [Downs, 2005]. We used a so-called four-wires sensor. The sensor consists of two flexible resistive sheets separated by an air gap and (micro-)dot separators. An interconnection between these two conducting layers can be created at a point where the object (ball) touches and, in fact, loads the upper sheet of the sensor. The planar position is measured in two steps. In the first step, the voltage applied to the electrodes on the opposite sides of one layer creates a voltage drop across one direction, say the x-axis. Therefore, if the object interconnects the two layers, the voltage on the other layer corresponds to the position along the x-axis. In the second step, the voltage applied to the electrodes on the second layer creates a voltage drop in the orthogonal direction, that is, the direction of the y-axis and now the voltage on the first layer corresponds to the position along the y-axis.

This sensor is advantageous because of its low price, good spatial resolution, and a high sampling rate (both limited mostly by the AD converter). Nonetheless, it also has two main drawbacks. First, it is not capable of measuring the planar position of multiple objects at once (in the simple version). Second, the contact resistance between the layers depends on the pressure exerted by the object (ball).

To a certain extent this dependence can be used to estimate the touching force, but if the touching force is too small, it is not possible to measure the position correctly. As a consequence, the measurement by the sensor may be inaccurate if the pressure exerted on the surface is lowered temporarily. This is the reason to use a bigger ball. In our case, the sampling frequency of measurement can be up to 1 kHz. The standard deviation of the position is 0.7 mm. The noise in the position comes mainly from other electronics and it can be notably suppressed using a shielding under the foil.

8.2.3. Computer vision

To overcome the problem with noise and to have the possibility to detect several balls, we implemented and tested several computer vision algorithms. A camera (Basler acA2000-340kc, 2046×1086 px, 340 fps, lens 12 mm F/1.8) captures the image and a frame grabber (BitFlow Neon-CLB) transmits it to the computer.

A few properties of the scene actually make the application of computer vision easier. For example, the scene is almost static (except the moving ball), the camera is in a fixed position approximately 50 cm above the

surface, and the illumination is static. Therefore the visual appearance of the ball always remains the same. The ball is well distinguishable from the background because it is colored while the background does not contain any distinctive colors. Therefore the implemented algorithm took advantage of color distinctness of the ball.

First, we tested a standard *Meanshift algorithm*, which is a simplified version of *Camshift* (Continuously Adaptive Mean Shift). The algorithm finds the region of the image whose histogram best fits the reference histogram. It turned out that the Meanshift algorithm is in our case outperformed by simpler algorithms that give faster and more precise detection. Namely, we then tested a linear *support vector machine* (SVM) and simple thresholding in hue-saturation-visibility (HSV or HSB) space and found their performance to be superior.

SVM based on the training dataset finds a vector of weights and a bias that are afterward used to classify individual pixels (represented by a feature vector—RGB values in our case) as a foreground or a background. In addition, we tested detection utilizing HSV. The selection of this method was motivated by the fact that the ball should be well distinguishable from the background by the value of saturation. A part of the acquired image—the region of interest (ROI)—was converted to HSV and then thresholds for saturation, visibility, and hue were applied. Conversion of the image from the RGB space into the HSV space takes some computational time, so we formulated thresholding of HSV values in RGB space. The center of the ball is then found in such a way that individual pixels are marked by 0 for the background and 1 for the foreground, then the sums of rows and the sums of columns are calculated. The position is detected by maximal correlation of the sums with the shape of the ball.

Computer vision was implemented in Matlab/Simulink, which introduces some performance limits. Acquisition of the image from the camera via Image Acquisition Toolbox takes approx. 13 ms. Detection of the ball using linear SVM takes approximately 5.5 ms and using thresholding of HSV values it takes 4.6 ms when it is done in RGB space (18 ms when it is done in HSV). Therefore, maximum sampling frequency is approx 50 Hz. The median of the error for the SVM is 1–3 px (according to the color of the ball), which corresponds to 0.2 mm–0.6 mm, and for thresholding the median of the error is 1.6 px, which corresponds to 0.3 mm.

It is difficult to implement a computer vision system that is fast and at the same time easily adjustable. We wanted to keep the system open for further adjustments and improvements so we decided to use a higher level of abstraction, which brings about some delay in processing.

Later we modified the control system to run on the Raspberry Pi 3. That is, the control system can be designed in Simulink and then translated to a C code that can run on the Raspberry. Because the performance of the computer vision algorithm written in Simulink was poor, the algorithm is written in Python using Open CV library and sends positions of detected objects to the control system using shared memory. The computer vision algorithm uses a standard Raspberry Camera[1] to capture the image. The sampling frequency remains equal to 50 Hz. We used this system in another project [Gurtner and Zemánek, 2017].

8.2.4. Analysis of magnetic field

We tried to measure the position of the ball based on changes in the magnetic field. Those methods involve analyzing the self-inductance, the mutual inductance, and the magnetic flux density. Presence of the steel ball in the vicinity of the coil should change the inductance of the coil. Nevertheless, measurements did not show any significant change. Similarly, the ball should change the mutual-inductance between two coils. The mutual inductance for two neighboring coils is approximately 79 mH. Turning on one coil induces current 37 mA in the other coil. The ball changes this induced current by only 3 mA, which can hardly be processed. We also tried to put a sensor in between the coils to measure change in the magnetic field. The magnitude of the magnetic flux density for the activated coil (250 mA) was approximately 75 mT and the change caused by the ball was approximately 6 mT when the ball was right above the sensor. Results can be seen in Fig. 8.4.

---

[1]There is a significant difference between Raspberry Camera versions 1 and 2. When running in smaller resolution, version 1 downsamples (decimates) the image because it only takes every other pixel. Version 2, on the other hand, crops the image, which leads to a smaller field of view.
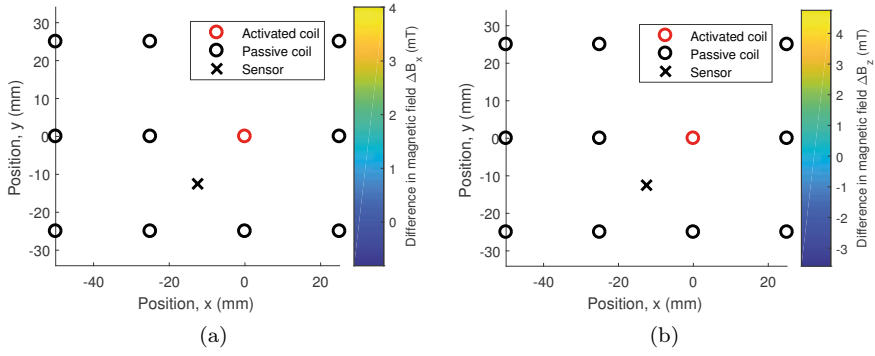
Figure 8.4.: Change in the magnetic flux density caused by the presence of the ball. (a) x-component, (b) z-component.

9

Mathematical modeling

The mathematical model serves two purposes. For system design, we need the model to calculate the motion of the object for known currents flowing through the coils. In the feedback loop, the model serves for finding suitable currents to exert desired force. The currents may vary over time, but we will consider only slow changes; therefore the magnetic field is *quasi-static*. The magnetic force acting on the object arises from an interaction of the object with the magnetic field. To evaluate this interaction, we can first calculate the magnetic field without the object and then the induced field within the object. Alternatively, we can calculate the field with the object present in it. We will discuss the magnetic field of a single coil, the magnetic field of multiple coils, magnetic force, and dynamics of the ball.

9.1. Single coil

The magnetic field can be obtained from Ampère's law

$$\nabla \times \mathbf{H} = \frac{\partial \mathbf{D}}{\partial t} + \mathbf{J}, \tag{9.1}$$

where $\mathbf{H}$ is the *magnetic field strength*, $\mathbf{D}$ the *electric displacement field*, and $\mathbf{J}$ the *total current density*. In our case, the electric displacement does not change over time. Therefore the law is in the form

$$\nabla \times \mathbf{B} = \mu \mathbf{J}, \tag{9.2}$$

where $\mathbf{B}$ is the *magnetic flux density* and μ the permeability[1]. It is beneficial to separate the magnetic field of a coil into two parts—one depends solely on the position and the other only on the current

---

[1] [2] for $\mathbf{H}$, and *magnetic field* for both $\mathbf{H}$ and $\mathbf{B}$.

$$\mathbf{B}_{\mathrm{coil}}(i, \mathbf{r}) = f(i)\mathbf{B}_{\mathrm{ref}}(\mathbf{r}), \qquad (9.3)$$

where function $f(i)$ captures how the magnetic field scales with the current i flowing through the coil[3], and $\mathbf{B}_{\mathrm{ref}}(\mathbf{r})$ represents how the magnetic field evolves with the position $\mathbf{r}$ for the reference current i_{ref}. Separation is justified by Ampère's law, where the right-hand side in (9.2) can be written as $\mu|f(i)|\mathbf{J}(\mathbf{r})$. Because the equation is linear, we can isolate the part of the solution that depends on the position from the part that scales it and depends on the current.

Hysteresis · · · · · The evolution of the magnetic flux density with the current depends on the material. The magnetic field strength $\mathbf{H}$ is proportional to the current. Because the core is from iron, i.e. ferromagnetic material, it experiences *magnetic hysteresis*. The hysteresis can be visualized by the *B-H curve* (magnetization curve, magnetic hysteresis curve) in Fig. 9.1a. This curve was measured on a closed sample (no air gap) of toroidal shape. On the platform, the magnetic circuit is open and we are interested in the magnetic field in air. Therefore we measured the magnetic flux density for several values of the current with a magnetometer (gaussmeter) at the coil's end in the core's axis. Figure 9.1b shows the measured data together with a function that we used to fit the data.

$$f(i) = 0.889\arctan\left(2.51|i| + 5.38i^2\right)\operatorname{sgn}(i), \ |i| \le i_{\mathrm{max}}. \qquad (9.4)$$

We picked the arctan function because its shape fits the measured data well. It is noticeable in Fig. 9.1b that the core in an open circuit behaves as magnetically soft, which means that the coercive force is small. For a given value of current, the magnetic flux density varies in the range of $8\,\mathrm{mT}$ at maximum, which corresponds to the value of residual magnetism. For a current above $100\,\mathrm{mA}$, the relative change of the flux density caused by hysteresis is under $30\,\%$.

As for the relation between the magnetic field and the position, it can be found analytically or numerically. Let us focus first on analytical solutions. We do not need to know the field in the whole space because the balls move only above the coils. Formally, it is a half-space without any free currents.

The magnetic flux density of a single coil was measured to verify the models and calibrate the unknown parameters. Data were collected using a magnetometer and a 3-axis micromanipulation stage that moved the probe to the predefined points. The result of the measurement is shown in Fig. 9.2

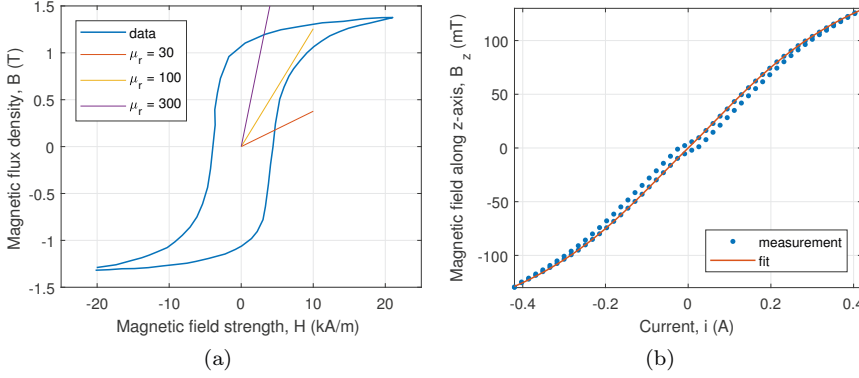[3]$f(i_{\mathrm{ref}}) = 1$ for the reference current i_{ref}

Figure 9.1.: (a) B-H curve for iron measured on a closed sample of toroidal shape. (b) Magnetic field at the end of the core measured by a gaussmeter.

that depicts a section above the activated coil. It is important to note that the measurement was done in the presence of other coils. Even though the magnetic field of one solenoid is axially symmetric, it does not hold in our case because of the presence of other coils. Nevertheless, we will consider the field to be axially symmetric and show later that this is a justifiable approximation.

9.1.1. Monopole and dipole

First, we can try to approximate the coil as an infinitesimally thin and infinitely long magnet. This means that the magnetic field corresponds to the magnetic field created by a *magnetic monopole*

$$\mathbf{B}_{\mathrm{MP}}(\mathbf{r}) = -\frac{q_{\mathrm{m}}}{4\pi}\nabla\frac{1}{|\mathbf{r}|} = \underbrace{-\frac{q_{\mathrm{m}}}{4\pi}}_{a}\frac{\mathbf{r}}{|\mathbf{r}|^3}, \tag{9.5}$$

where q_{m} denotes the strength of the point magnetic monopole located at the origin. To find this parameter, we can fit the measured magnetic field by the function

$$|\mathbf{B}_{\mathrm{MP}}(\mathbf{r}, i)| = \frac{f(i) \cdot a}{x^2 + y^2 + (z+b)^2} = \frac{0.73 \cdot 5.55 \cdot 10^{-6}}{x^2 + y^2 + (z + 4.3 \cdot 10^{-3})^2}, \tag{9.6}$$
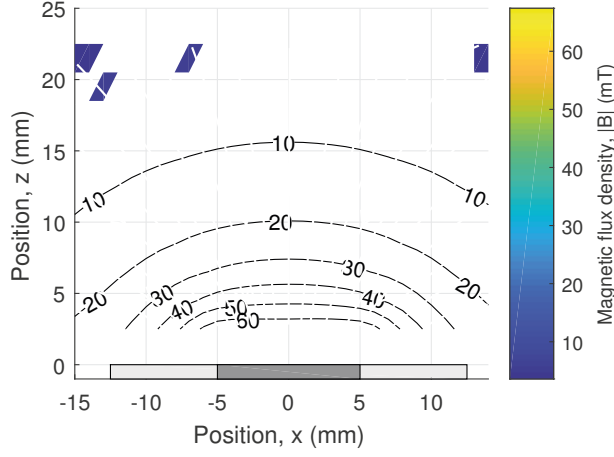
Figure 9.2.: Magnetic field in a section above the activated coil ($i = 250\,\text{mA}$) measured by a gaussmeter.

where the parameter b added to the denominator enhances the fit because it allows shift of the monopole in the z-direction. The numerical parameters were obtained for fitting at the height of $15\,\text{mm}$, which corresponds the center of 30-mm ball. In Fig. 9.3a, we can see that the magnetic monopole approximates the field well at the fixed height.

Dipole   We can also try to approximate the magnetic field of the solenoid by the field created by a *magnetic dipole*

$$\mathbf{B}_{\text{DP}}(\mathbf{r}) = \underbrace{-\frac{q_m}{4\pi}}_{a} \nabla \left(\frac{1}{|\mathbf{r} - \mathbf{r_1}|} - \frac{1}{|\mathbf{r} - \mathbf{r_2}|} \right), \qquad (9.7)$$

where $\mathbf{r}_1$ and $\mathbf{r}_2$ stand for the positions of two magnetic charges. The charges are in our case placed on the axis of the coil so that $\mathbf{r}_1 = (0, 0, z_1), \mathbf{r}_2 = (0, 0, z_2)$. Values obtained by curve fitting are the following: $a = 3.565 \cdot 10^{-5}, z_1 = -11.8 \cdot 10^{-3}, z_2 = -15.3 \cdot 10^{-3}$. In comparison to the monopole field, the dipole field captures the evolution in height better, as can be seen in Fig. 9.3b,

9.1.2. Axial model

This model is based on the general solution of the Laplace equation in spherical coordinates for the special case of axial symmetry (azimuthal
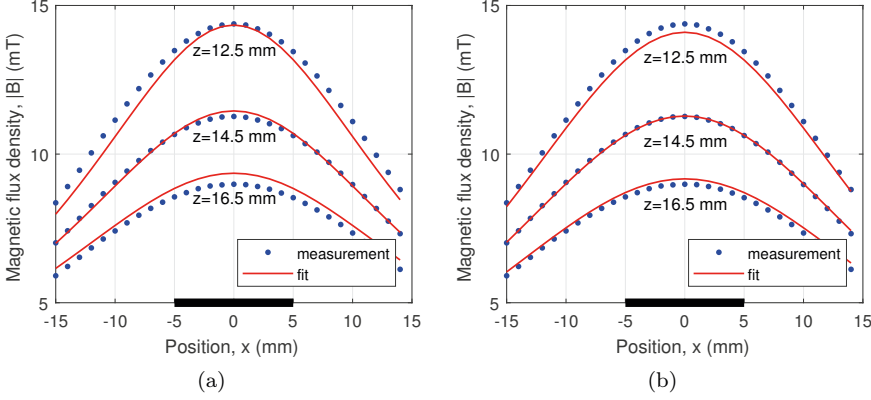
Figure 9.3.: Magnitude of the field at various heights compared with the (a) monopole model and (b) dipole model.

symmetry). The *magnetic scalar potential*[4] defined as $\mathbf{B} = -\nabla U$ can be expressed [Griffiths, 2017, Jackson, 1998] as

$$U(r, \theta) = \sum_{n=0}^{\infty} \left(A_n r^n + \frac{B_n}{r^{n+1}} \right) P_n(\cos(\theta)), \qquad (9.8)$$

where $P_n(\cdot)$ are Legendre polynomials. Because the field decreases with the distance in our case, coefficients A_n have to be zero. The first few terms of the series are

$$U(r, \theta) = \frac{B_0}{r} + \frac{B_1 \cos(\theta)}{r^2} + \frac{B_2 \left(3 \cos^2(\theta) - 1 \right)}{2r^3} + \\ + \frac{B_3 \left(5 \cos^3(\theta) - 3 \cos(\theta) \right)}{2r^4} + \cdots. \qquad (9.9)$$

We see that the first term is the magnetic scalar potential of a monopole and the second term is the potential of a dipole. Since we are working in spherical coordinates, it is easier to express the gradient in spherical coordinates[5]

---

[4]We can express the magnetic field through the magnetic scalar potential because of the absence of currents in the halfspace above the coils.

[5]Thanks to axial symmetry, there is no influence of the azimuthal angle ϕ.

$$\nabla U = \frac{\partial U}{\partial r}\hat{\mathbf{r}} + \frac{1}{r}\frac{\partial U}{\partial \theta}\hat{\boldsymbol{\theta}}. \tag{9.10}$$

and then transform it to Cartesian coordinates. This can be done by expressing the basis vectors of the spherical coordinate system in the Cartesian coordinate system

$$\mathbf{R}_z(\phi)\mathbf{R}_y(\theta) = \begin{bmatrix} \cos(\phi)\cos(\theta) & -\sin(\phi) & \cos(\phi)\sin(\theta) \\ \sin(\phi)\cos(\theta) & \cos(\phi) & \sin(\phi)\sin(\theta) \\ -\sin(\theta) & 0 & \cos(\theta) \end{bmatrix} = $$
$$= \begin{bmatrix} \hat{\boldsymbol{\theta}} & \hat{\boldsymbol{\phi}} & \hat{\mathbf{r}} \end{bmatrix}, \tag{9.11}$$

and substituting for

$$r = \sqrt{x^2 + y^2 + z^2}, \quad \theta = \arccos\left(\frac{z}{r}\right), \quad \phi = \arctan\left(\frac{y}{x}\right). \tag{9.12}$$

Partial derivatives of the potential that appear in the gradient (9.10) are

$$\frac{\partial U}{\partial r} = -\frac{B_0}{r^2} - \frac{2B_1\cos(\theta)}{r^3} - \frac{3B_2\left(3\cos^2(\theta) - 1\right)}{2r^4} - $$
$$- \frac{2B_3\left(5\cos^3(\theta) - 3\cos(\theta)\right)}{r^5} + \cdots, \tag{9.13}$$

$$\frac{\partial U}{\partial \theta} = -\frac{B_1\sin(\theta)}{r^2} - \frac{3B_2\cos(\theta)\sin(\theta)}{r^3} + $$
$$+ \frac{B_3\left(-15\cos^2(\theta)\sin(\theta) + 3\sin(\theta)\right)}{2r^4} + \cdots. \tag{9.14}$$

The coefficients B_n were found by fitting (9.13) to the measurement of the magnetic field along the axis of the coil. One additional parameter Δz was the shift of the coordinate system along the z-axis. The values for various orders of the series are stated in Table 9.1.

From the comparison of the mathematical model and the measured data in Fig. 9.4 it is apparent that the model fits the data quite well. The relative error is within $20\,\%$ up to $13\,\text{mm}$ for B_0, to $22\,\text{mm}$ for B_1, and to $26\,\text{mm}$ for B_2 and B_3.

The evolutions of the magnetic field with the distance from the axis were investigated. Comparison of the measured data with the axial mathematical

Table 9.1.: Parameters of the axial model found using fitting.

Δz	B_0	B_1	B_2	B_3
$8.77 \cdot 10^{-3}$	$1.07 \cdot 10^{-5}$	0	0	0
$4.22 \cdot 10^{-3}$	$7.21 \cdot 10^{-6}$	$-1.05 \cdot 10^{-8}$	0	0
$2.72 \cdot 10^{-3}$	$6.36 \cdot 10^{-6}$	$-1.3 \cdot 10^{-8}$	$1.02 \cdot 10^{-11}$	0
$2.54 \cdot 10^{-3}$	$6.35 \cdot 10^{-6}$	$-1.4 \cdot 10^{-8}$	$1.44 \cdot 10^{-11}$	$-4.81 \cdot 10^{-15}$
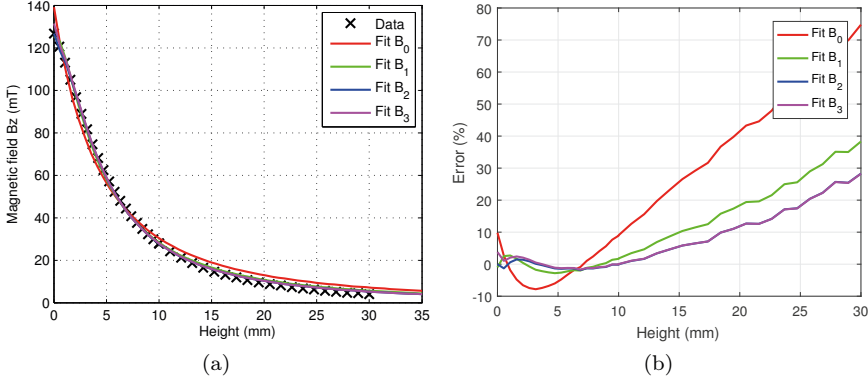
Figure 9.4.: Comparison of the mathematical model and the measured z-component of the magnetic field along the axis of the coil.

model is in Fig. 9.5. It is notable that the axial model is not able to capture the shape of the magnetic field right above the coil. Higher above the coil (5 mm) the axial model fits the data well except for the model with only B_0 nonzero.

9.1.3. Green's function

Calculation of the magnetic field in the half-space above the coil can be viewed as a boundary value problem if the magnetic field on the boundary is known. Formally written, we want to find the scalar potential of the magnetic field U ($\mathbf{B} = -\nabla U$) that satisfies the Laplace equation

$$\nabla^2 U = 0 \quad (z > 0), \tag{9.15}$$
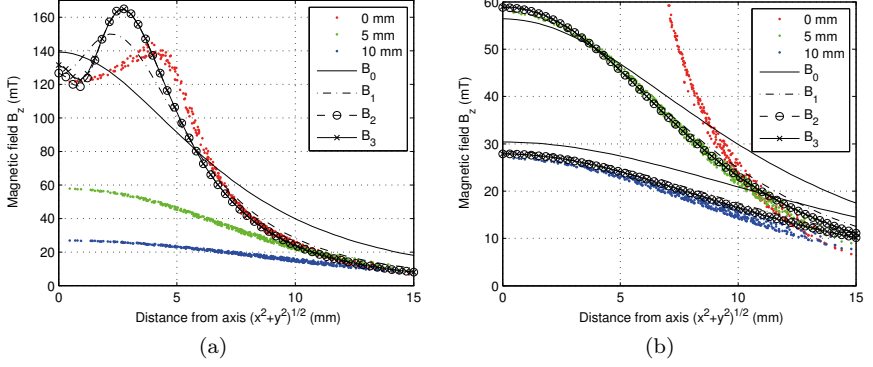
and the boundary condition

97

Figure 9.5.: Comparison of the axial mathematical model (of various order) and the measured data.

$$- \mathbf{n} \cdot \nabla U = B_n \quad (z = 0), \tag{9.16}$$

where $\mathbf{n}$ is the unit vector in the z-direction and $B_n(x, y) = B_z(x, y, z = 0)$ is the normal field component on the boundary. In such a case, the scalar magnetic potential can be obtained using the Green's function for a Neumann problem

$$U(\mathbf{r}) = \int B_n(\mathbf{r}')G_n(\mathbf{r}, \mathbf{r}') \, \mathrm{d}S', \tag{9.17}$$

where $\mathrm{d}S' = \mathrm{d}x' \, \mathrm{d}y'$, $\mathbf{r}' = (x', y', 0)$. Green's function

$$G_n(\mathbf{r}, \mathbf{r}') = \frac{1}{2\pi|\mathbf{r} - \mathbf{r}'|} \tag{9.18}$$

represents the potential of a monopole located at $\mathbf{r}$. Because we assume the solution to be rotationally symmetric about the z-axis, it is natural to use the cylindrical coordinate system $\mathbf{r} = (\rho, \varphi, z)$, where ρ is radial distance, φ angular coordinate, and z height. In such a case, the potential can be expressed as

$$U(\mathbf{r}) = \int_0^\infty B_n(\rho')G_n^{\mathrm{AX}}(\mathbf{r}, \mathbf{r}')\rho' \, \mathrm{d}\rho', \tag{9.19}$$

where $G_n^{\mathrm{AX}}(\mathbf{r}, \mathbf{r}')$ is a free-space axisymmetric Green's function

$$G_n^{\text{AX}}(\mathbf{r}, \mathbf{r}') = \frac{1}{4\pi} \int_0^{2\pi} \frac{\mathrm{d}U}{|\mathbf{r} - \mathbf{r}'|}, \tag{9.20}$$

$$G_n^{\text{AX}}(\mathbf{r}, \mathbf{r}') = \frac{K(k)}{\pi f_1}. \tag{9.21}$$

The previous expression was taken from [Pozrikidis, 2002] but it has to be multiplied by two to work properly. To evaluate this expression, we need the complete elliptic integral of the first kind

$$K(k) = \int_0^{\frac{\pi}{2}} \frac{\mathrm{d}\theta}{\sqrt{1 - k^2 \sin^2 \theta}} = \int_0^1 \frac{\mathrm{d}t}{\sqrt{(1 - t^2)(1 - k^2 t^2)}}. \tag{9.22}$$

To get the magnetic field

$$B_\rho(\mathbf{r}) = -\frac{\partial U}{\partial \rho} = -\int_0^\infty B_n(\rho) \frac{\partial G_n^{\text{AX}}}{\partial \rho} \rho \, \mathrm{d}\rho, \tag{9.23}$$

$$B_z(\mathbf{r}) = -\frac{\partial U}{\partial z} = -\int_0^\infty B_n(\rho) \frac{\partial G_n^{\text{AX}}}{\partial z} \rho \, \mathrm{d}\rho, \tag{9.24}$$

we can express partial derivatives of the Green's function

$$\frac{\partial G_n^{\text{AX}}}{\partial z} = -\frac{2(z - z')E(k)}{\pi f_1 f_2}, \tag{9.25}$$

$$\frac{\partial G_n^{\text{AX}}}{\partial \rho} = -\frac{K(k)f_2 + E(k)f_3}{\pi \rho f_1 f_2}, \tag{9.26}$$

where substitutions

$$f_1 = \sqrt{(\rho + \rho')^2 + (z - z')^2}, \tag{9.27}$$

$$f_2 = (\rho - \rho')^2 + (z - z')^2, \tag{9.28}$$

$$f_3 = \rho^2 - \rho'^2 - (z - z')^2, \tag{9.29}$$

$$k^2 = \frac{4\rho\rho'}{f_1^2} \tag{9.30}$$

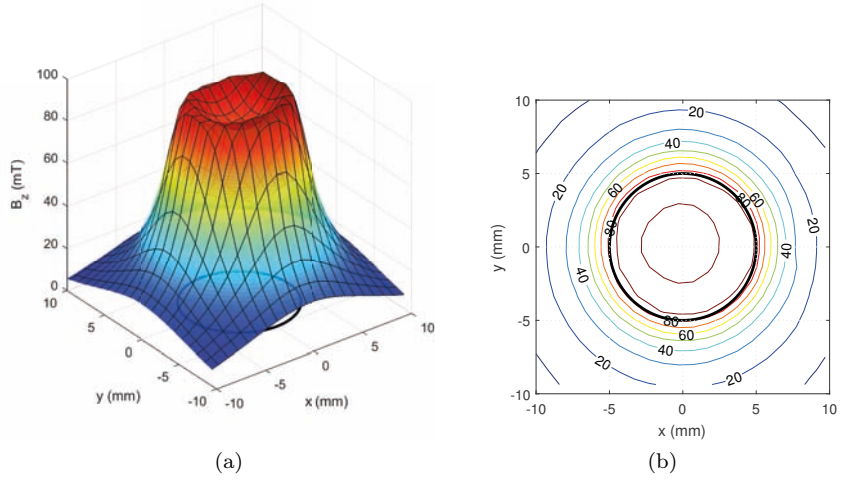were used to make the expressions more compact. The complete elliptic integral of the second kind is

(a)

(b)

Figure 9.6.: B_z in the plane right above the coil for $250\,\text{mA}$.

$$E(k) = \int_0^{\frac{\pi}{2}} \sqrt{1 - k^2 \sin^2 \theta} \, \mathrm{d}\theta = \int_0^1 \frac{\sqrt{1 - k^2 t^2}}{\sqrt{1 - t^2}} \, \mathrm{d}t. \tag{9.31}$$

To use this method, we have to know the magnetic field on the boundary. Therefore, we measured the z-component of the field in the horizontal plane right above the coil. The measured field is shown in Fig. 9.6. Although the platform is not axially symmetric, as was mentioned earlier, measured data show an axially symmetric field.

9.1.4. Comparison

All the discussed models were compared with the measured data. Figure 9.7 shows the relative error in the magnitude of the magnetic flux density for individual models. From the comparison, we can deduce that the best model (at least with respect to its complexity) is the dipole model. The error within the inspected area is approximately $5\,\%$. The dipole model offers good approximation for fixed height for which it is calibrated. Though the accuracy of the numerical model is also very good, its computation demands make it a poor candidate for use in a real-time control system. For the numerical simulations, we need to know the relative permeability of the iron.

(c) Axia   function
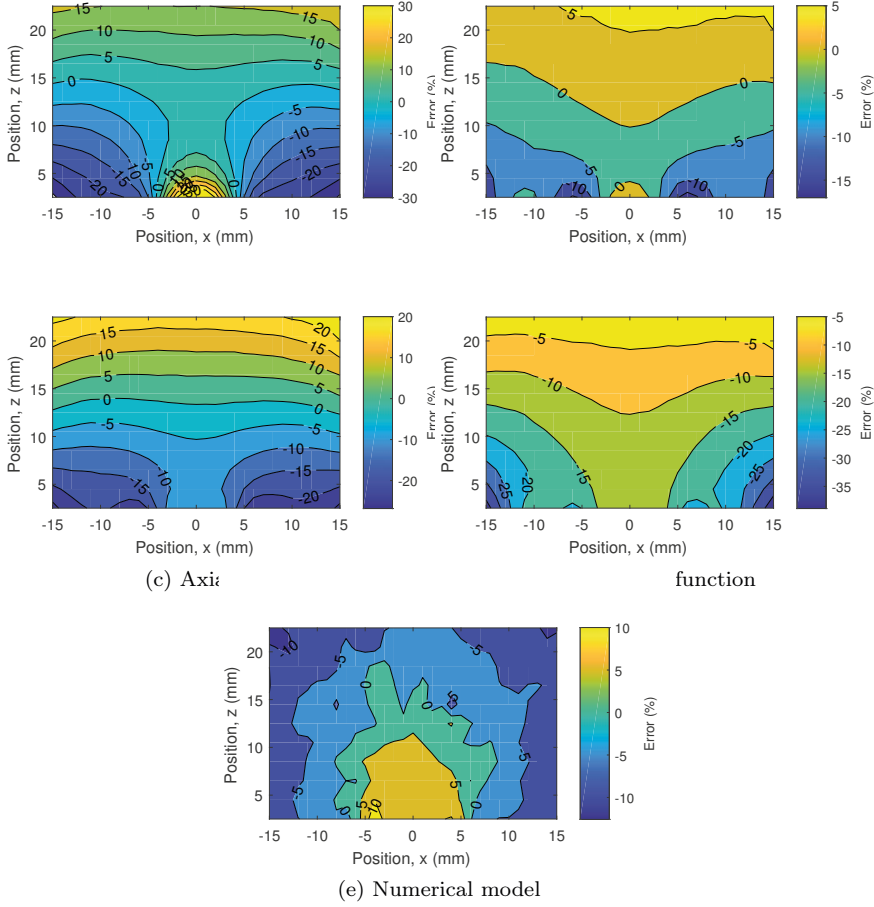

(e) Numerical model

Figure 9.7.: Comparison of mathematical models of the magnetic field of a
            single coil against measured data.

According to the B-H curve, this value should be in the range of 30–300. To
match measurement and simulation we used $\mu_r = 50$.

101

9.2. Magnetic force

9.2.1. Induced dipole moment

If a magnetizable object is placed into a non-uniform magnetic field, it experiences a magnetic force. The force can be estimated as the force exerted on a magnetic dipole within a non-uniform field [Jones, 1995]

$$\mathbf{F} = (\mathbf{m} \cdot \nabla)\mathbf{B}, \tag{9.32}$$

where $\mathbf{m}$ stands for effective magnetic dipole and $\mathbf{B}$ for the magnetic flux density. In the case when the object is made from magnetically linear material and has a spherical shape with radius R, the effective moment is

$$\mathbf{m} = 4\pi R^3 K \mathbf{H}, \tag{9.33}$$

where K stands for the *Clausius-Mossotti function* (or Clausius-Mossotti factor). The CM function is defined as

$$K = \frac{\mu_2 - \mu_1}{\mu_2 + 2\mu_1}, \tag{9.34}$$

where μ_1 and μ_2 are permeability of the surroundings and the object, respectively. We can express the magnetic force as[6]

$$\mathbf{F} = \frac{2\pi R^3 K}{\mu_1} \nabla \mathbf{B}^2 = k \nabla \mathbf{B}^2, \tag{9.35}$$

For the magnetic field that is created by a magnetic monopole (9.5), this equation can be expressed as

$$\mathbf{F} = k \frac{q_m^2}{16\pi^2} \nabla \frac{1}{|\mathbf{r}|^4} = k \frac{q_m^2}{16\pi^2} \nabla \frac{1}{(x^2 + y^2 + z^2)^2}, \tag{9.36}$$

where an x-component of the force is equal to

$$F_x = -k \underbrace{\frac{q_m^2}{4\pi^2}}_{c} \frac{x}{(x^2 + y^2 + z^2)^3}. \tag{9.37}$$

Therefore the magnetic force can be described by a function

$$F_x(i, x, y) = f^2(i) \frac{cx}{(x^2 + y^2 + d^2)^3}, \tag{9.38}$$

---

[6]Because $\nabla(\mathbf{B} \cdot \mathbf{B}) = 2(\mathbf{B} \cdot \nabla)\mathbf{B} + 2\mathbf{B} \times (\nabla \times \mathbf{B})$ and $\nabla \times \mathbf{B} = 0$
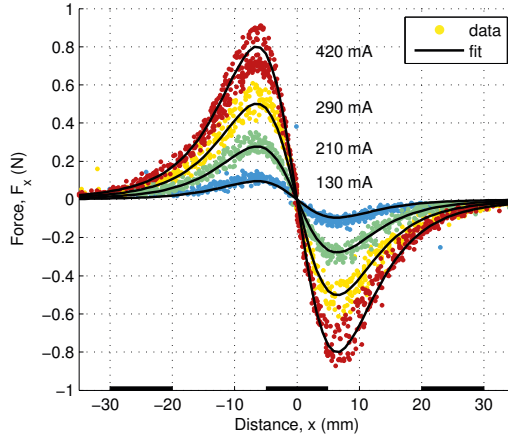
Figure 9.8.: Measurement of magnetic force exerted on the steel ball of radius 30 mm by a single coil. Data set is fitted by a function using a least squares method.

where the part $f(i)$ was already found during the measurement of the magnetic field, c can be calculated according to (9.37) (for our case it is approximately equal to $-1.81 \cdot 10^{-9}\,\mathrm{N\,m}$), and d stands for the z-position of the ball's center, in our case 15 mm.

This model was verified and further improved using an *experimental identification* of the system. To do so, a measurement of the force exerted on the ball was done in such a way that a force gauge was used to push the ball from the equilibrium above an energized coil while the ball's position and the measured force were recorded by the computer. In this way we obtained a data set representing how force evolves with position. The measurement was repeated for various values of the current and for coils in different locations to see the effect of their position in the array. The results are depicted in Fig. 9.8.

It is noticeable that for a particular position and current the measured force has a wide range. In fact, the force is either on the upper or lower bound of this range. Force on the upper limit of magnitude was measured when the ball was pushed away from the coil, and the force on the lower limit was obtained when the ball moved towards the coil (values between those limits correspond to change of direction). The relative difference in the force is approximately 20 %.

Experimental identification

The reason for this observation is not clear. The difference might be explained by hysteresis of the ball's material because when the external field is increased the induced dipole is weaker, and when the field is decreased (moving away) the dipole is stronger. Nevertheless, this was not confirmed. We have tried leaving the ball at one position and changing the current, and there was no difference in the force.

The measured data were fitted using the least squares method by the function

$$F_x(i, x, y) = f^2(i) \frac{-1.85 \cdot 10^{-9} x}{\left(x^2 + y^2 + (14.5 \cdot 10^{-3})^2\right)^3}, \qquad (9.39)$$

The equation for the y-component of the force can be obtained by switching x and y. It is worth noticing that it is not possible to generate a repulsive force (because the $f(i)$ is squared), which is an important feature that has to be considered during control system design.

We can estimate the maximal energy that can be transferred to the ball when it is attracted towards the coil

$$W_{\mathrm{max}} = \int_{-\infty}^{0} F_x(i_{\mathrm{max}}, x, 0) \, \mathrm{d}x, \qquad (9.40)$$

which equals to $10.6\,\mathrm{mJ}$ and corresponds to velocity $0.36\,\mathrm{m\,s^{-1}}$.

9.2.2. Maxwell stress tensor

A method based on the Maxwell stress tensor (MST) offers very accurate results. Therefore it can serve as source of reference data. Due to high computation demands, however, it is not suitable for real-time control systems. The force can be calculated as

$$\mathbf{F} = \oint_{A} (\mathbf{T} \cdot \mathbf{n}) \, \mathrm{d}A \qquad (9.41)$$

where A is the surface enclosing the volume V. $\mathbf{T}$ is the Maxwell stress tensor given by

$$\mathbf{T} = \epsilon(\mathbf{E} \otimes \mathbf{E} - \frac{1}{2}\mathbf{E}^2\mathbf{U}) + \mu(\mathbf{H} \otimes \mathbf{H} - \frac{1}{2}\mathbf{E}^2\mathbf{U}), \qquad (9.42)$$

where $\mathbf{U}$ is the unit tensor. Because in our case the field is only magnetic, we can drop terms related to the electric field. Calculation of the magnetic
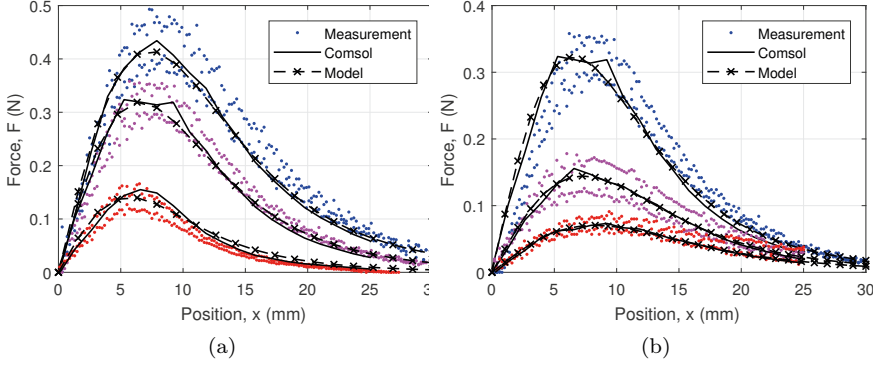
Figure 9.9.: Comparison of magnetic force obtained using Comsol, dipole model, and measurement. (a) Various diameters of the ball (10 mm, 20 mm, and 30 mm). (b) Various thicknesses of the plate (2 mm, 4 mm, and 6 mm).

force based on MST was done using Comsol. Results are compared to the force obtained using the dipole model and to the measured force. Figure 9.9a shows forces for various diameters of the ball and Figure 9.9b for various heights. We can see that with increasing height (it is the thickness of the plate on which the ball rolls) the force quickly decreases. The dipole model was calibrated for each ball and each height individually. The permeability of the iron was set to $\mu_\mathrm{r} = 70$ to match the measurement.

9.2.3. Several coils

So far we have discussed the effect of a single coil. However, the platform contains a set of coils and their effect is combined. To get the total force exerted on the ball by several coils, we can consider the total magnetic field as the sum of fields created by individual coils. This assumption was verified experimentally as shown in Fig. 9.10. The total field for the situation when the coils are activated by the currents

$$\bar{\mathbf{i}} = [i_1, \dots i_N]^\mathrm{T} \tag{9.43}$$
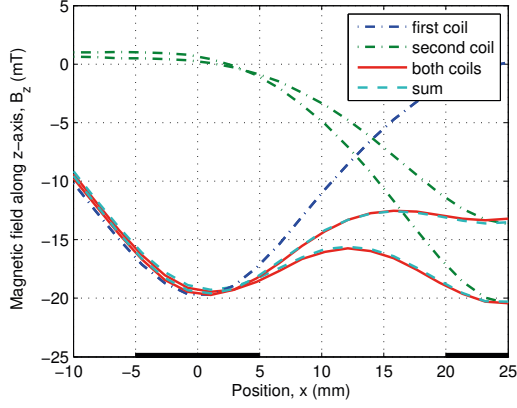
can be then expressed as

Figure 9.10.: Superposition of the magnetic field. Individual magnetic fields were measured for two coils separately and then the total field of two coils was measured and compared against the sum of the individual fields. Two cases are shown: in the first one the current flowing through coils was 250 mA, then the current flowing through the second coil was changed to 170 mA. (First coil is located in position 0 mm and the second one in 25 mm.)

$$\mathbf{B}_{\text{total}}(\bar{\mathbf{i}}, \mathbf{r}) = \sum_{n=1}^{N} \mathbf{B}_{\text{coil}}(i_n, \mathbf{r} - \mathbf{r}_n), \qquad (9.44)$$

where $\mathbf{r}_n$ stands for the position of the n-th coil. The magnetic force can be re-expressed from (9.35) as

$$\mathbf{F}(\bar{\mathbf{i}}, \mathbf{r}) = k\nabla \left(\sum_{n=1}^{N} \mathbf{B}(i_n, \mathbf{r} - \mathbf{r}_n) \right)^2. \qquad (9.45)$$

Let us define vectors of individual contributions

$$\bar{\mathbf{f}}(\bar{\mathbf{i}}) = \begin{bmatrix} f(i_1) \\ \vdots \\ f(i_N) \end{bmatrix}, \ \bar{\mathbf{B}}_a(\mathbf{r}) = \begin{bmatrix} B_a(\mathbf{r} - \mathbf{r}_1) \\ \vdots \\ B_a(\mathbf{r} - \mathbf{r}_N) \end{bmatrix}, \ a \in \{x, y, z\}, \qquad (9.46)$$

where $\bar{\mathbf{f}}(\bar{\mathbf{i}})$ describes how the individual fields are scaled by the change of the currents and $\bar{\mathbf{B}}_a(\mathbf{r})$ is a vector of a-components (x, y, and z) of the magnetic field in position $\mathbf{r}$ (the bar above vectors indicates that elements correspond to individual coils).

For the sake of clarity, only one component of the force will be expressed

$$F_x(\bar{\mathbf{i}}, \mathbf{r}) = k \frac{\partial}{\partial x} \left(\sum_{a=x,y,z} \bar{\mathbf{f}}^{\mathrm{T}}(\bar{\mathbf{i}}) \bar{\mathbf{B}}_a(\mathbf{r}) \right)^2, \tag{9.47}$$

which can be expressed as a standard quadratic form

$$F_x(\bar{\mathbf{i}}, \mathbf{r}) = \bar{\mathbf{f}}^{\mathrm{T}}(\bar{\mathbf{i}}) \underbrace{\left(2k \sum_{a=x,y,z} \frac{\partial \bar{\mathbf{B}}_a(\mathbf{r})}{\partial x} \bar{\mathbf{B}}_a^{\mathrm{T}}(\mathbf{r}) \right)}_{\mathbf{G}_x(\mathbf{r})} \bar{\mathbf{f}}(\bar{\mathbf{i}}). \tag{9.48}$$

This equation is an equivalent of the equation for cDEP (5.1). Diagonal entries of the matrix $\mathbf{G}_x(\mathbf{r})$ represent the influence of the individual coils and the off-diagonal entries represent their interaction. If the interaction between the coils is negligible (it means the magnetic fields of the coils do not overlap significantly), the force can be further simplified to a form where only the diagonal entries are taken into account and we can express the vector of magnetic force as

$$\mathbf{F}(\bar{\mathbf{i}}, \mathbf{r}) = \begin{bmatrix} G_{x_{1,1}}(\mathbf{r}) & \cdots & G_{x_{N,N}}(\mathbf{r}) \\ G_{y_{1,1}}(\mathbf{r}) & \cdots & G_{y_{N,N}}(\mathbf{r}) \end{bmatrix} \begin{bmatrix} f(i_1)^2 \\ \vdots \\ f(i_N)^2 \end{bmatrix}. \tag{9.49}$$

This means that it is possible to get the total force simply as a sum of forces created by individual coils. In our case, the magnetic fields of coils overlap, so the off-diagonal entries should be non-zero. Nonetheless, experimentally we have found that the simplified model that takes into account only the diagonal entries fits very well, as is shown in Fig. 9.11. The off-diagonal entries would cause an increase in the magnetic force in the region where the individual fields overlap, which would make the difference between the model and the measurement worse.
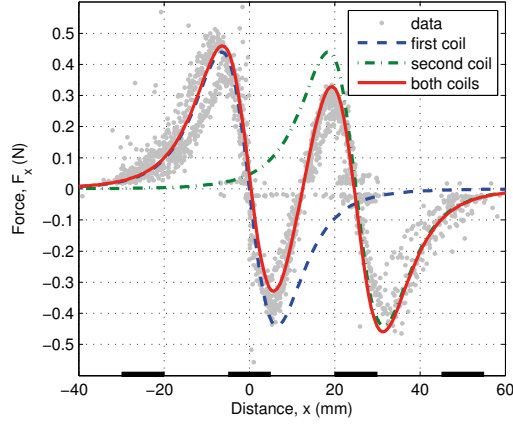
Figure 9.11.: Superposition of the force. The total force of two activated
coils was measured and compared with the model that does not
involve interaction of fields. Force from the model of individual
coils is shown as well. Coils are in positions 0 mm and 25 mm,
and flowing current is set to 250 mA as in the case in Fig. 9.10.

9.3. Ball dynamics

In the previous section, we derived the magnetic force exerted on the ball
by several coils. Here, we focus on the motion of the ball (dynamics). Let
us assume that the ball moves by rolling without slipping, which leads to a
motion constraint

$$0 = \dot{x} - R\omega_y, \quad 0 = \dot{y} + R\omega_x. \tag{9.50}$$

Let us express the kinetic co-energy

$$K^* = \frac{1}{2} J_{\text{ball}} \left(\omega_x^2 + \omega_y^2 + \omega_z^2 \right) + \frac{1}{2} m \left(\dot{x}^2 + \dot{y}^2 \right), \tag{9.51}$$

and substitute for $\boldsymbol{\omega}$ from the constraint (9.50) and for the moment of inertia
of the ball $J_{\text{ball}} = \frac{2mR^2}{5}$. Thus,

$$K^* = \frac{1}{2} \frac{2mR^2}{5} \omega_z^2 + \frac{1}{2} \frac{7m}{5} \left(\dot{x}^2 + \dot{y}^2 \right). \tag{9.52}$$

From the Euler-Lagrange equation we get

$$\ddot{x} = \frac{5}{7m}F_x, \quad \ddot{y} = \frac{5}{7m}F_y, \quad \dot{\omega}_z = \frac{5}{2mR^2}M_z. \tag{9.53}$$

If the orientation of the ball is of interest, first it is necessary to choose how to parametrize it. Here *Euler angles* in the sequence ZXZ are used, giving a rotation matrix

$$\mathbf{R} = \mathbf{R}_z(\phi)\mathbf{R}_x(\theta)\mathbf{R}_z(\psi). \tag{9.54}$$

From the matrix, the angular rates can be expressed

$$\boldsymbol{\omega} = \begin{bmatrix} -\frac{\dot{y}}{R} \\ \frac{\dot{x}}{R} \\ \omega_z. \end{bmatrix} = \begin{bmatrix} \dot{\theta}\cos(\phi) + \dot{\psi}\sin(\phi)\sin(\theta) \\ \dot{\theta}\sin(\phi) - \dot{\psi}\cos(\phi)\sin(\theta) \\ \dot{\phi} + \dot{\psi}\cos(\theta) \end{bmatrix}, \tag{9.55}$$

and this set of equations can then be solved for the time derivatives of the Euler angles to get differential equations

$$\dot{\phi} = \omega_z + \cot(\phi)\cos(\theta)\frac{\dot{x}}{R} + \cot(\theta)\sin(\phi)\frac{\dot{y}}{R},$$
$$\dot{\theta} = \sin(\phi)\frac{\dot{x}}{R} - \cos(\phi)\frac{\dot{y}}{R}, \tag{9.56}$$
$$\dot{\psi} = -\frac{\cos(\phi)}{\sin(\theta)}\frac{\dot{x}}{R} + \frac{\sin(\phi)}{\sin(\theta)}\frac{\dot{y}}{R}.$$

9.3.1. Damping

If we let the ball oscillate around the equilibrium above an activated coil, we observe damped oscillations. We assume damping of two kinds. The first originates in mechanical contact of the ball and the foil giving rise to rolling resistance. The second occurs due to the motion of a conducting object within a magnetic field and is related to so-called *eddy currents* (also called *Foucault currents*).

Rolling resistance does not depend on the velocity and a conventional model is

$$\mathbf{F}_{\mathrm{rr}} = -C_{\mathrm{rr}}F_{\mathrm{N}}\frac{\mathbf{v}}{|\mathbf{v}|}, \tag{9.57}$$

where C_{rr} is a dimensionless *coefficient of rolling resistance* (it is approximately 0.001 for a steel ball on steel[7]) and F_{N} is a normal force, which is a sum of gravity and a z-component of the magnetic force.

It would be difficult to derive the exact mathematical model of the eddy currents for our platform. Therefore, the mathematical model is based on the experimental identification.

Eddy currents are caused by the change of the magnetic flux. Thus, we assume the magnitude of the eddy currents to be proportional to the velocity and derivation of the magnetic field in the direction of the velocity. Force caused by the eddy currents should be then proportional to the eddy currents and the magnetic field. Nevertheless, in experiments, it turned out that the best approximation of the force is proportional to the derivation of the magnetic field

$$\mathbf{F}_{\mathrm{eddy}} = -C_{\mathrm{eddy}} \left(\mathbf{v} \cdot \nabla |\mathbf{B}| \right) \frac{\mathbf{v}}{|\mathbf{v}|}, \tag{9.58}$$

where C_{eddy} is a coefficient of damping due to the eddy currents. By experimental identification we found values of the coefficients to be $C_{\mathrm{rr}} = 0.115$ and $C_{\mathrm{eddy}} = 4.25 \cdot 10^{-4}$. The output of the mathematical model in comparison to experiments is shown in Fig. 9.12. We can see that lower currents lead to lower frequency and lower damping of oscillations.

In addition, we can compare the model and the real system by plotting acceleration versus position in Fig. 9.13, where the effect of the velocity (coded by the color) also can be seen. Both plots are almost the same, but there is an interesting difference. The real system has the biggest acceleration for velocities around zero. This is not captured in the model and the reason is not known. This, however, does not cause a substantial difference in resulting behavior.

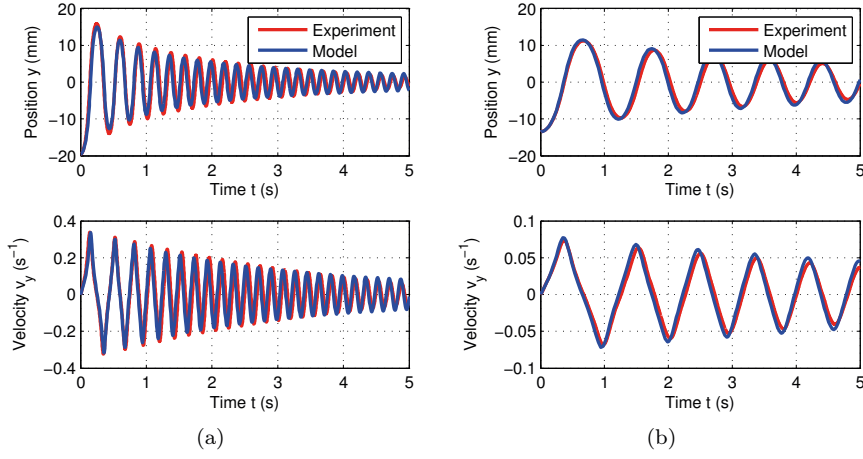[7]https://en.wikipedia.org/wiki/Rolling_resistance

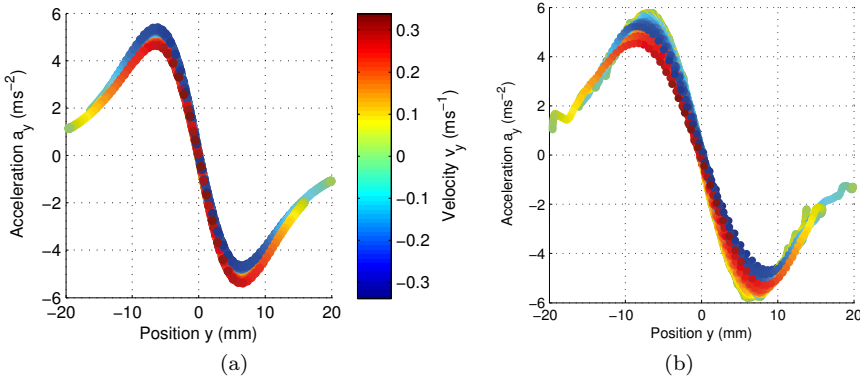Figure 9.12.: Comparison of the model and measured data during transient of the ball when a coil is activated.

Figure 9.13.: Transient response of the ball when a coil is activated. Comparison of (a) the model and (b) measured data.

10

Control

In this chapter we will present examples of feedback control algorithms that can be examined using the platform. As was shown in the section on modeling, the platform is a nonlinear dynamical system with multiple inputs, so one possible way to control such a system is to use feedback linearization. This amounts to finding a function that generates the system's inputs according to the current state and a newly introduced input so that the system behaves like a linear system with respect to this new input.

10.1. Feedback linearization

Nonlinearity of the system, which is introduced primarily by the magnetic field, can be treated in two independent steps, which means that nonlinearities due to the current and position are separated. First, the relation between the magnetic field generated by one coil and the flowing current is resolved. It can be viewed as a simple input nonlinearity and therefore linearized by adding the inverse function before the input.

The second step is to take into account nonlinear dependence of the magnetic field on the position. As was shown during the description of the mathematical model, the force exerted on the ball is the sum of contributions from individual coils. The task here is to find how to scale individual contributions so that their sum would give a demanded force.

The force exerted on the ball (9.49) has the form

$$\underbrace{\mathbf{F}(\bar{\mathbf{i}}, \mathbf{r})}_{\mathbf{b}} = \underbrace{\begin{bmatrix} G_{x_{1,1}}(\mathbf{r}) & \dots & G_{x_{N,N}}(\mathbf{r}) \\ G_{y_{1,1}}(\mathbf{r}) & \dots & G_{y_{N,N}}(\mathbf{r}) \end{bmatrix}}_{\mathbf{A}} \underbrace{\begin{bmatrix} f(i_1)^2 \\ \vdots \\ f(i_N)^2 \end{bmatrix}}_{\mathbf{x}}. \qquad (10.1)$$

The linearization of the system can be viewed as a problem of finding

the values of currents (or more precisely the scaling factors $f^2(i)$) so that the exerted force is equal to the demanded force (dynamics of the ball are then linear). This means we have to solve the underdetermined system of equations (10.1) for non-negative and bounded x_n (**A** is determined by the position of the ball). Because the system of equations is underdetermined, we have to choose a criterion for the solution. We can take, for example, a 2-norm of the solution to get the least-norm solution. There is no closed-form solution because x_n has to be non-negative, but the problem can be solved numerically as an optimization problem

$$
\begin{aligned}
\underset{\bar{\mathbf{x}}}{\text{minimize}} \quad & ||\bar{\mathbf{x}}|| \\
\text{subject to} \quad & 0 \leq x_n \leq 1 \\
& \mathbf{A}\bar{\mathbf{x}} = \mathbf{b}
\end{aligned}
\tag{10.2}
$$

Alternatively, when the exact solution is not found we can find the approximate solution by solving the problem

$$
\begin{aligned}
\underset{\bar{\mathbf{x}}}{\text{minimize}} \quad & ||\bar{\mathbf{x}}|| + c||\mathbf{A}\bar{\mathbf{x}} - \mathbf{b}|| \\
\text{subject to} \quad & 0 \leq x_n \leq 1
\end{aligned}
\tag{10.3}
$$

Examples of the solution for different conditions are in Fig. 10.1. Currents are obtained from the solution of the optimization problem using the inverse function

$$
i_n = \sqrt{f^{-1}(x_n)}.
\tag{10.4}
$$

10.2. Controller of dynamics

When the system is linearized, we can use standard design approaches for a controller of the ball's dynamics. Here a standard PID controller was used. The controller of dynamics should reflect that the system's inputs are saturated, which means that if too much force is demanded there is no solution of the optimization problem (10.2), and (10.3) has to be used instead. Limits of the magnetic force can be calculated from the mathematical model as

$$
F_x^{\max}(\mathbf{r}) = \sum_{n=1}^{N} \min\left(0, G_{x_{n,n}}(\mathbf{r})\right),
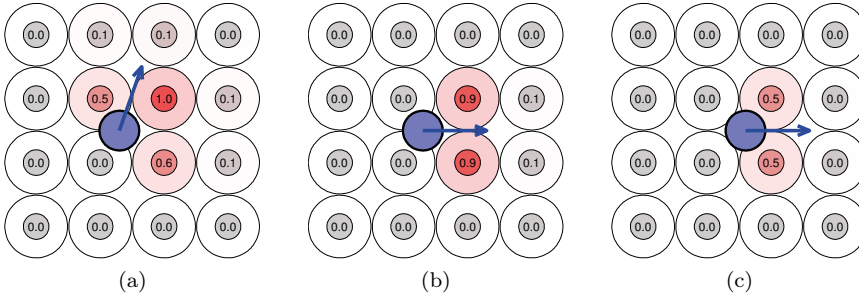\tag{10.5}
$$

Figure 10.1.: Examples of solutions for different demanded force and positions of the ball. Position of the ball is the same in (a) and (b). Force is the same in (b) and (c).

$$F_x^{\min}(\mathbf{r}) = \sum_{n=1}^{N} \max\left(0, G_{x_{n,n}}(\mathbf{r})\right). \tag{10.6}$$

These limits in the plane above the platform are shown in Fig. 10.2, and for two fixed values of y (the best and the worst case) are shown in Fig. 10.3. It is obvious that the maximal force is $0.8\,\mathrm{N}$. We can also calculate the energy that is transferred to the ball during one pass above the rows of coils (when they are switched optimally). For one coil it is, according to (9.40), $10\,\mathrm{mJ}$ and, because the magnetic forces of the coils sum, the total energy is $40\,\mathrm{mJ}$ (which corresponds to ball velocity $0.7\,\mathrm{m\,s^{-1}}$).

We used a simple PID controller to control the position of the object because we wanted to present mainly the control layer that allocates the desired force. In Fig. 10.4 you can see control of position in one direction. Currents flowing through the coils are displayed at appropriate positions corresponding to the positions of the coils. Tracking of a circular trajectory is shown in Fig. 10.5 Error in the position is caused by the dynamic controller.

10.3. Parallel manipulation

Parallel manipulation within the presented control scheme is quite straightforward. It is necessary to extend the control layer responsible for force allocation (feedback linearization) in such a way that it can process more desired forces. Adding new demanded force means adding new equations
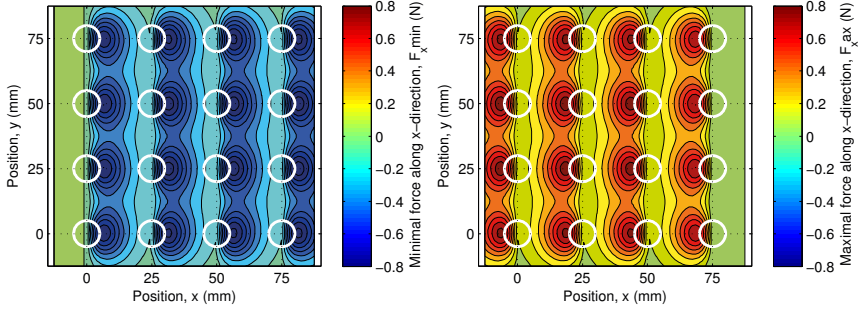
Figure 10.2.: Upper and lower bound for the x-component of the magnetic force. The force is further limited by the fact that x and y components are dependent (y-component can put further restriction on x components). Bounds for the y-component of the force are the same, merely rotated by 90°.
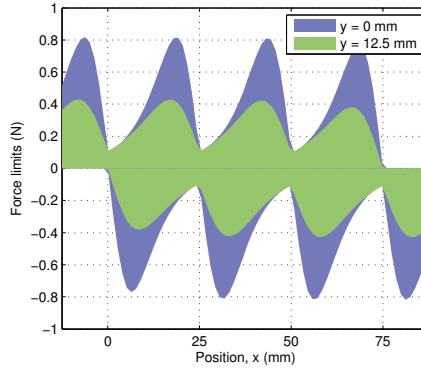

Figure 10.3.: Upper and lower bound for the x-component of the magnetic force.

into (10.1). This extended set of equations can be solved using numerical optimization (10.2).

We tested parallel manipulation on the bigger Magman platform with 8×8 coils. In Fig. 10.6, we show an example of parallel manipulation during which three balls follow a figure-eight trajectory. Fig. 10.7 shows snapshots from the video capturing the experiment. To convey the motion of the balls
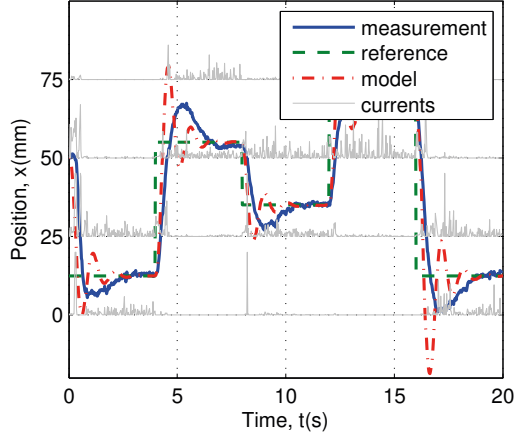
Figure 10.4.: Feedback control of the ball's position. Currents flowing through individual coils are shown at corresponding positions.
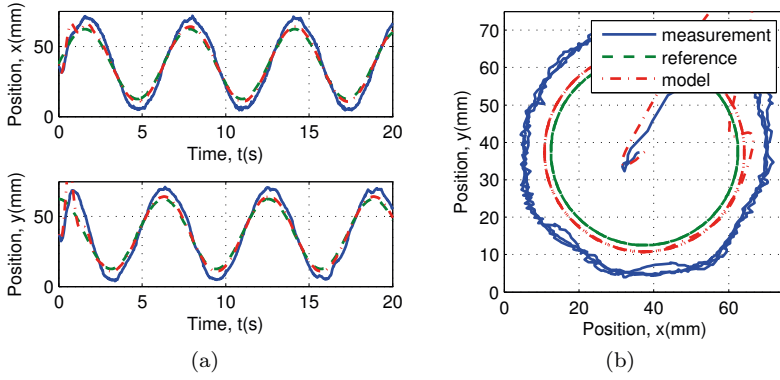

Figure 10.5.: Feedback control of the ball's position following a circular trajectory. (a) The trajectory and (b) the path.

graphically, we added a long exposure effect in post-processing.

Another example of parallel manipulation is in Fig. 10.8, where the balls follow ellipsoidal trajectories. Fig. 10.9 shows snapshots from the video.

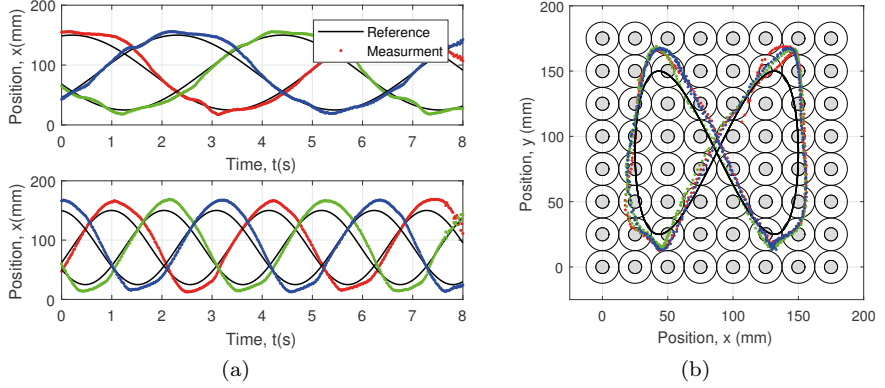Two important aspects of parallel manipulation are mutual interaction

Figure 10.6.: Parallel manipulation of three balls along figure-eight trajectory. (a) The trajectory and (b) the path.
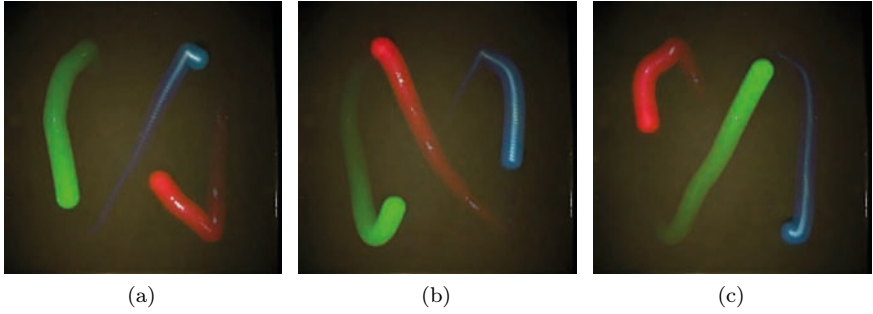

Figure 10.7.: Video snapshots from parallel manipulation of three balls along a figure-eight trajectory.

of objects and scalability. There are two kinds of interactions. Firstly, the objects influence each other through the magnetic field—induced magnetic dipoles exert forces on each other. The mutual magnetic interaction of the objects is in our case negligible, thanks to a relatively small induced dipole, and it does not have to be taken into account. Secondly, the objects may interact mechanically if they collide. However, this must be solved on the level of trajectory planning. If the magnetic interaction was strong, it would be possible to extend the optimization task (10.2) by the mathematical
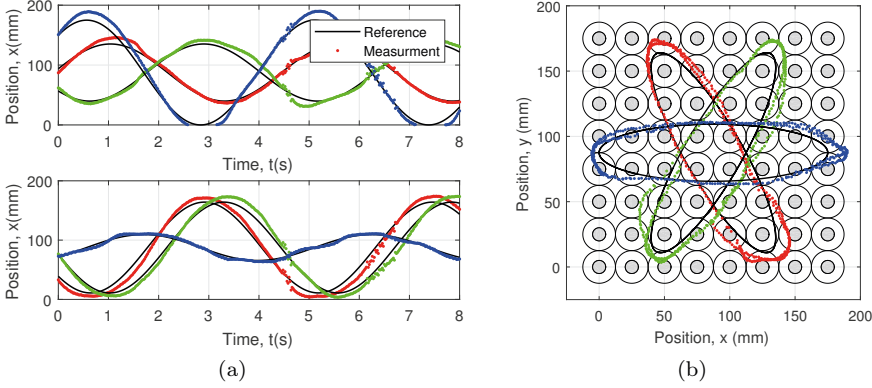
Figure 10.8.: Parallel manipulation of three balls along an ellipsoidal trajectory. (a) The trajectory and (b) the path.
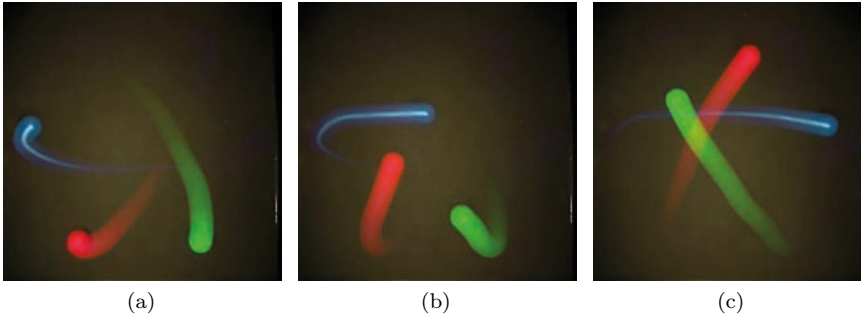

Figure 10.9.: Video snapshots from parallel manipulation of three balls along an ellipsoidal trajectory.

model of interaction. Another problem arising from the proximity of two objects is that the closer they are, the harder it is to set two independent forces. This is a consequence of the fact that the force field is continuous and control signals are limited.

Because one of the main motivations for distributed manipulation is parallel manipulation, a natural question is how the system scales; that is, whether the number of actuators and objects can be increased. Growing numbers of actuators make the optimization task bigger. To deal with a
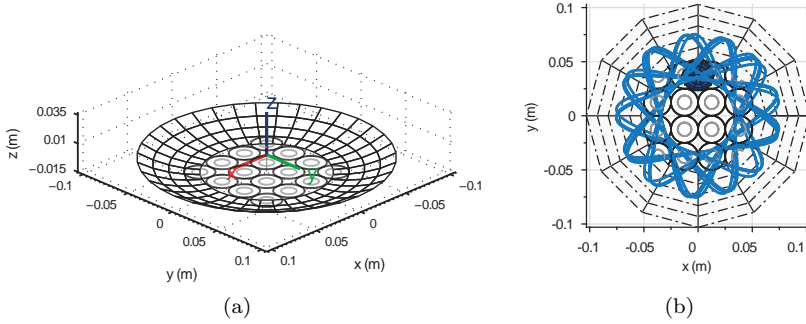
Figure 10.10.: (a) The sketch of the coils and the bowl on top of them. (b) Mathematical model showing an example of a trajectory induced by the bowl.[1]

huge array, it is possible to decompose the force allocation problem into smaller ones. Every actuator has a limited range. Therefore it is reasonable to work with a subset of actuators that influence the object. In our case, it is a 3×3 array of coils for one object. If those smaller sets overlap, they have to solve the optimization problem together. This can be done, for example, using the method of consensus.

10.4. Maintaining oscillation

The Magman platform can be extended by a non-flat surface that changes the natural behavior of the system. This extension brings about new challenges for control system design. We can add, for example, various ramps and bumps and then control the trajectory of the ball or several balls on this curved surface. A basic curved surface is a bowl with a flat region above the coils, as shown in Fig. 10.10a. The bowl changes the dynamics of the system in such a way that it returns objects moving out of the flat region. A simulation using the mathematical models in Fig. 10.10b shows that the object can now oscillate even without the presence of the magnetic field.

The ball in the real system experiences damping caused by rolling resistance. The task for the control system can then be to maintain the oscillations of the ball. The phase portrait of the system in Fig. 10.11a

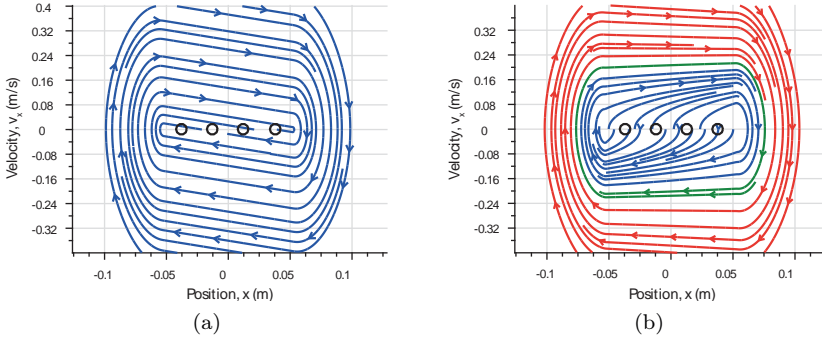---

[1]Reprinted from [Filip, 2015].

Figure 10.11.: Phase portrait of (a) the non actuated system and (b) the system with the controller maintaining oscillations.[2]

shows damped oscillations along the x-axis. To compensate the lost energy, we can introduce a basic controller that exerts a small force F_{m} on the ball in the direction of the motion if the velocity $||v||$ is under the desired value

$$F_{\mathrm{des,x}} = \begin{cases} \mathrm{sgn}(v_x)F_{\mathrm{m}} & \text{if } ||v|| < v_{\mathrm{max}}, \\ 0 & \text{otherwise.} \end{cases} \tag{10.7}$$

This controller sets the desired force $F_{\mathrm{des,x}}$ to the control layer responsible for force allocation (feedback linearization). The phase portrait of the controlled system in Fig. 10.11b shows the state trajectories of the controlled system. The blue color represents a state when the velocity is under the desired value and the controller accelerates the ball. The red color, on the other hand, represents a state when the velocity is above the desired value and damping gradually lowers the velocity. The green trajectory is an approximation of the stable periodic orbit (it is a limit cycle of the system).

10.5. Switching control

In this section we will investigate an example of a control-theoretic problem related to manipulation through a physical field. The aim of the controller is to bring the object to the origin in the shortest time using only switching

---

[2]Reprinted from [Filip, 2015].
[3]Reprinted from [Filip, 2015].

(a) Measured data

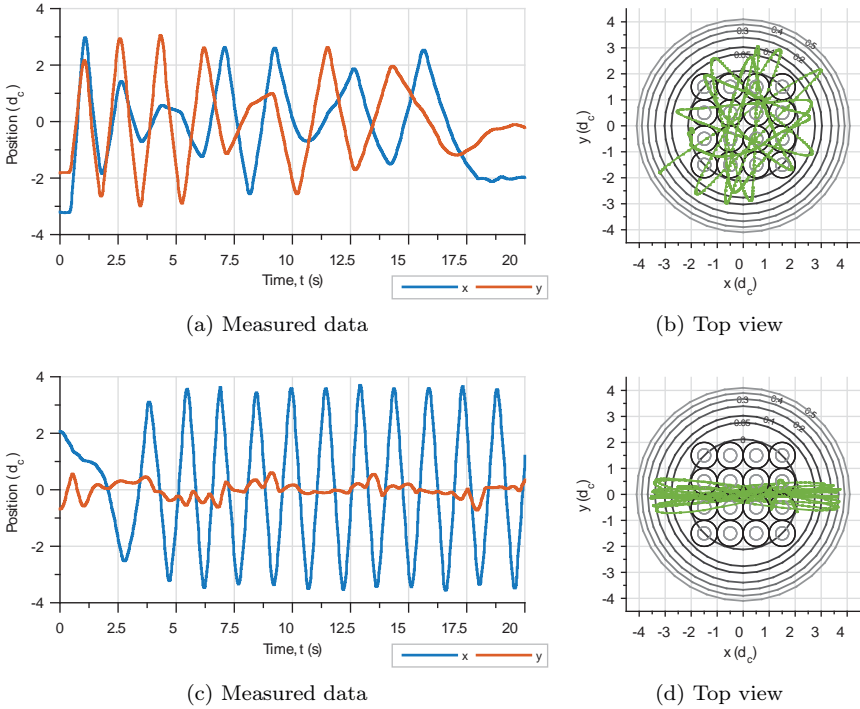(b) Top view

(c) Measured data

(d) Top view

Figure 10.12.: Experiment showing maintaining oscillations of a single ball
on the curved surface. (a,b) System without control—the
response to the initial conditions. (c,d) Controller maintaining
oscillations along x-axis.[3]

control – the current is either flowing or not. Although the Magman platform
is capable of continuous modulation of the currents through the coils, in
some applications the actuator can be turned only on and off. Moreover,
time-optimal control leads to bang-bang control.

10.5.1. One-dimensional nonlinear model

A one-dimensional abstract scenario for the problem studied in this section
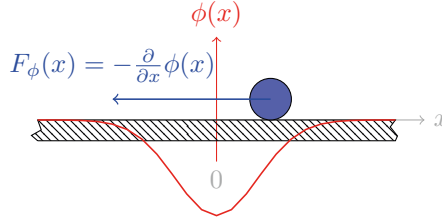is in Fig. 10.13.

Figure 10.13.: One-dimensional restriction of the problem of manipulation by shaping a potential field through a single actuator.

Bell shape potential and the derived force field

We consider the force acting on the object to be derived from the scalar potential that has an inverse bell shape. This is a reasonable assumption in practice for actuators having spatially localized influence (for example, electrodes, coils, etc.). As a simple example, we can consider the potential (magnetic pressure) of a magnetic monopole

$$\phi(x) = \frac{c}{2(x^2 + h^2)^2},\tag{10.8}$$

where c comprises several physical parameters, including the strength of the magnetic monopole, and h is the vertical distance of the monopole from the horizontal plane of manipulation. The exerted force is then

$$F_\phi(x) = -\frac{\partial \phi(x)}{\partial x} = \frac{cx}{(x^2 + h^2)^3}.\tag{10.9}$$

Both the potential and the derived force (field) are shown in Fig. 10.14 and they serve as a reasonable approximation for the Magman platform, as was shown in Section 9.2.1. Furthermore, the inverse bell-shaped potential (namely a Gaussian function) can be used to model a lateral force induced on a microparticle in a laser beam, a phenomenon that has been exploited to create optical tweezers [Gorman and Shapiro, 2011].

Equation of motion

The equation of motion of a single object of mass m in the force field is

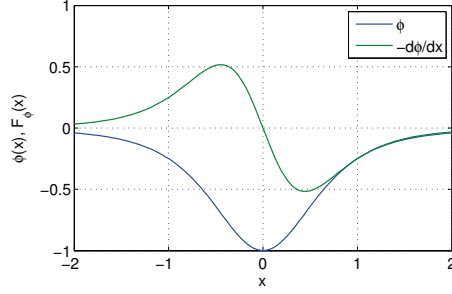$$m\ddot{x}(t) = F_\phi(x, t) - F_{\text{friction}}(\dot{x}).\tag{10.10}$$

Figure 10.14.: The potential (magnetic pressure) and the force derived from it for a magnetic monopole.

An object initially located out of the origin will finally settle at the origin, but this settling process can be rather long and oscillatory if the friction is weak. This gives an incentive for finding a control scheme that steers the object to the origin faster. In the considered setup the friction is very small and ultimately will be ignored.

10.5.2. Bilinear model

Although the complete solution to the control problem must consider the full nonlinear model, the presented profile for the force suggests that linear approximation is feasible in the vicinity of the origin

$$m\ddot{x}(t) = -kx(t)u(t) - b\dot{x}(t), \quad u(t) \in \{0, 1\}, \tag{10.11}$$

where k represents a stiffness coefficient and b parameterizes the linear model of friction. The corresponding linear(ized) state-space model is

$$\begin{bmatrix} \dot{x}(t) \\ \dot{v}(t) \end{bmatrix} = \begin{bmatrix} 0 & 1 \\ 0 & -b/m \end{bmatrix} \begin{bmatrix} x(t) \\ v(t) \end{bmatrix} + \begin{bmatrix} 0 & 0 \\ -k/m & 0 \end{bmatrix} \begin{bmatrix} x(t) \\ v(t) \end{bmatrix} u(t),$$
$$u(t) \in \{0, 1\}. \tag{10.12}$$

This is an instance of a bilinear second-order model

$$\dot{\mathbf{x}}(t) = \mathbf{A}\mathbf{x}(t) + \mathbf{B}\mathbf{x}(t)u(t), \quad u(t) \in \{0, 1\}. \tag{10.13}$$

To make the structure of the model as transparent as possible, we introduce new real constants $\chi, \psi > 0$ and rewrite the state space model as

$$\begin{bmatrix} \dot{x}_1(t) \\ \dot{x}_2(t) \end{bmatrix} = \begin{bmatrix} 0 & 1 \\ 0 & -\chi \end{bmatrix} \begin{bmatrix} x_1(t) \\ x_2(t) \end{bmatrix} + \begin{bmatrix} 0 & 0 \\ -\psi & 0 \end{bmatrix} \begin{bmatrix} x_1(t) \\ x_2(t) \end{bmatrix} u(t),$$

$$u(t) \in \{0, 1\}. \tag{10.14}$$

For this model, a (switching) control will be designed. Finally, it is always possible to transform the system with $\psi \neq 1$ into a new one with $\psi = 1$ by introducing a new state and a time variable

$$\tilde{x}_1(\tilde{t}) = x_1(t), \ \tilde{x}_2(\tilde{t}) = \frac{x_2(t)}{\sqrt{\psi}}, \ \tilde{t} = t\sqrt{\psi}. \tag{10.15}$$

10.5.3. Control strategy

Our aim is to bring the object to the position $x_1(t) = 0$ with the velocity $x_2(t) = 0$ in the shortest time. It is well known that the time-optimal control for constrained linear systems enforces the *bang-bang* control strategy; that is, the control signal is switched between two extreme values. Something similar can be expected here, and in our first attempt to solve the problem we ignore the discrete-valued (in fact, binary) character of the control signal and pretend that it can assume any real value within some bounds.

Indirect approach to optimal control

First, we consider the task of designing a control $u(t)$ that regulates the second-order nonlinear system. Hence the assignment is: bring the system described by

$$\dot{\mathbf{x}}(t) = \mathbf{A}\mathbf{x}(t) + \mathbf{F}(\mathbf{x})u(t), \quad u(t) \in [0, 1] \tag{10.16}$$

from any initial state to the state $(x_1(T), x_2(T)) = (0, 0)$ as fast as possible, that is, minimizing T.

The Hamiltonian (using the control-theoretic convention) for the minimum-time problem is

$$H(x, u, \lambda) = 1 + \boldsymbol{\lambda}^{\mathrm{T}}(t) \left[\mathbf{A}\mathbf{x}(t) + \mathbf{F}(\mathbf{x})u(t) \right]. \tag{10.17}$$

Realizing that matrix $\mathbf{F}(\mathbf{x})$ is zero at the origin because there is no force exerted on the object there, that is,

$$\mathbf{F}(\mathbf{0}) = \mathbf{0}, \tag{10.18}$$

we observe that one of the necessary conditions of the minimum-time optimality, namely

$$H(T) = 0 \tag{10.19}$$

(see, for instance, [Lewis and Syrmos, 1995]) is impossible to satisfy because

$$H(T) = 1 + \underbrace{\boldsymbol{\lambda}^{\mathrm{T}}(T)\mathbf{F}(\mathbf{0})u(T)}_{=0} = 1 \neq 0. \tag{10.20}$$

Obviously, the problem here is that the system is not controllable at the origin. We could possibly drop the requirement that $\mathbf{x}(T) = 0$ and penalize the deviation of the state $\mathbf{x}$ from $\mathbf{0}$ by including the $\varphi(\mathbf{x}(T))$ term penalizing the final state in the cost function. A common choice is $\varphi(\mathbf{x}) = s\mathbf{x}^2(T)$. The boundary condition (10.19) will be replaced by the general condition

$$(\nabla_{\mathrm{x}}\varphi - \boldsymbol{\lambda})^{\mathrm{T}}\Big|_T \, \mathrm{d}\mathbf{x}(T) + H|_T \, \mathrm{d}T = 0. \tag{10.21}$$

The final state $\mathbf{x}(T)$ and the final time T (and hence their differentials) remain independent in this particular situation and therefore, because we still have two independent conditions, we have the same optimization problem as before.

Note that approximating the nonlinear term $\mathbf{F}(\mathbf{x})$ in the vicinity of $\mathbf{x} = 0$ by a linear term $\mathbf{Bx}$ does not make the problem more approachable. Even here, pursuing the indirect approach apparently calls for some more advanced concepts from the domain of bilinear systems. These have been investigated; see [Elliott, 2009], for example. But the results are far from trivial. We have not pursued this any further in this work.

Direct approach— numerical optimal control   Rather than handling the boundary value problem generated by the first-order conditions of optimality as described in the previous section, *direct approaches* are based on discretizing the time axis and reformulating the optimal control problem as an instance of nonlinear programming. Among the popular references are [Betts, 2009, Diehl, 2011, Hargraves and Paris, 1987]. These numerical approaches provide an optimal trajectory as their outcome. It is then necessary to design a feedback controller that will steer the system along the trajectory. We have not pursued that approach here.

Geometric approach   Since the control signal is constrained to assume one of two values (switched on and switched off), the techniques from the discipline of switching control might be invoked. Although there is a formal and rigorous framework for control of switched systems [Liberzon, 2003, Sun, 2005], we use simple and intuitive geometric arguments to arrive at a time-optimal solution.

There are two assumptions for the following development, however. First, we assume that the friction is negligible. With a steel ball rolling on a hard surface this is a good approximation, as the rolling resistance is low[4]. The

---

[4]Damping in the process is of electromagnetic origin—motion of the steel ball through the magnetic field induces eddy currents in the volume of the ball.
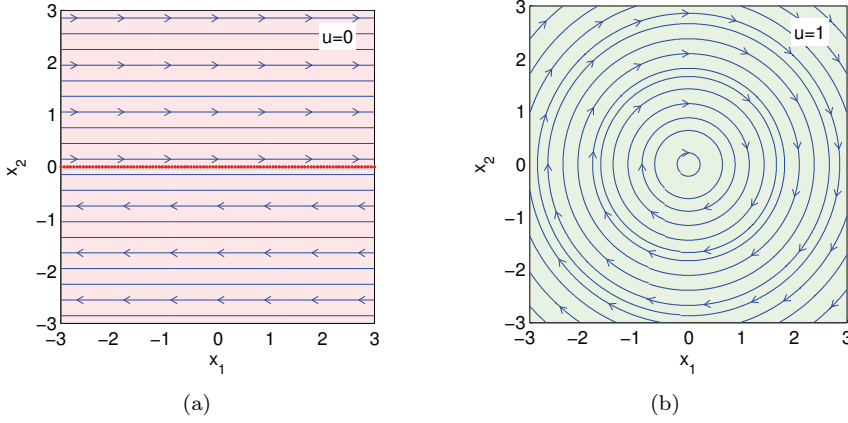
Figure 10.15.: Phase portraits for the field switched on and off. (a) Phase portrait for $u(t) = 0$. Single real eigenvector corresponding to the zero eigenvalue. (b) Phase portrait for $u(t) = 1$. No real eigenvector.

second assumption is that we only consider regulation in the vicinity of the origin, where a bilinear model of the system applies. Making the controller work for a wider range would necessitate using some numerical optimal control methods.

The two phase portraits for the switched-on and switched-off actuator are shown in Fig. 10.15; both portraits were generated for $\chi = 0$ and $\psi = 1$. The phase portrait in Fig. 10.15a confirms a single invariant direction (eigenvector of $\begin{bmatrix} 0 & 1 \\ 0 & 0 \end{bmatrix}$), namely $v = \begin{bmatrix} 1 & 0 \end{bmatrix}^T$ corresponding to $\lambda = 0$. The phase portrait in Fig. 10.15b confirms that there is no invariant direction for the state matrix $\begin{bmatrix} 0 & 1 \\ -1 & 0 \end{bmatrix}$ (no real eigenvector) and the state trajectory for the force field switched on keeps orbiting around the origin; obviously, without any control the force field will never steer the system asymptotically to the origin. The following control strategy is proposed.

Two switching curves are used: a line with a descending slope given by a constant parameter $\gamma > 0$ (that is, $x_2 = -\gamma x_1$), and the vertical axis (that is, $x_1 = 0$). The justification for fixing the latter to the vertical axis will be given later. These two lines split the plane into four segments. The proposed

controller switches the force field off and on when the state vector is in the upper right and lower left segment, since this is the only opportunity to bring the system closer to the origin. Invoking the concept of a switching function, the control is given analytically as

$$u(t) = \begin{cases} 1 & \text{if } \underbrace{\gamma x_1^2(t) + x_1(t)x_2(t)}_{s(t)} > 0, \\ 0 & \text{else,} \end{cases} \qquad (10.22)$$

where the switching function $s(t)$ is indicated. The inequality $s(t) > 0$ is just a compact expression for

$$\begin{aligned} x_2(t) &> -\gamma x_1(t) \text{ if } x_1(t) > 0 \quad \text{or} \\ x_2(t) &< -\gamma x_1(t) \text{ if } x_1(t) < 0. \end{aligned} \qquad (10.23)$$

To gain an initial insight, we will arbitrarily choose $\gamma = \tan(\pi/6) \approx 0.5774$; that is, the switching line is at the angle of $\pi/6$ with the horizontal axis. For this particular value, $\sin(\pi/6) = 1/2$, the norm $\|\mathbf{x}\|_2$ of the error is halved at every switching cycle, which makes the convergence analysis convenient. The analysis will be even more convenient while looking at the phase portrait with the switching control in Fig. 10.16. As can be seen, the state trajectory consists of a sequence of circular arcs and horizontal linear segments. It is possible to find an upper bound on the time needed to halve the initial velocity. Such a time interval is given by three components

$$\tau_{1/2} = \frac{\pi}{2} + \pi/6 + \sqrt{3}, \qquad (10.24)$$

where the first component is the time needed to travel through the upper right quadrant with the force field switched on; hence it constitutes an upper bound on the time needed to reach the horizontal access from an initial state somewhere in the upper right quadrant. The second component is exactly the time required to travel along the circular arc of $\pi/6$ from the horizontal axis to the switching line. The last component is the time needed to travel along the horizontal line in the absence of the force field. It comes from the observation that the length of the segment is $d\cos(\pi/6)$ and the constant velocity is $d/2$. It can also be written as $\cot(\pi/6)$.

For an arbitrary switching angle α, to which the controller parameter γ corresponds, an estimate of the upper bound of the time needed to reduce the norm of the regulation error to a given amount, say, to one half, possibly by taking multiple rounds (oscillation periods), is
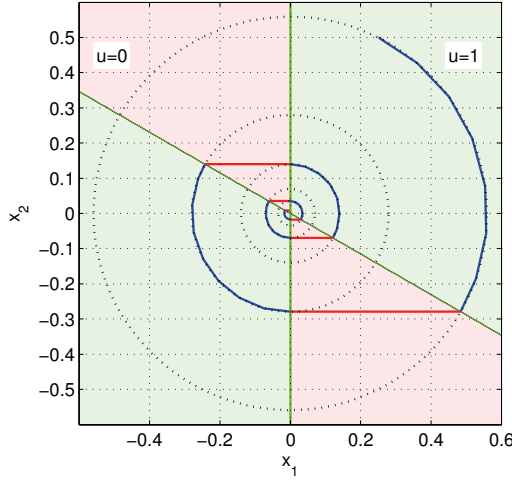
Figure 10.16.: $x_1(t)$ versus $x_2(t)$ in response to $x_1(0) = 1/4$ and $x_2(0) = 1/2$ for $\gamma = \tan(\pi/6) \approx 0.5774$ and no friction. The red segments of the state trajectory correspond to the field switched off. The two green lines are the switching curves.

$$\tau_{1/2} = \frac{\left(\frac{\pi}{2} + \alpha + \cot(\alpha)\right)}{\log_{1/2}(\sin(\alpha))} = \ln(1/2) \frac{\left(\frac{\pi}{2} + \alpha + \cot(\alpha)\right)}{\ln(\sin(\alpha))}. \tag{10.25}$$

The dependence on the switching angle of the time needed to halve the regulation error is shown in Fig. 10.17, including the optimal angle of 0.2433.

It is worth emphasizing that the above-given estimate is only approximate because the reduction of the error is only achieved during a portion of each cycle. This may be more pronounced if the needed number of cycles is small, which is actually the case in our application. This constitutes a challenge to be addressed in the future.

The response of the system with an optimal controller to some nonzero initial conditions is shown in Fig. 10.18. The threshold δ mentioned in the figure will be addressed below.

Observe in Fig. 10.18 that $u(t)$ stops assuming the value 0 after some time; the field remains switched on. This is purely determined by the threshold parameter $-\delta$ substituted for zero on the right-hand side of the inequality in (10.22). The particular setting in Fig. 10.18 was $\delta = 10^{-6}$.
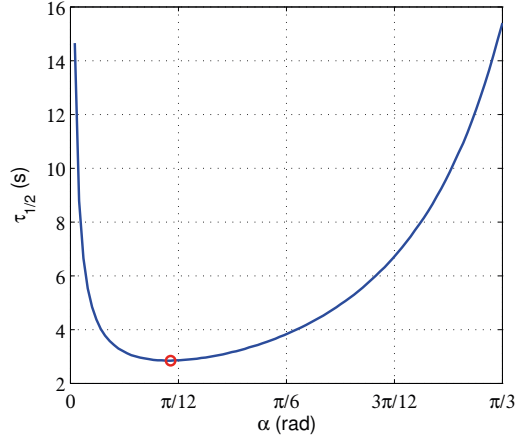
Steady-state error analysis

Figure 10.17.: Time to halve the initial norm of the error as a function of the switching angle α.
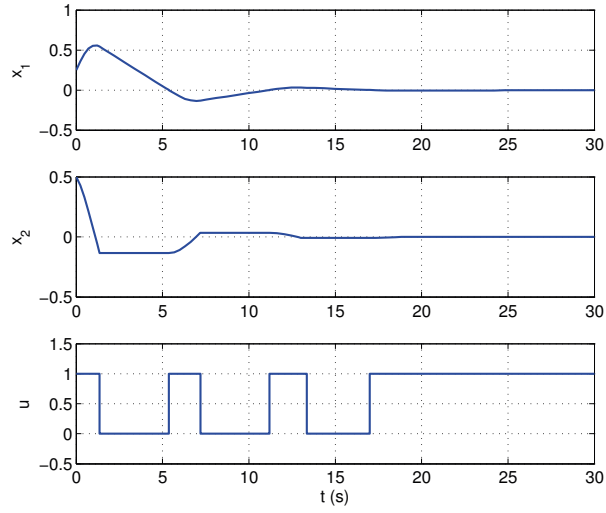

Figure 10.18.: $x_1(t)$ and $x_2(t)$ versus time in response to $x_1(0) = 1/4$ and $x_2(0) = 1/2$ for the optimal controller parameter $\gamma \approx 0.2493$ and the threshold $\delta = 10^{-6}$.
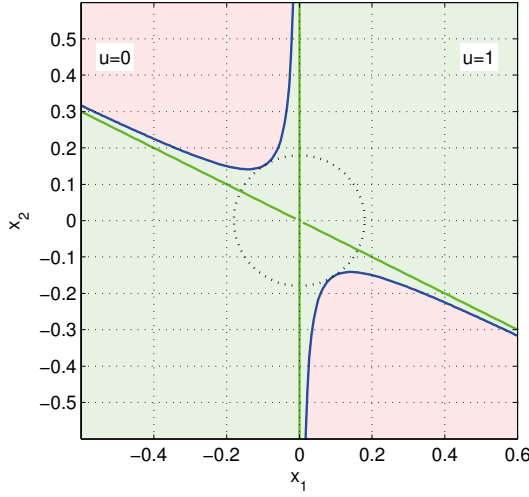
Figure 10.19.: Approximations (blue) of the switching curves (green) for the threshold $\delta = 10^{-1}$.

To gain some insight into the constraint

$$\gamma x_1^2(t) + x_1(t)x_2(t) > -\delta, \tag{10.26}$$

consider $\delta = 10^{-1}$ and plot the approximate switching curve in Fig. 10.19. It is given by

$$x_2(t) = \frac{-\delta}{x_1(t)} - \gamma x_1(t). \tag{10.27}$$

The curve is denoted approximate because the switching angles are not constant; the closer the system is to the origin, the more they move away from the optimal values. Finding the point on the curve closest to the origin we get the bound on the norm of the error

$$\|\mathbf{x}\|_2 < \sqrt{\frac{2\,\delta^2}{\sqrt{\frac{\delta^2}{\gamma^2+1}}} - 2\,\delta\,\gamma}. \tag{10.28}$$

With $\delta = 10^{-1}$ and $\gamma = 1/2$, the bound on the steady state error is 0.18, as shown in Fig. 10.19.

Figure 10.20.: Geometry of the elementary step toward reduction of the norm of the regulation error (radial distance from the origin).
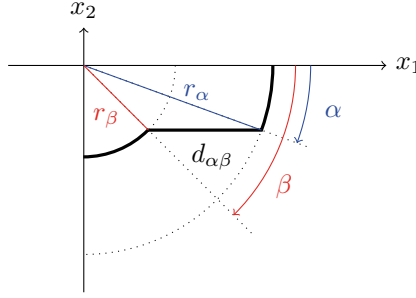
The time intervals needed for traveling along the arcs are independent of the radius—they only depend on the angle; both the traveled distance and the velocity are proportional to the radius. The same holds for the horizontal paths. Hence, the computed optimal angle indeed guarantees optimality for the proposed switching scheme.

Alignment of the switching line The control strategy introduced in the previous section was derived by fixing the controller structure first (the number of switching curves set to two, one of them aligned to the vertical axis) and then by optimizing over the single switching angle γ. It is not obvious, however, if by restricting to this particular controller structure the optimal control strategy has been found. This section and the next provide an analysis. We address first the question of relaxing the alignment of one of the two switching lines to the vertical axis. As can be seen, it only makes sense to switch the force field on and off in the upper left and bottom right quadrants in order to achieve a reduction in the regulation error. Due to symmetry, we will only conduct the analysis for the bottom right quadrant.

Consider an elementary *reduction step* as in Fig. 10.20. It is parameterized by the start angle α, which determines the instant when the field is switched off, and the final angle β, which determines when the field is switched on.

Following the style of analysis in the fixed $\beta = \frac{\pi}{2}$ case, the relative reduction of the radius (error) $r_{\alpha\beta}$ during one step (cycle) of reduction can be obtained as

$$r_{\alpha\beta} := \frac{r_\beta}{r_\alpha} = \frac{\sin(\alpha)}{\sin(\beta)}. \tag{10.29}$$

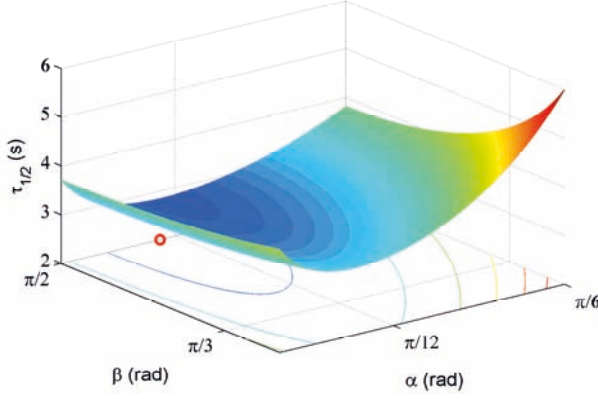The constant-velocity part $d_{\alpha\beta}$ of the trajectory traveled by the object is

Figure 10.21.: Time to halve the regulation error as a function of the switching angles α and β.

$$d_{\alpha\beta} = r_\alpha \cos(\alpha) - r_\beta \cos(\beta). \tag{10.30}$$

Thus the time $t_{\alpha\beta}$ needed for traveling along this constant-velocity segment is

$$t_{\alpha\beta} = \frac{d_{\alpha\beta}}{r_\alpha \sin(\alpha)} = \cot(\alpha) - \cot(\beta). \tag{10.31}$$

The total time needed to reduce the regulation error to $1/2$ of the original value is given by

$$
\begin{aligned}
\tau_{1/2} &= \frac{\frac{\pi}{2} + \alpha + \cot(\alpha) - \cot(\beta) + \left(\frac{\pi}{2} - \beta\right)}{\log_{1/2}\left(\sin\left(\frac{\alpha}{\beta}\right)\right)} \\
&= \ln(1/2)\frac{\pi + \alpha + \cot(\alpha) - \cot(\beta) - \beta}{\ln\left(\sin\left(\frac{\alpha}{\beta}\right)\right)}.
\end{aligned} \tag{10.32}
$$

The above is a nonlinear function of two variables, α and β, which are constrained as $0 \le \alpha \le \beta \le \frac{\pi}{2}$. The graph of the function for a subset of the domain is in Fig. 10.21.

By inspecting the graph, it can be seen that for a given α, the optimal β is on the boundary; that is, $\beta_{\text{optimal}} = \frac{\pi}{2}$.
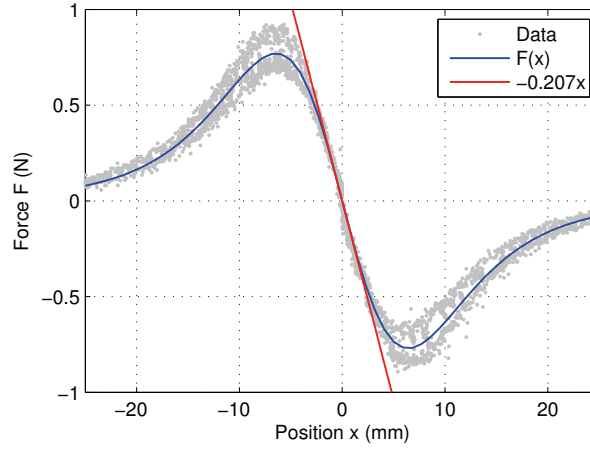
Figure 10.22.: Evolution along the x-axis of the magnetic force exerted on the steel ball.

10.5.4. Experimental verification

Mathematical model

For experimental verification we used the Magman platform with a steel ball having a radius of 15 mm. The mathematical model of the force derived in Section 9.2.1 is

$$F(x) = \frac{-1.823x}{(x^2 + 14.37^2)^3} 10^6, \tag{10.33}$$

where x is measured in millimeters and value of $F(x)$ is in newtons. The force profile is depicted in Fig. 10.22. In addition to this nonlinear model, the original measured data and the linearization of the force in the vicinity of the origin ($F(x) = -kx$, $k = 0.270$) are plotted here. It appears that the linearization approximates the force sufficiently to a distance of around 5 mm from the center of the coil.

The dynamics of the ball is modelled using Newton's second law

$$\ddot{x} = \frac{F(x)}{m_{\text{eff}}} 10^3, \ m_{\text{eff}} = \frac{7}{5}m, \tag{10.34}$$

where m_{eff} is the effective mass, which also includes the influence of the moment of inertia of the ball. The mass of the ball m is 110 g and x is

in millimeters. Therefore, if the coil is turned on, the linearized system is described as a bilinear system

$$\begin{bmatrix} \dot{x}_1(t) \\ \dot{x}_2(t) \end{bmatrix} = \begin{bmatrix} 0 & 1 \\ 0 & 0 \end{bmatrix} \begin{bmatrix} x_1(t) \\ x_2(t) \end{bmatrix} + \begin{bmatrix} 0 & 0 \\ -\psi & 0 \end{bmatrix} \begin{bmatrix} x_1(t) \\ x_2(t) \end{bmatrix} u(t),$$

$$u(t) \in \{0, 1\}, \tag{10.35}$$

$$\psi = \frac{k}{m_{\text{eff}}} 10^3 = 1.344 \cdot 10^3.$$

Controller implementation

A few implementation issues will be discussed here. First, a velocity observer needed to be designed since the direct measurement of velocity is not available and the measurement of position is rather noisy (standard deviation of 0.7 mm). A standard Kalman filter was used to accomplish this task. We incorporated the knowledge of the dependence of force on the position as a nonlinearity at the input of the filter. The filter is crucial for good performance of the controller because the control law relies on the ratio between the velocity and the position; if one of them is not estimated accurately enough, the controller will not operate correctly.

The second implementation issue is that the theoretical results hold for the normalized model ($\psi = 1$). Therefore, unscaling needs to be done by dividing the velocity by $\sqrt{\psi} = 36.7$.

The controller was implemented in Matlab/Simulink and run in External Mode utilizing Real-Time Windows Target. The sampling rate was 1 kHz.

Results

The experimental scenario was such that at the beginning the ball was accelerated to some reference velocity (specifically, $150 \, \text{mm s}^{-1}$) by another controller, and when it reached the origin ($x = 0 \, \text{mm}$) the switching controller proposed in this section was activated. This means that the initial condition for the experiments was zero position and some non-zero velocity. An example of recorded variables (namely measured position, estimated position, estimated velocity, and control signal) is in Fig. 10.23.

We can compare the variables measured on the platform with the variables obtained by the simulation with the linear model. These values, which already have been presented, were transformed to match the non-normalized
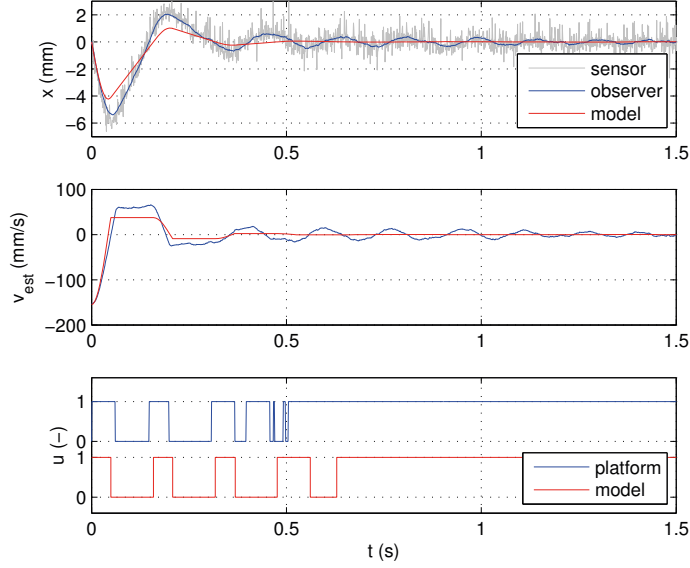
Figure 10.23.: Comparison of the variables measured on the platform and
simulated with the linear model.

system. This means simulated velocity had to be multiplied by $\sqrt{\psi} = 36.7$
and the simulation time was divided by this factor.

It is noticeable that the simulated and the measured control signal are
quite similar at the beginning but later they diverge. This difference can
be partially caused by the fact that the linearized model does not match
the real system with increasing distance of the ball from the coil. Namely,
braking at the beginning is less intensive than it is supposed to be and that
is why the position in the real system diverges from the simulated position.
Nevertheless, the first three pulses of the measured and the modelled control
signal are close. Other pulses of the control signal during the experiment
are not relevant because fluctuation of the estimated position is too high to
bring the ball to absolute rest. Figure 10.24 provides evolutions of the ball
positions during several experiments[5] to assess repeatability. The settling
time of the uncontrolled system is naturally and clearly much longer.

---

[5]Video from the experiment is available at http://youtu.be/5r4IdUrz6Sg

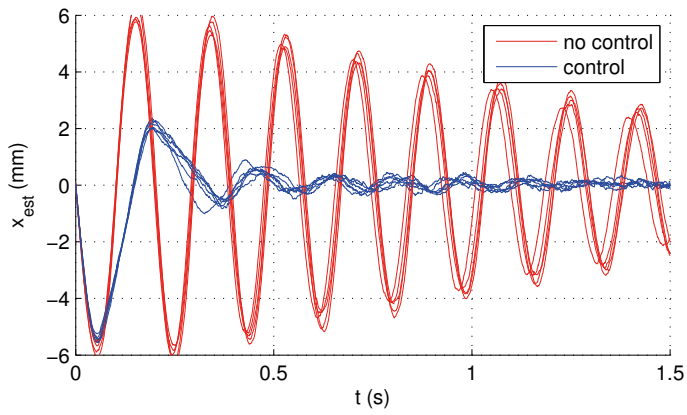Figure 10.24.: Comparison of evolutions of the estimated position (for several runs, to assess repeatability).

.

11
Discussion and concluding remarks

In the preceding discussion dedicated to manipulation using a magnetic field, we first described in detail the development of a test bed for distributed magnetic manipulation. First, the platform hardware was described with attention to parts related to the magnetic field, control, and position measurement of a steel ball.

We then derived several mathematical models that approximate the magnetic field of a solenoid by using the monopole field, the dipole field, the general solution of the Laplace equation, and Green's function. The force acting on the ball was derived from the magnetic field and extended for the case of multiple coils. The equation relating the magnetic force to input currents has a quadratic form, but the matrix was reduced to only the diagonal. We also presented the dynamic model for a rolling ball, including damping. All results from the models were compared to measured values of the magnetic field and force, and to numerical simulations.

Finally, we focused on control systems that can steer one several ball along desired trajectories. To develop a controller that shapes the magnetic field we inverted the model using numerical optimization. Experiments proved the capability of the system to manipulate one and even several objects at once. We also presented two examples of interesting problems that can be demonstrated with the platform: namely, maintaining oscillation and a heuristic strategy for optimal switching control.

Ideas

The presented platform has the potential for other attractive demonstrations and applications both from the visual and research points of view. Here, for illustrative purposes, we describe an interesting preliminary experiment
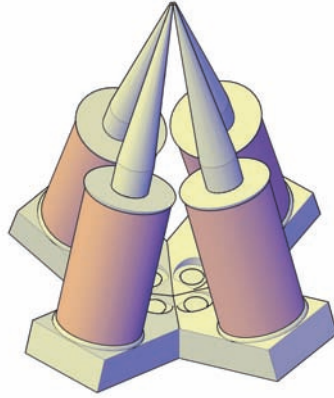
Figure 11.1.: CAD model of a laboratory setup for magnetic micromanipulation.

with the Magman platform and note some examples of using magnetic fields for visual effects.

Micromanipulation

A promising application of distributed manipulation is micromanipulation. Existing systems for magnetic micromanipulation use either a set of coils around the manipulation area or a planar array of coils. Arrays of coils are usually fabricated using lithography and therefore have a limited number of turns. We tried a different approach. Instead of fabricating microscopic coils, we designed sharp iron cores that meet in one point. Figure 11.1 shows a CAD model of the system and in Fig. 11.2 the laboratory system is shown.

We performed preliminary experiments using nickel squares with a side of 50 mm immersed in DI water. Figure 11.3 shows a basic experiment during which the controller sequentially energized individual coils. Each coil was energized for 4 s. Motion was substantially improved using a pulsating current ($f = 5$ Hz).

Ferrofluid and visual effects

A magnetic field can be used to create fascinating visual effects. Photographer Fabian Oerner used a mixture of ferrofluid with watercolors to create
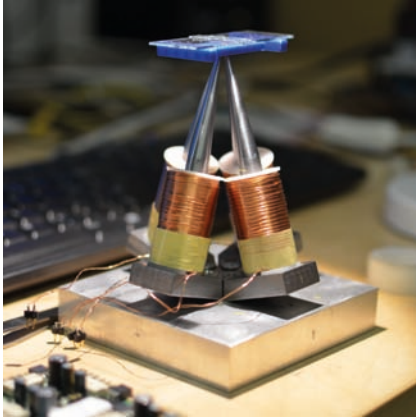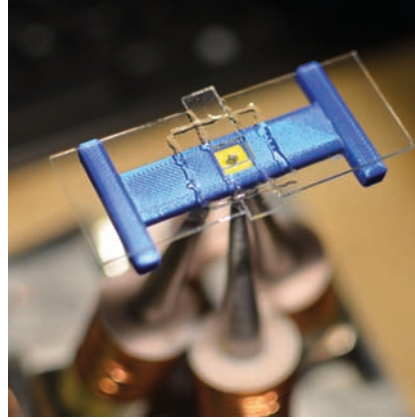
Figure 11.2.: Laboratory setup for magnetic micromanipulation.
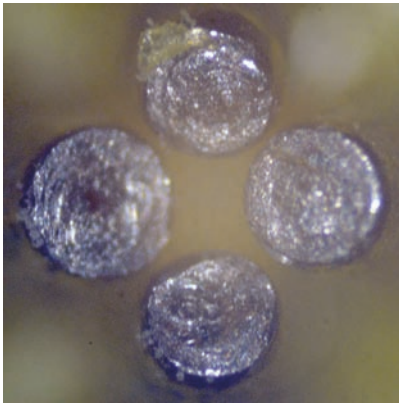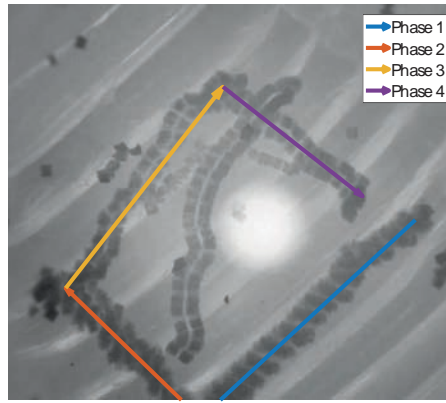
Figure 11.3.: Manipulation area of the system for magnetic micromanipulation. (a) View of the points of the four iron cores through a microscope. (b) Experiment showing manipulation of nickel squares.

Figure 11.4.: Watercolors mixed with a ferrofluid[2].

the beautiful patterns shown in Fig. 11.4. He calls this process *Millefiori*. Zelf Koelman created a Ferrofluid clock, *Ferrolic* [Koelman et al., 2015], shown in Fig. 11.5. A magnetic field viewer called Ferocell (in Fig. 11.4) can be created by a thin layer of ferrofluid between two glass slides[1]. A device called *Tamable Looper* uses an array of coils to animate strings of spherical permanent magnets [Kono and Kakehi, 2012].

---

[1] http://www.instructables.com/id/Ferrocell-Magnetic-Fields-Viewer/
[2] Picture from http://fabianoefner.com/projects/millefiori/
[3] Picture from http://hight3ch.com/ferrofluid-clock/
[4] Picture from http://www.ferrocell.us/
[5] Picture from https://www.aec.at/c/en/tamable-looper/

Figure 11.5.: Ferrofluid clock Ferrolic[3].

Figure 11.6.: Magnetic field viewer Ferrocell[4].

Figure 11.7.: Chain of spherical magnets by Tamable Looper[5].

12
Final conclusions

In this chapter, we provide an overall perspective on the entire work by highlighting the key findings and contributions from our approaches in both the electric field and magnetic field domains. We have already partly summarized and discussed specific aspects of modeling and manipulation at the end of each section.

Feedback control of DEP manipulation

Most of the DEP systems reported in the literature operate in open-loop mode. Systems for DEP micromanipulation described in the literature use either discrete DEP cages, and are therefore limited in resolution, or have limited range of motion because the electrodes encompass the manipulation area. Our proposed feedback control approach has a virtually unlimited range of motion and the resolution of the array does not constrain manipulation accuracy. The proposed control scheme can control both twDEP and cDEP (though only cDEP was demonstrated experimentally) through amplitude and phase modulation. Our system allows parallel manipulation of several objects at once, which was also shown experimentally.

Phase modulation

Systems reported in the literature use mainly amplitude modulation of the voltages applied to the (micro)electrodes to control the force acting on the object. Phase modulation was used only to shift local equilibria or control global motion, but we proposed and verified that phase modulation can control the DEP force locally. Phase modulation has advantages such as simpler implementation and a broader set of achievable forces in comparison to amplitude modulation. In addition, it can control both cDEP and twDEP.

Noise-aided recovery of controllability

We proposed a way of recovering controllability of a system in the situation when two identical objects experience the same force. Our method brings objects to an unstable equilibrium and relies on the intrinsic noise in the system to separate them. We validated this idea experimentally by swapping particles on the parallel electrodes array, which should not be possible theoretically. This result deserves further study from a control theoretical point of view.

New layouts of electrodes for DEP

We designed a layout of electrodes (we call it just a *corner array*) that can be used as a programmable switch for DEP or electroosmosis. Another layout (called just a *four-sector array*) can manipulate several objects in a plane and probably even in 3D—a topic for further experimentation. Both layouts are advantageous because they need only a single-layer fabrication technology.

Test bed for distributed manipulation

We developed a system for magnetic manipulation that can serve as a test bed for distributed manipulation. The controller can be either centralized or decentralized. In comparison to systems reported in the literature, our system moves a ferromagnetic material, which makes the system non-linear. We showed that dynamics of the manipulated objects play an important role and offer challenges for advanced control systems.

Unified mathematical model and way of shaping the electric and magnetic field

For both DEP and magnetophoresis, we derived a mathematical model that is suitable for use in the feedback loop. The models have explicitly expressed inputs and can be executed in real time. In the cases of both electric and the magnetic fields, the models have a similar quadratic form that allows the use of the magnetic system for testing of control manipulation using an electric field, and vice versa.

Instrumentation

Another contribution of this work is also in documenting many practical aspects of manipulation using physical fields. For example, we describe technical details of multi-channel amplitude and phase modulation of voltage, real-time measuring of position using various methods, and even suggest a novel method for real-time estimation of the 3D position of multiple objects.

Future research

In the future, we would like to integrate the twin-beam sensor with the four-sector array to get a compact platform for 3D manipulation of several objects. We want to experimentally verify feedback control of twDEP and a combination of amplitude and phase modulation. Besides, we would like to perform experiments with particles like cells or droplets of liquid. In the magnetic field, our next research includes control of several mechanically joined objects and control of conductive fluids by shaping a magnetic field (magnetohydrodynamics)

Bibliography

[Abbott et al., 2007] Abbott, J. J., Nagy, Z., Beyeler, F., and Nelson, B. J. (2007). Robotics in the Small, Part I: Microbotics. *IEEE Robotics & Automation Magazine*, 14(2):92–103.

[Adekanmbi and Srivastava, 2016] Adekanmbi, E. O. and Srivastava, S. K. (2016). Dielectrophoretic applications for disease diagnostics using lab-on-a-chip platforms. *Lab on a Chip*, 16(12):2148–2167.

[Ataka et al., 2009] Ataka, M., Legrand, B., Buchaillot, L., Collard, D., and Fujita, H. (2009). Design, Fabrication, and Operation of Two-Dimensional Conveyance System With Ciliary Actuator Arrays. *IEEE/ASME Transactions on Mechatronics*, 14(1):119–125.

[Barr and Dudek, 2009] Barr, D. R. W. and Dudek, P. (2009). APRON: A Cellular Processor Array Simulation and Hardware Design Tool. *EURASIP Journal on Advances in Signal Processing*, 2009(1):751687.

[Barr et al., 2013] Barr, D. R. W., Walsh, D., and Dudek, P. (2013). A Smart Surface Simulation Environment. In *2013 IEEE International Conference on Systems, Man, and Cybernetics*, pages 4456–4461.

[Batchelder, 1983] Batchelder, J. S. (1983). Dielectrophoretic manipulator. *Review of Scientific Instruments*, 54(3):300–302.

[Betts, 2009] Betts, J. T. (2009). *Practical Methods for Optimal Control and Estimation Using Nonlinear Programming, Second Edition*. Society for Industrial & Applied Mathematics, Philadelphia, 2nd edition edition.

[Bocchi et al., 2009] Bocchi, M., Lombardini, M., Faenza, A., Rambelli, L., Giulianelli, L., Pecorari, N., and Guerrieri, R. (2009). Dielectrophoretic trapping in microwells for manipulation of single cells and small aggregates of particles. *Biosensors and Bioelectronics*, 24(5):1177–1183.

[Bohringer et al., 1997] Bohringer, K. F., Donald, B. R., MacDonald, N. C., Kovacs, G. T. A., and Suh, J. W. (1997). Computational methods for design and control of MEMS micromanipulator arrays. *IEEE Computational Science and Engineering*, 4(1):17–29.

Bibliography

[Bohringer et al., 1994] Bohringer, K. F., Donald, B. R., Mihailovich, R., and MacDonald, N. C. (1994). A theory of manipulation and control for microfabricated actuator arrays. In *Proceedings IEEE Micro Electro Mechanical Systems An Investigation of Micro Structures, Sensors, Actuators, Machines and Robotic Systems*, pages 102–107.

[Bourbon et al., 1999] Bourbon, G., Minotti, P., Htlin, P., and Fujita, H. (1999). Toward Smart Surfaces Using High-Density Arrays of Silicon-Based Mechanical Oscillators. *Journal of Intelligent Material Systems and Structures*, 10(7):534–540.

[Bourgeois and Goldstein, 2015] Bourgeois, J. and Goldstein, S. (2015). Distributed Intelligent MEMS: Progresses and Perspectives. *IEEE Systems Journal*, 9(3):1057–1068.

[Boutoustous et al., 2010] Boutoustous, K., Laurent, G., Dedu, E., Matignon, L., Bourgeois, J., and Le Fort-Piat, N. (2010). Distributed control architecture for smart surfaces. In *2010 IEEE/RSJ International Conference on Intelligent Robots and Systems (IROS)*, pages 2018–2024.

[Brazey et al., 2018] Brazey, B., Cottet, J., Bolopion, A., Lintel, H. V., Renaud, P., and Gauthier, M. (2018). Impedance-based real-time position sensor for lab-on-a-chip devices. *Lab on a Chip*, 18(5):818–831.

[Böhringer and Choset, 2000] Böhringer, K. F. and Choset, H., editors (2000). *Distributed Manipulation*. Springer US.

[Cappelleri et al., 2014] Cappelleri, D., Efthymiou, D., Goswami, A., Vitoroulis, N., and Zavlanos, M. (2014). Towards Mobile Microrobot Swarms for Additive Micromanufacturing. *International Journal of Advanced Robotic Systems*, 11(9):150.

[Castellanos et al., 2003] Castellanos, A., Ramos, A., González, A., Green, N. G., and Morgan, H. (2003). Electrohydrodynamics and dielectrophoresis in microsystems: scaling laws. *Journal of Physics D: Applied Physics*, 36(20):2584.

[Castillo et al., 2009] Castillo, J., Dimaki, M., and Svendsen, W. E. (2009). Manipulation of biological samples using micro and nano techniques. *Integrative Biology: Quantitative Biosciences from Nano to Macro*, 1(1):30–42.

[Cen et al., 2004] Cen, E. G., Dalton, C., Li, Y., Adamia, S., Pilarski, L. M., and Kaler, K. V. I. S. (2004). A combined dielectrophoresis, traveling wave dielectrophoresis and electrorotation microchip for the manipulation and characterization of human malignant cells. *Journal of Microbiological Methods*, 58(3):387–401.

[Cen et al., 2003] Cen, E. G., Qian, L., and Kaler, K. V. I. S. (2003). An integrated microchip for dielectrophoresis based characterization and manipulation of cells. In *Proceedings of the 25th Annual International Conference of the IEEE Engineering in Medicine and Biology Society (IEEE Cat. No.03CH37439)*, volume 4, pages 3344–3347 Vol.4.

[Chang and Loire, 2003] Chang, D. E. and Loire, S. (2003). Separation of bioparticles using the travelling wave dielectrophoresis with multiple frequencies. In *42nd IEEE International Conference on Decision and Control*, volume 6, pages 6448–6453 Vol.6.

[Chang et al., 2003] Chang, D. E., Loire, S., and Mezic, I. (2003). Closed-form solutions in the electrical field analysis for dielectrophoretic and travelling wave inter-digitated electrode arrays. *Journal of Physics D: Applied Physics*, 36(23):3073–3078.

[Chang and Petit, 2005] Chang, D. E. and Petit, N. (2005). Toward controlling dielectrophoresis. *International Journal of Robust and Nonlinear Control*, 15(16):769 – 784.

[Chang et al., 2006] Chang, D. E., Petit, N., and Rouchon, P. (2006). Time-optimal control of a particle in a dielectrophoretic system. *IEEE Transactions on Automatic Control*, 51(7):1100 – 1114.

[Chowdhury et al., 2015] Chowdhury, S., Jing, W., and Cappelleri, D. J. (2015). Towards Independent Control of Multiple Magnetic Mobile Microrobots. *Micromachines*, 7(1):3.

[Chowdhury et al., 2017] Chowdhury, S., Johnson, B. V., Jing, W., and Cappelleri, D. J. (2017). Designing local magnetic fields and path planning for independent actuation of multiple mobile microrobots. *Journal of Micro-Bio Robotics*, 12(1-4):21–31.

[Coutinho and Will, 1998] Coutinho, M. and Will, P. (1998). A general theory for positioning and orienting 2d polygonal or curved parts using intelligent motion surfaces. In *Robotics and Automation, 1998. Proceedings. 1998 IEEE International Conference on*, volume 1, pages 856–862 vol.1.

Bibliography

[Current et al., 2007] Current, K. W., Yuk, K., McConaghy, C., Gascoyne, P. R. C., Schwartz, J. A., Vykoukal, J. V., and Andrews, C. (2007). A High-Voltage SOI CMOS Exciter Chip for a Programmable Fluidic Processor System. *IEEE Transactions on Biomedical Circuits and Systems*, 1(2):105–115.

[Damsteeg et al., 2017] Damsteeg, J. W., Nageshrao, S. P., and Babuska, R. (2017). Model-based real-time control of a magnetic manipulator system. In *2017 IEEE 56th Annual Conference on Decision and Control (CDC)*, pages 3277–3282.

[Dang et al., 2016] Dang, T. A. T., Bosch-Mauchand, M., Arora, N., Prelle, C., and Daaboul, J. (2016). Electromagnetic modular Smart Surface architecture and control in a microfactory context. *Computers in Industry*, 81:152–170.

[Desai et al., 2007] Desai, J. P., Pillarisetti, A., and Brooks, A. D. (2007). Engineering Approaches to Biomanipulation. *Annual Review of Biomedical Engineering*, 9(1):35–53.

[Diehl, 2011] Diehl, M. (2011). *Numerical Optimal Control*.

[Diller et al., 2012] Diller, E., Floyd, S., Pawashe, C., and Sitti, M. (2012). Control of Multiple Heterogeneous Magnetic Microrobots in Two Dimensions on Nonspecialized Surfaces. *IEEE Transactions on Robotics*, 28(1):172 –182.

[Diller et al., 2013] Diller, E., Giltinan, J., and Sitti, M. (2013). Independent control of multiple magnetic microrobots in three dimensions. *The International Journal of Robotics Research*, 32(5):614–631.

[Dkhil et al., 2014] Dkhil, M., Bolopion, A., Regnier, S., and Gauthier, M. (2014). Modeling and experiments of high speed magnetic micromanipulation at the air/liquid interface. In *2014 IEEE/RSJ International Conference on Intelligent Robots and Systems (IROS 2014)*, pages 4649–4655.

[Dkhil et al., 2017] Dkhil, M., Kharboutly, M., Bolopion, A., Régnier, S., and Gauthier, M. (2017). Closed-Loop Control of a Magnetic Particle at the Air #8211;Liquid Interface. *IEEE Transactions on Automation Science and Engineering*, 14(3):1387–1399.

[Downs, 2005] Downs, R. (2005). Using resistive touch screens for human/machine interface. *Analog Applications Journal, Texas Instruments*.

[Drs, 2012] Drs, J. (2012). *Four-sector microelectrode array for dielectrophoresis (in Czech)*. Bachelor's thesis, Czech Technical University in Prague, Prague, Czech Republic.

[Drs, 2015] Drs, J. (2015). Micromanipulation platform for droplets (in Czech). Master's thesis, Czech Technical University in Prague, Prague, Czech Republic.

[Edwards and Engheta, 2012] Edwards, B. and Engheta, N. (2012). Electric tweezers: negative dielectrophoretic multiple particle positioning. *New Journal of Physics*, 14(6):063012.

[El Baz et al., 2012] El Baz, D., Boyer, V., Bourgeois, J., Dedu, E., and Boutoustous, K. (2012). Distributed part differentiation in a smart surface. *Mechatronics*, 22(5):522–530.

[Elbuken et al., 2009] Elbuken, C., Khamesee, M. B., and Yavuz, M. (2009). Design and Implementation of a Micromanipulation System Using a Magnetically Levitated MEMS Robot. *IEEE/ASME Transactions on Mechatronics*, 14(4):434–445.

[Elliott, 2009] Elliott, D. (2009). *Bilinear Control Systems: Matrices in Action*. Springer Science & Business Media. Google-Books-ID: dH6QpmVoMvkC.

[Erdmann and Mason, 1988] Erdmann, M. and Mason, M. (1988). An exploration of sensorless manipulation. *Robotics and Automation, IEEE Journal of*, 4(4):369–379.

[Fearing, 1995] Fearing, R. S. (1995). Survey of sticking effects for micro parts handling. In *Proceedings 1995 IEEE/RSJ International Conference on Intelligent Robots and Systems. Human Robot Interaction and Cooperative Robots*, volume 2, pages 212–217 vol.2.

[Filip, 2015] Filip, J. (2015). *Extension of the control system for the magnetic manipulator with a non-flat surface*. Bachelor's thesis, Czech Technical University in Prague, Prague, Czech Republic.

[Floyd et al., 2009] Floyd, S., Pawashe, C., and Sitti, M. (2009). Two-Dimensional Contact and Noncontact Micromanipulation in Liquid Using

an Untethered Mobile Magnetic Microrobot. *IEEE Transactions on Robotics*, 25(6):1332 –1342.

[Follmer et al., 2013] Follmer, S., Leithinger, D., Olwal, A., Hogge, A., and Ishii, H. (2013). inFORM: Dynamic Physical Affordances and Constraints Through Shape and Object Actuation. In *Proceedings of the 26th Annual ACM Symposium on User Interface Software and Technology*, UIST '13, pages 417–426, New York, NY, USA. ACM.

[Fromherz and Jackson, 2003] Fromherz, M. and Jackson, W. (2003). Force allocation in a large-scale distributed active surface. *Control Systems Technology, IEEE Transactions on*, 11(5):641–655.

[Fukuta et al., 2006] Fukuta, Y., Chapuis, Y.-A., Mita, Y., and Fujita, H. (2006). Design, fabrication, and control of MEMS-based actuator arrays for air-flow distributed micromanipulation. *Journal of Microelectromechanical Systems*, 15(4):912–926.

[Gagnon, 2011] Gagnon, Z. R. (2011). Cellular dielectrophoresis: Applications to the characterization, manipulation, separation and patterning of cells. *Electrophoresis*, 32(18):2466–2487.

[Gascoyne et al., 2004] Gascoyne, P. R. C., Vykoukal, J. V., Schwartz, J. A., Anderson, T. J., Vykoukal, D. M., Current, K. W., McConaghy, C., Becker, F. F., and Andrews, C. (2004). Dielectrophoresis-based programmable fluidic processors. *Lab on a Chip*, 4(4):299–309.

[Gauthier and Régnier, 2010] Gauthier, M. and Régnier, S., editors (2010). *Robotic Micro-Assembly*. Wiley-IEEE Press, Hoboken, N.J. : Piscataway, N.J, 1 edition edition.

[Georgilas et al., 2012] Georgilas, I., Adamatzky, A., and Melhuish, C. (2012). Manipulating objects with gliders in cellular automata. In *2012 IEEE International Conference on Automation Science and Engineering (CASE)*, pages 936–941.

[Goldberg, 1993] Goldberg, K. (1993). Orienting polygonal parts without sensors. *Algorithmica*, 10(2):201–225.

[Gorman and Shapiro, 2011] Gorman, J. J. and Shapiro, B., editors (2011). *Feedback Control of MEMS to Atoms*. Springer, 2012 edition edition.

[Green et al., 2002] Green, N. G., Ramos, A., and Morgan, H. (2002). Numerical solution of the dielectrophoretic and travelling wave forces for interdigitated electrode arrays using the finite element method. *Journal of Electrostatics*, 56(2):235–254.

[Griffiths, 2017] Griffiths, D. J. (2017). *Introduction to Electrodynamics.* Cambridge University Press, Cambridge, United Kingdom ; New York, NY, 4 edition edition.

[Guo and Zhu, 2015] Guo, X. and Zhu, R. (2015). Controllably moving individual living cell in an array by modulating signal phase difference based on dielectrophoresis. *Biosensors and Bioelectronics*, 68:529–535.

[Gurtner, 2016] Gurtner, M. (2016). Real-time optimization-based control and estimation for dielectrophoretic micromanipulation. Master's thesis, Czech Technical University in Prague, Prague, Czech Republic.

[Gurtner et al., 2017] Gurtner, M., Hengster-Movric, K., and Hurák, Z. (2017). Green's function-based control-oriented modeling of electric field for dielectrophoresis. *Journal of Applied Physics*, 122(5):054903. arXiv: 1703.01980.

[Gurtner and Zemánek, 2016] Gurtner, M. and Zemánek, J. (2016). Twinbeam real-time position estimation of micro-objects in 3d. *Measurement Science and Technology*, 27(12):127003.

[Gurtner and Zemánek, 2017] Gurtner, M. and Zemánek, J. (2017). Ball in double hoop: demonstration model for numerical optimal control. *IFAC-PapersOnLine*, 50(1):2379–2384.

[Hagedorn et al., 1992] Hagedorn, R., Fuhr, G., Muller, T., and Gimsa, J. (1992). Traveling-wave dielectrophoresis of microparticles. *Electrophoresis*, 13(1):49–54.

[Happel and Brenner, 1983] Happel, J. and Brenner, H. (1983). *Low Reynolds number hydrodynamics: with special applications to particulate media.* Springer, The Hague ; Boston : Hingham, MA, USA, 1983 edition edition.

[Hargraves and Paris, 1987] Hargraves, C. R. and Paris, S. W. (1987). Direct trajectory optimization using nonlinear programming and collocation. *Journal of Guidance, Control, and Dynamics*, 10(4):338–342.

Bibliography

[Hosseini et al., 2008] Hosseini, Y., Ikram, S., and Kaler, K. (2008). A CMOS Optical feedback control for high-speed DEP based microfluidic actuation. In *Microsystems and Nanoelectronics Research Conference, 2008. MNRC 2008. 1st*, pages 137 –140.

[Hsu et al., 2016] Hsu, A., Wong-Foy, A., McCoy, B., Cowan, C., Marlow, J., Chavez, B., Kobayashi, T., Shockey, D., and Pelrine, R. (2016). Application of micro-robots for building carbon fiber trusses. In *2016 International Conference on Manipulation, Automation and Robotics at Small Scales (MARSS)*, pages 1–6.

[Huang et al., 1997] Huang, Y., Wang, X. B., Becker, F. F., and Gascoyne, P. R. (1997). Introducing dielectrophoresis as a new force field for field-flow fractionation. *Biophys. J.*, 73(2):1118–1129.

[Huang et al., 1993] Huang, Y., Wang, X. B., Tame, J. A., and Pethig, R. (1993). Electrokinetic behaviour of colloidal particles in travelling electric fields: studies using yeast cells. *Journal of Physics D: Applied Physics*, 26(9):1528–1535.

[Hughes, 2003] Hughes, M. P. (2003). *Nanoelectromechanics in Engineering and Biology*. Nano- and Microscience, Engineering, Technology and Medicine. CRC Press.

[Hughes, 2016] Hughes, M. P. (2016). Fifty years of dielectrophoretic cell separation technology. *Biomicrofluidics*, 10(3):032801.

[Hughes et al., 1996] Hughes, M. P., Pethig, R., and Wang, X.-B. (1996). Dielectrophoretic forces on particles in travelling electric fields. *Journal of Physics D: Applied Physics*, 29(2):474–482.

[Hunt et al., 2007] Hunt, T. P., Issadore, D., and Westervelt, R. M. (2007). Integrated circuit/microfluidic chip to programmably trap and move cells and droplets with dielectrophoresis. *Lab on a Chip*, 8(1):81–87.

[Ishii et al., 2012a] Ishii, H., Lakatos, D., Bonanni, L., and Labrune, J.-B. (2012a). Radical Atoms: Beyond Tangible Bits, Toward Transformable Materials. *interactions*, 19(1):38–51.

[Ishii and Ullmer, 1997] Ishii, H. and Ullmer, B. (1997). Tangible Bits: Towards Seamless Interfaces Between People, Bits and Atoms. In *Proceedings of the ACM SIGCHI Conference on Human Factors in Computing Systems*, CHI '97, pages 234–241, New York, NY, USA. ACM.

[Ishii et al., 2012b] Ishii, K. S., Hu, W., and Ohta, A. T. (2012b). Cooperative Micromanipulation Using Optically Controlled Bubble Microrobots. *2012 Ieee International Conference on Robotics and Automation (icra)*, pages 3443–3448. WOS:000309406703069.

[Issadore et al., 2009] Issadore, D., Franke, T., Brown, K. A., Hunt, T. P., and Westervelt, R. M. (2009). High-Voltage Dielectrophoretic and Magnetophoretic Hybrid Integrated Circuit/Microfluidic Chip. *Journal of Microelectromechanical Systems*, 18(6):1220–1225.

[Jackson, 1998] Jackson, J. D. (1998). *Classical Electrodynamics Third Edition*. Wiley, New York, 3 edition edition.

[Jesús-Pérez and Lapizco-Encinas, 2011] Jesús-Pérez, N. M. and Lapizco-Encinas, B. H. (2011). Dielectrophoretic monitoring of microorganisms in environmental applications. *Electrophoresis*, 32(17):2331–2357.

[Jones, 2003] Jones, T. (2003). Basic theory of dielectrophoresis and electrorotation. *Engineering in Medicine and Biology Magazine, IEEE*, 22(6):33–42.

[Jones, 1979] Jones, T. B. (1979). Dielectrophoretic force calculation. *Journal of Electrostatics*, 6(1):69–82.

[Jones, 1995] Jones, T. B. (1995). *Electromechanics of Particles*. Cambridge University Press.

[Jones and Bliss, 1977] Jones, T. B. and Bliss, G. W. (1977). Bubble dielectrophoresis. *Journal of Applied Physics*, 48(4):1412–1417.

[Jones and Kallio, 1979] Jones, T. B. and Kallio, G. A. (1979). Dielectrophoretic levitation of spheres and shells. *Journal of Electrostatics*, 6(3):207–224.

[Jones and Kraybill, 1986] Jones, T. B. and Kraybill, J. P. (1986). Active feedback #x2010;controlled dielectrophoretic levitation. *Journal of Applied Physics*, 60(4):1247 –1252.

[Jones and Kraybill, 1987] Jones, T. B. and Kraybill, J. P. (1987). Dielectrophoretic Levitation of Small Metallic Particles. *IEEE Transactions on Industry Applications*, IA-23(6):980 –983.

Bibliography

[Kaler and Jones, 1990] Kaler, K. and Jones, T. B. (1990). Dielectrophoretic spectra of single cells determined by feedback-controlled levitation. *Biophys. Journal*, 57:173–182.

[Kavraki, 1997] Kavraki, L. (1997). Part orientation with programmable vector fields: two stable equilibria for most parts. In *Robotics and Automation, 1997. Proceedings., 1997 IEEE International Conference on*, volume 3, pages 2446–2451 vol.3.

[Keilman et al., 2004] Keilman, J. R., Jullien, G. A., and Kaler, K. V. I. S. (2004). A programmable AC electrokinetic analysis system. In *IEEE International Workshop on Biomedical Circuits and Systems, 2004.*, pages S2/3–9–12.

[Khamesee et al., 2002] Khamesee, M. B., Kato, N., Nomura, Y., and Nakamura, T. (2002). Design and control of a microrobotic system using magnetic levitation. *IEEE/ASME Transactions on Mechatronics*, 7(1):1–14.

[Khan et al., 2012] Khan, M. U., Bencheikh, N., Prelle, C., Lamarque, F., Beutel, T., and Buttgenbach, S. (2012). A Long Stroke Electromagnetic XY Positioning Stage for Micro Applications. *IEEE/ASME Transactions on Mechatronics*, 17(5):866–875.

[Kharboutly and Gauthier, 2013] Kharboutly, M. and Gauthier, M. (2013). High speed closed loop control of a dielectrophoresis-based system. In *2013 IEEE International Conference on Robotics and Automation (ICRA)*, pages 1446–1451.

[Kharboutly et al., 2009] Kharboutly, M., Gauthier, M., and Chaillet, N. (2009). Modeling the trajectory of a microparticle in a dielectrophoresis device. *Journal of Applied Physics*, 106:114312.

[Kharboutly et al., 2010] Kharboutly, M., Gauthier, M., and Chaillet, N. (2010). Predictive control of a micro bead's trajectory in a dielectrophoresis-based device. In *Intelligent Robots and Systems (IROS), 2010 IEEE/RSJ International Conference on*, pages 5616–5621.

[Kharboutly et al., 2012a] Kharboutly, M., Melis, A., Bolopion, A., Chaillet, N., and Gauthier, M. (2012a). 2d robotic control of a planar dielectrophoresis-based system. In *2012 International Conference on Manipulation, Manufacturing and Measurement on the Nanoscale (3M-NANO)*, pages 148–153.

[Kharboutly et al., 2012b] Kharboutly, M., Melis, A., Gauthier, M., and Chaillet, N. (2012b). 2d open loop trajectory control of a micro-object in a dielectrophoresis-based device. In *2012 IEEE International Conference on Automation Science and Engineering (CASE)*, pages 950–955.

[Khoshmanesh et al., 2011] Khoshmanesh, K., Nahavandi, S., Baratchi, S., Mitchell, A., and Kalantar-zadeh, K. (2011). Dielectrophoretic platforms for bio-microfluidic systems. *Biosensors and Bioelectronics*, 26(5):1800–1814.

[Koelman et al., 2015] Koelman, Z., de Graaf, M. J., and Lee, H. (2015). From meaning to liquid matters. In *Proceedings of the 21st International Symposium on Electronic Art*.

[Komori and Hirakawa, 2005] Komori, M. and Hirakawa, T. (2005). A magnetically driven linear microactuator with new driving method. *IEEE/ASME Transactions on Mechatronics*, 10(3):335–338.

[Konishi and Fujita, 1994] Konishi, S. and Fujita, H. (1994). A conveyance system using air flow based on the concept of distributed micro motion systems. *Microelectromechanical Systems, Journal of*, 3(2):54–58.

[Kono and Kakehi, 2012] Kono, M. and Kakehi, Y. (2012). Tamable Looper: Creature-like Expressions and Interactions by Movement and Deformation of Clusters of Sphere Magnets. In *ACM SIGGRAPH 2012 Posters*, SIGGRAPH '12, pages 25:1–25:1, New York, NY, USA. ACM.

[Kratochvil et al., 2014] Kratochvil, B. E., Kummer, M. P., Erni, S., Borer, R., Frutiger, D. R., Schürle, S., and Nelson, B. J. (2014). MiniMag: A Hemispherical Electromagnetic System for 5-DOF Wireless Micromanipulation. In *Experimental Robotics*, Springer Tracts in Advanced Robotics, pages 317–329. Springer, Berlin, Heidelberg.

[Kruhn et al., 2013] Kruhn, T., Radosavac, M., Shchekutin, N., and Overmeyer, L. (2013). Decentralized and dynamic routing for a Cognitive Conveyor. In *2013 IEEE/ASME International Conference on Advanced Intelligent Mechatronics (AIM)*, pages 436–441.

[Ku et al., 2001] Ku, P.-J., Winther, K., Stephanou, H., and Safaric, R. (2001). Distributed control system for an active surface device. In *IEEE International Conference on Robotics and Automation, 2001. Proceedings 2001 ICRA.*, volume 4, pages 3417–3422 vol.4.

Bibliography

[Kua et al., 2005] Kua, C. H., Lam, Y. C., Yang, C., and Youcef-Toumi, K. (2005). Review of bio-particle manipulation using dielectrophoresis.

[Kummer et al., 2010] Kummer, M. P., Abbott, J. J., Kratochvil, B. E., Borer, R., Sengul, A., and Nelson, B. J. (2010). OctoMag: An Electromagnetic System for 5-DOF Wireless Micromanipulation. *IEEE Transactions on Robotics*, 26(6):1006–1017.

[Lapizco-Encinas and Rito-Palomares, 2007] Lapizco-Encinas, B. H. and Rito-Palomares, M. (2007). Dielectrophoresis for the manipulation of nanobioparticles. *Electrophoresis*, 28(24):4521–4538.

[Laurent et al., 2011] Laurent, G., Delettre, A., and Le Fort-Piat, N. (2011). A New Aerodynamic-Traction Principle for Handling Products on an Air Cushion. *IEEE Transactions on Robotics*, 27(2):379–384.

[Laurent and Moon, 2015] Laurent, G. J. and Moon, H. (2015). A survey of non-prehensile pneumatic manipulation surfaces: principles, models and control. *Intelligent Service Robotics*, 8(3):151–163.

[Lee et al., 2006] Lee, H., Liu, Y., Westervelt, R. M., and Ham, D. (2006). IC/microfluidic hybrid system for magnetic manipulation of biological cells. *IEEE Journal of Solid-State Circuits*, 41(6):1471–1480.

[Lee et al., 2004] Lee, H., Purdon, A. M., Chu, V., and Westervelt, R. M. (2004). Controlled Assembly of Magnetic Nanoparticles from Magnetotactic Bacteria Using Microelectromagnets Arrays. *Nano Letters*, 4(5):995–998.

[Leithinger et al., 2014] Leithinger, D., Follmer, S., Olwal, A., and Ishii, H. (2014). Physical Telepresence: Shape Capture and Display for Embodied, Computer-mediated Remote Collaboration. In *Proceedings of the 27th Annual ACM Symposium on User Interface Software and Technology*, UIST '14, pages 461–470, New York, NY, USA. ACM.

[Lewis and Syrmos, 1995] Lewis, F. L. and Syrmos, V. L. (1995). *Optimal Control, 2nd Edition*. Wiley-Interscience, 2 edition.

[Lewis et al., 2015] Lewis, J. M., Heineck, D. P., and Heller, M. J. (2015). Detecting cancer biomarkers in blood: challenges for new molecular diagnostic and point-of-care tests using cell-free nucleic acids. *Expert Review of Molecular Diagnostics*, 15(9):1187–1200.

160

[Liberzon, 2003] Liberzon, D. (2003). *Switching in Systems and Control*. Birkhäuser, Boston, MA, 2003 edition edition.

[Lin and Yeow, 2007] Lin, J. and Yeow, J. (2007). Enhancing dielectrophoresis effect through novel electrode geometry. *Biomedical Microdevices*, 9(6):823–831.

[Lin et al., 2006] Lin, Y., Amberg, G., Aldaeus, F., and Roeraade, J. (2006). Simulation of dielectrophoretic motion of microparticles using a molecular dynamics approach. In *4th International Conference on Nanochannels, Microchannels and Minichannels*, Limerick, Ireland. ASME.

[Liu et al., 1995] Liu, C., Tsao, T., Tai, Y.-C., Liu, W., Will, P., and Ho, C.-M. (1995). A Micromachined Permalloy Magnetic Actuator Array for Micro Robotics Assembly Systems. In *The 8th International Conference on Solid-State Sensors and Actuators, 1995 and Eurosensors IX.. Transducers '95*, volume 1, pages 328–331.

[Liu and Will, 1995] Liu, W. and Will, P. (1995). Parts manipulation on an intelligent motion surface. In *Proceedings 1995 IEEE/RSJ International Conference on Intelligent Robots and Systems. Human Robot Interaction and Cooperative Robots*, volume 3, pages 399–404 vol.3.

[Luntz et al., 1997] Luntz, J., Messner, W., and Choset, H. (1997). Parcel manipulation and dynamics with a distributed actuator array: the virtual vehicle. In *Proceedings of International Conference on Robotics and Automation*, volume 2, pages 1541–1546 vol.2.

[Luntz and Moon, 2001] Luntz, J. and Moon, H. (2001). Distributed manipulation with passive air flow. In *2001 IEEE/RSJ International Conference on Intelligent Robots and Systems, 2001. Proceedings*, volume 1, pages 195–201 vol.1.

[Luntz et al., 2001] Luntz, J. E., Messner, W., and Choset, H. (2001). Distributed Manipulation Using Discrete Actuator Arrays. *The International Journal of Robotics Research*, 20(7):553–583.

[Luo et al., 2018] Luo, H., Sun, W., and Yeow, J. T. (2018). Modelling and adaptive dynamic sliding mode control of dielectrophoresis-based micromanipulation. *Transactions of the Institute of Measurement and Control*, 40(1):122–134.

Bibliography

[Machek, 2017] Machek (2017). Flow control by shaping electric field through an array of microelectrodes. Master's thesis, Czech Technical University in Prague, Prague, Czech Republic.

[Manaresi et al., 2003] Manaresi, N., Romani, A., Medoro, G., Altomare, L., Leonardi, A., Tartagni, M., and Guerrieri, R. (2003). A CMOS chip for individual cell manipulation and detection. *Solid-State Circuits, IEEE Journal of*, 38(12):2297–2305.

[Martel, 2017] Martel, S. (2017). Beyond imaging: Macro- and microscale medical robots actuated by clinical MRI scanners. *Science Robotics*, 2(3):eaam8119.

[Marzo et al., 2018] Marzo, A., Corkett, T., and Drinkwater, B. W. (2018). Ultraino: An Open Phased-Array System for Narrowband Airborne Ultrasound Transmission. *IEEE Transactions on Ultrasonics, Ferroelectrics, and Frequency Control*, 65(1):102–111.

[Masuda and Kamimura, 1975] Masuda, S. and Kamimura, T. (1975). Approximate methods for calculating a non-uniform travelling field. *Journal of Electrostatics*, 1(4):351–370.

[Masuda et al., 1987] Masuda, S., Washizu, M., and Iwadare, M. (1987). Separation of Small Particles Suspended in Liquid by Nonuniform Traveling Field. *Industry Applications, IEEE Transactions on*, IA-23(3):474–480.

[Masuda et al., 1988] Masuda, S., Washizu, M., and Kawabata, I. (1988). Movement of blood cells in liquid by nonuniform traveling field. *Industry Applications, IEEE Transactions on*, 24(2):217–222.

[McEvoy and Correll, 2015] McEvoy, M. A. and Correll, N. (2015). Materials that couple sensing, actuation, computation, and communication. *Science*, 347(6228):1261689.

[Medoro et al., 2007] Medoro, G., Guerrieri, R., Manaresi, N., Nastruzzi, C., and Gambari, R. (2007). Lab on a Chip for Live-Cell Manipulation. *IEEE Design Test of Computers*, 24(1):26–36.

[Medoro et al., 2003] Medoro, G., Manaresi, N., Leonardi, A., Altomare, L., Tartagni, M., and Guerrieri, R. (2003). A lab-on-a-chip for cell detection and manipulation. *Sensors Journal, IEEE*, 3(3):317–325.

162

[Menciassi et al., 2004] Menciassi, A., Eisinberg, A., Izzo, I., and Dario, P. (2004). From "macro" to "micro" manipulation: models and experiments. *IEEE/ASME Transactions on Mechatronics*, 9(2):311–320.

[Michálek, 2013] Michálek, T. (2013). *Matrix electrode array for dielectrophoresis - basic position control (in Czech).* Bachelor's thesis, Czech Technical University in Prague, Prague, Czech Republic.

[Michálek, 2015] Michálek, T. (2015). Real-time optimization-based control for dielectrophoresis. Master's thesis, Czech Technical University in Prague, Prague, Czech Republic.

[Michálek and Zemánek, 2017] Michálek, T. and Zemánek, J. (2017). Dipole and multipole models of dielectrophoresis for a non-negligible particle size: Simulations and experiments. *Electrophoresis*, 38(11):1419–1426.

[Miled and Sawan, 2010] Miled, M. A. and Sawan, M. (2010). A new CMOS/microfluidic interface for cells manipulation and separation in LoC devices. In *2nd Asia Symposium on Quality Electronic Design (ASQED)*, pages 194–197.

[Mita et al., 1997] Mita, Y., Konishi, S., and Fujita, H. (1997). Two dimensional micro conveyance system with through holes for electrical and fluidic interconnection. In *, 1997 International Conference on Solid State Sensors and Actuators, 1997. Transducers '97 Chicago*, volume 1, pages 37–40 vol.1.

[Moffitt et al., 2008] Moffitt, J. R., Chemla, Y. R., Smith, S. B., and Bustamante, C. (2008). Recent Advances in Optical Tweezers. *Annual Review of Biochemistry*, 77(1):205–228.

[Morgan and Green, 2002] Morgan, H. and Green, N. G. (2002). *AC Electrokinetic: Colloids and Nanoparticles.* Research Studies Pr Ltd, Baldock, 1st edition edition.

[Morgan et al., 1997] Morgan, H., Green, N. G., Hughes, M. P., Monaghan, W., and Tan, T. C. (1997). Large-area travelling-wave dielectrophoresis particle separator. *Journal of Micromechanics and Microengineering*, 7(2):65–70.

[Morgan et al., 2001] Morgan, H., Izquierdo, A. G., Bakewell, D., Green, N. G., and Ramos, A. (2001). The dielectrophoretic and travelling wave forces generated by interdigitated electrode arrays: analytical solution

Bibliography

using Fourier series. *Journal of Physics D: Applied Physics*, 34(10):1553–1561.

[Murphey and Burdick, 2004] Murphey, T. D. and Burdick, J. W. (2004). Feedback Control Methods for Distributed Manipulation Systems that Involve Mechanical Contacts. *The International Journal of Robotics Research*, 23(7-8):763–781.

[Nakazawa et al., 1997] Nakazawa, H., Watanabe, Y., Morita, O., Edo, M., and Yonezawa, E. (1997). The two-dimensional micro conveyer: principles and fabrication process of the actuator. In *, 1997 International Conference on Solid State Sensors and Actuators, 1997. Transducers '97 Chicago*, volume 1, pages 33–36 vol.1.

[Nelson et al., 2010] Nelson, B. J., Kaliakatsos, I. K., and Abbott, J. J. (2010). Microrobots for Minimally Invasive Medicine. *Annual Review of Biomedical Engineering*, 12(1):55–85.

[Ochiai et al., 2013] Ochiai, Y., Hoshi, T., and Rekimoto, J. (2013). Three-dimensional Mid-air Acoustic Manipulation by Ultrasonic Phased Arrays. *arXiv:1312.4006 [physics]*. arXiv: 1312.4006.

[O'Riordan et al., 2004] O'Riordan, A., Delaney, P., and Redmond, G. (2004). Field Configured Assembly: Programmed Manipulation and Self-assembly at the Mesoscale. *Nano Letters*, 4(5):761–765.

[Oyobe et al., 2000] Oyobe, H., Kitajima, H., and Hori, Y. (2000). Design and realization of autonomous decentralized object transfer system: magic carpet. In *6th International Workshop on Advanced Motion Control, 2000. Proceedings*, pages 25–29.

[Pangaro et al., 2002] Pangaro, G., Maynes-Aminzade, D., and Ishii, H. (2002). The Actuated Workbench: Computer-controlled Actuation in Tabletop Tangible Interfaces. In *Proceedings of the 15th Annual ACM Symposium on User Interface Software and Technology*, UIST '02, pages 181–190, New York, NY, USA. ACM.

[Pawashe et al., 2012] Pawashe, C., Floyd, S., Diller, E., and Sitti, M. (2012). Two-Dimensional Autonomous Microparticle Manipulation Strategies for Magnetic Microrobots in Fluidic Environments. *IEEE Transactions on Robotics*, 28(2):467 –477.

164

[Pelrine, 1989] Pelrine, R. (1989). Maglev microrobotics: an approach toward highly integrated small-scale manufacturing systems. In *Electronic Manufacturing Technology Symposium, 1989, Proceedings. Seventh IEEE/CHMT International*, pages 273–276.

[Pelrine et al., 2012] Pelrine, R., Wong-Foy, A., McCoy, B., Holeman, D., Mahoney, R., Myers, G., Herson, J., and Low, T. (2012). Diamagnetically levitated robots: An approach to massively parallel robotic systems with unusual motion properties. In *2012 IEEE International Conference on Robotics and Automation (ICRA)*, pages 739–744.

[Pethig, 2010] Pethig, R. (2010). Dielectrophoresis: Status of the theory, technology, and applications. *Biomicrofluidics*, 4(2):022811.

[Pethig, 2013] Pethig, R. (2013). Dielectrophoresis: An assessment of its potential to aid the research and practice of drug discovery and delivery. *Advanced Drug Delivery Reviews*, 65(11–12):1589–1599.

[Pethig, 2017a] Pethig, R. (2017a). Review—Where Is Dielectrophoresis (DEP) Going? *Journal of The Electrochemical Society*, 164(5):B3049–B3055.

[Pethig et al., 1998] Pethig, R., Burt, J. P. H., Parton, A., Rizvi, N., Talary, M. S., and Tame, J. A. (1998). Development of biofactory-on-a-chip technology using excimer laser micromachining. *Journal of Micromechanics and Microengineering*, 8(2):57–63.

[Pethig, 2017b] Pethig, R. R. (2017b). *Dielectrophoresis: Theory, Methodology and Biological Applications*. Wiley, Hoboken, NJ, 1 edition edition.

[Pieters et al., 2016] Pieters, R., Lombriser, S., Alvarez-Aguirre, A., and Nelson, B. J. (2016). Model Predictive Control of a Magnetically Guided Rolling Microrobot. *IEEE Robotics and Automation Letters*, 1(1):455–460.

[Pister et al., 1990] Pister, K. S. J., Fearing, R. S., and Howe, R. T. (1990). A planar air levitated electrostatic actuator system. In *IEEE Micro Electro Mechanical Systems, 1990. Proceedings, An Investigation of Micro Structures, Sensors, Actuators, Machines and Robots*, pages 67–71.

[Pohl, 1978] Pohl, H. (1978). *Dielectrophoresis*. Cambridge University Press.

[Pohl, 1951] Pohl, H. A. (1951). The Motion and Precipitation of Suspensoids in Divergent Electric Fields. *Journal of Applied Physics*, 22(7):869–871.

Bibliography

[Pohl, 1958] Pohl, H. A. (1958). Some Effects of Nonuniform Fields on Dielectrics. *Journal of Applied Physics*, 29(8):1182–1188.

[Pohl, 1960] Pohl, H. A. (1960). Nonuniform Electric Fields. *Scientific American*, 203:106–116.

[Pohl and Crane, 1971] Pohl, H. A. and Crane, J. S. (1971). Dielectrophoresis of Cells. *Biophysical Journal*, 11(9):711–727.

[Pohl and Hawk, 1966] Pohl, H. A. and Hawk, I. (1966). Separation of Living and Dead Cells by Dielectrophoresis. *Science*, 152(3722):647–a–649.

[Pohl and Schwar, 1959] Pohl, H. A. and Schwar, J. P. (1959). Factors Affecting Separations of Suspensions in Nonuniform Electric Fields. *Journal of Applied Physics*, 30(1):69–73.

[Popa, 2014] Popa, D. (2014). Robust and Reliable Microtechnology Research and Education through the Mobile Microrobotics Challenge [Competitions]. *IEEE Robotics Automation Magazine*, 21(1):8–12.

[Pozrikidis, 2002] Pozrikidis, C. (2002). *A Practical Guide to Boundary Element Methods with the Software Library BEMLIB*. CRC Press, Boca Raton, Fla., 1 edition edition.

[Probst et al., 2012] Probst, R., Cummins, Z., Ropp, C., Waks, E., and Shapiro, B. (2012). Flow Control of Small Objects on Chip: Manipulating Live Cells, Quantum Dots, and Nanowires. *Control Systems, IEEE*, 32(2):26 –53.

[Probst et al., 2011] Probst, R., Lin, J., Komaee, A., Nacev, A., Cummins, Z., and Shapiro, B. (2011). Planar steering of a single ferrofluid drop by optimal minimum power dynamic feedback control of four electromagnets at a distance. *Journal of Magnetism and Magnetic Materials*, 323(7):885–896.

[Rahmer et al., 2017] Rahmer, J., Stehning, C., and Gleich, B. (2017). Spatially selective remote magnetic actuation of identical helical micromachines. *Science Robotics*, 2(3):eaal2845.

[Ramos, 2011] Ramos, A., editor (2011). *Electrokinetics and Electrohydrodynamics in Microsystems*. Springer, Wien ; New York, 2011 edition edition.

[Reznik et al., 2001] Reznik, D., Canny, J., and Alldrin, N. (2001). Leaving on a plane jet. In *2001 IEEE/RSJ International Conference on Intelligent Robots and Systems, 2001. Proceedings*, volume 1, pages 202–207 vol.1.

[Reznik and Canny, 2001] Reznik, D. S. and Canny, J. F. (2001). C'mon part, do the local motion! In *Proceedings 2001 ICRA. IEEE International Conference on Robotics and Automation (Cat. No.01CH37164)*, volume 3, pages 2235–2242 vol.3.

[Richter, 2014] Richter, F. (2014). *Instrumentation upgrade for Magman magnetic platform (in Czech).* Bachelor's thesis, Czech Technical University in Prague, Prague, Czech Republic.

[Richter, 2017] Richter, F. (2017). Extension of the platform for magnetic manipulation. Master's thesis, Czech Technical University in Prague, Prague, Czech Republic.

[Rosales and Lim, 2005] Rosales, C. and Lim, K. M. (2005). Numerical comparison between Maxwell stress method and equivalent multipole approach for calculation of the dielectrophoretic force in single-cell traps. *Electrophoresis*, 26(11):2057–2065.

[Rosenthal and Voldman, 2005] Rosenthal, A. and Voldman, J. (2005). Dielectrophoretic Traps for Single-Particle Patterning. *Biophysical Journal*, 88(3):2193–2205.

[Safaric et al., 2000] Safaric, R., Uran, S., and Winther, K. (2000). Closed-loop control of rigid and flexible objects on a pneumatic active surface device. In *Proceedings. 2000 IEEE/RSJ International Conference on Intelligent Robots and Systems (IROS 2000)*, volume 1, pages 486–491 vol.1.

[Safaric et al., 2002] Safaric, R., Uran, S., and Winther, T. (2002). Massive motion control of sub-millimeter objects. In *7th International Workshop on Advanced Motion Control. Proceedings*, pages 604–609.

[Samiei et al., 2016] Samiei, E., Tabrizian, M., and Hoorfar, M. (2016). A review of digital microfluidics as portable platforms for lab-on a-chip applications. *Lab on a Chip*, 16(13):2376–2396.

[Schaler et al., 2012] Schaler, E., Tellers, M., Gerratt, A., Penskiy, I., and Bergbreiter, S. (2012). Toward fluidic microrobots using electrowetting. In *2012 IEEE International Conference on Robotics and Automation*, pages 3461 –3466.

Bibliography

[Simha et al., 2011a] Simha, H., Banavar, R. N., and Chang, D. E. (2011a). Reachability and controllability of a particle in a dielectrophoretic system. *Systems & Control Letters*, 60(7):460–467.

[Simha et al., 2011b] Simha, H., Barve, H. A., and Banavar, R. N. (2011b). Energy-optimal control of a particle in a dielectrophoretic system. *Optimal Control Applications and Methods*, pages n/a–n/a.

[Simonian, 2014] Simonian, A. (2014). Feedback control for planar parallel magnetic manipulation. Master's thesis, Czech Technical University in Prague, Prague, Czech Republic.

[Sin et al., 2011] Sin, M. L., Gao, J., Liao, J. C., and Wong, P. K. (2011). System Integration - A Major Step toward Lab on a Chip. *Journal of Biological Engineering*, 5:6.

[Suehiro and Pethig, 1998] Suehiro, J. and Pethig, R. (1998). The dielectrophoretic movement and positioning of a biological cell using a three-dimensional grid electrode system. *Journal of Physics D: Applied Physics*, 31(22):3298.

[Suh et al., 1999] Suh, J., Darling, R., Bohringer, K.-F., Donald, B., Baltes, H., and Kovacs, G. (1999). CMOS integrated ciliary actuator array as a general-purpose micromanipulation tool for small objects. *Microelectromechanical Systems, Journal of*, 8(4):483–496.

[Suh et al., 1997] Suh, J. W., Glander, S. F., Darling, R. B., Storment, C. W., and Kovacs, G. T. A. (1997). Organic thermal and electrostatic ciliary microactuator array for object manipulation. *Sensors and Actuators A: Physical*, 58(1):51–60.

[Sun, 2005] Sun, Z. (2005). *Switched Linear Systems: Control and Design*. Springer, London, 2005 edition edition.

[Terray et al., 2002] Terray, A., Oakey, J., and Marr, D. W. M. (2002). Microfluidic Control Using Colloidal Devices. *Science*, 296(5574):1841–1844.

[Tomášek, 2013] Tomášek, J. (2013). *Optically controlled and sensed micromanipulation - basic setup*. Bachelor's thesis, Czech Technical University in Prague, Prague, Czech Republic.

[Varsos and Luntz, 2006] Varsos, K. and Luntz, J. (2006). Superposition Methods for Distributed Manipulation Using Quadratic Potential Force Fields. *Robotics, IEEE Transactions on*, 22(6):1202–1215.

[Varsos et al., 2006] Varsos, K., Moon, H., and Luntz, J. (2006). Generation of quadratic potential force fields from flow fields for distributed manipulation. *Robotics, IEEE Transactions on*, 22(1):108–118.

[Vela et al., 2009] Vela, E., Hafez, M., and Regnier, S. (2009). Laser-Induced Thermocapillary Convection for Mesoscale Manipulation. *International Journal of Optomechatronics*, 3(4):289–302. WOS:000272736600005.

[Vlaminck and Dekker, 2012] Vlaminck, I. D. and Dekker, C. (2012). Recent Advances in Magnetic Tweezers. *Annual Review of Biophysics*, 41(1):453–472.

[Walker, 2012] Walker, G. (2012). A review of technologies for sensing contact location on the surface of a display. *Journal of the Society for Information Display*, 20(8):413–440.

[Wang et al., 2013] Wang, C.-C., Lan, K.-C., Chen, M.-K., Wang, M.-H., and Jang, L.-S. (2013). Adjustable trapping position for single cells using voltage phase-controlled method. *Biosensors and Bioelectronics*, 49:297–304.

[Wang et al., 2007] Wang, K.-L., Jones, T. B., and Raisanen, A. (2007). Dynamic control of DEP actuation and droplet dispensing. *Journal of Micromechanics and Microengineering*, 17:76–80.

[Wang et al., 1996] Wang, X., Wang, X.-B., Becker, F. F., and Gascoyne, P. R. C. (1996). A theoretical method of electrical field analysis for dielectrophoretic electrode arrays using Green's theorem. *Journal of Physics D: Applied Physics*, 29(6):1649–1660.

[Wang and Zhe, 2011] Wang, Z. and Zhe, J. (2011). Recent advances in particle and droplet manipulation for lab-on-a-chip devices based on surface acoustic waves. *Lab on a Chip*, 11(7):1280–1285.

[Wautelet, 2001] Wautelet, M. (2001). Scaling laws in the macro-, micro- and nanoworlds. *European Journal of Physics*, 22(6):601–611.

[Weiss et al., 2011a] Weiss, M., Remy, C., and Borchers, J. (2011a). Rendering Physical Effects in Tabletop Controls. In *Proceedings of the SIGCHI*

Conference on Human Factors in Computing Systems, CHI '11, pages 3009–3012, New York, NY, USA. ACM.

[Weiss et al., 2010] Weiss, M., Schwarz, F., Jakubowski, S., and Borchers, J. (2010). Madgets: Actuating Widgets on Interactive Tabletops. In *Proceedings of the 23Nd Annual ACM Symposium on User Interface Software and Technology*, UIST '10, pages 293–302, New York, NY, USA. ACM.

[Weiss et al., 2011b] Weiss, M., Wacharamanotham, C., Voelker, S., and Borchers, J. (2011b). FingerFlux: Near-surface Haptic Feedback on Tabletops. In *Proceedings of the 24th Annual ACM Symposium on User Interface Software and Technology*, UIST '11, pages 615–620, New York, NY, USA. ACM.

[Wu and Ozcan, 2018] Wu, Y. and Ozcan, A. (2018). Lensless digital holographic microscopy and its applications in biomedicine and environmental monitoring. *Methods*, 136:4–16.

[Yu et al., 2014] Yu, X., Hong, J., Liu, C., and Kim, M. K. (2014). Review of digital holographic microscopy for three-dimensional profiling and tracking. *Optical Engineering*, 53(11):112306.

[Zemanek et al., 2014] Zemanek, J., Drs, J., and Hurak, Z. (2014). Dielectrophoretic actuation strategy for micromanipulation along complex trajectories. In *2014 IEEE/ASME International Conference on Advanced Intelligent Mechatronics (AIM)*, pages 19–25.

[Zemánek et al., 2015] Zemánek, J., Michálek, T., and Hurák, Z. (2015). Feedback control for noise-aided parallel micromanipulation of several particles using dielectrophoresis. *Electrophoresis*, 36(13):1451–1458.

[Zemánek et al., 2017] Zemánek, J., Čelikovský, S., and Hurák, Z. (2017). Time-optimal Control for Bilinear Nonnegative-in-control Systems: Application to Magnetic Manipulation. *IFAC-PapersOnLine*, 50(1):16032–16039.

[Zhang et al., 2009] Zhang, C., Khoshmanesh, K., Mitchell, A., and Kalantar-zadeh, K. (2009). Dielectrophoresis for manipulation of micro/nano particles in microfluidic systems. *Analytical and Bioanalytical Chemistry*, 396(1):401–420.

[Çetin and Li, 2011] Çetin, B. and Li, D. (2011). Dielectrophoresis in microfluidics technology. *Electrophoresis*, 32(18):2410–2427.

Published papers

Journal papers

- Michálek, T. and Zemánek, J. (2017). Dipole and multipole models of dielectrophoresis for a non-negligible particle size: Simulations and experiments. *Electrophoresis*, 38(11):1419–1426.

- Gurtner, M. and Zemánek, J. (2016). Twin-beam real-time position estimation of micro-objects in 3D. *Measurement Science and Technology*, 27(12):127003.

- Zemánek, J., Michálek, T., and Hurák, Z. (2015). Feedback control for noise-aided parallel micromanipulation of several particles using dielectrophoresis. *Electrophoresis*, 36(13):1451–1458.

Conference papers in Web of Science

- Zemánek, J., Čelikovský, S., and Hurák, Z. (2017). Time-optimal control for bilinear nonnegative-in-control systems: Application to magnetic manipulation. *IFAC-PapersOnLine*, 50(1):16032–16039.

- Zemánek, J., Drs, J., and Hurák, Z. (2014). Dielectrophoretic actuation strategy for micromanipulation along complex trajectories. In *2014 IEEE/ASME International Conference on Advanced Intelligent Mechatronics (AIM)*, pages 19–25.

- Basova, E., Drs, J., Zemánek, J., Hurák, Z., and Foret, F. (2013). Integrated microfludic device for droplet manipulation. *2013 CECE JUNIOR Conference*, pages S291–S293.

- Hurák, Z. and Zemánek, J. (2012). Feedback linearization approach to distributed feedback manipulation. In *American Control Conference (ACC), 2012*, pages 991–996.

- Zemánek, J. and Hurák, Z. (2009). Noncontact Parallel Manipulation with Meso-and Microscale Particles Using Dielectrophoresis. *In Nanocon 2009 Conference Proceedings*, pages 276–283.

Other papers

- Zemánek, J., Michálek, T., and Hurák, Z. (2016). Real-time optimization-based control of phase shifts for planar dielectrophoretic micromanipulation. *Dielectrophoresis 2016 Conference.*

- Gurtner, M. and Zemánek, J. (2016). Real-time lensless optical position estimation method for dielectrophoretic micromanipulation. *Dielectrophoresis 2016 Conference.*

- Michálek, T. and Zemánek, J. (2016). Comparison of several control-oriented models for dielectrophoresis against Maxwell stress tensor predictions and their experimental verification. *Dielectrophoresis 2016 Conference.*

- Zemánek, J. and Hurák, Z. (2013). Magnetic manipulator (Magman): Design and implementation in Matlab. *Technical Computing Prague 2013*, page 389.

- Zemánek, J., Hurák, Z., and Bellouard, Y. (2010) Modeling and simulation, design and fabrication, instrumentation and control for dielectrophoresis. In *25th International Symposium on Microscale BioSeparations MSB 2010.*

Awards

- Winner of EEA Demonstrator Paper Prize on IFAC World Congress 2017—Awarded for paper [Zemánek et al., 2017] and on-site demonstration.

- Winner of IEEE CSS Video Clip Contest 2017—Awarded for a video clip *Ball and Hoop - motivation for numerical optimal control*[1].

- Winner of MATLAB and Simulink Student Design Challenge 2013— *Awarded for a video clip Magnetic manipulator Magman and Matlab*[2].

---

[1]Video clip available at https://youtu.be/484GN4KBQnc.
[2]Video clip available at https://youtu.be/AhS_2gU1qW0.